Preliminary Design of a Turbine Test Facility for Rocket Engine Applications

Enhancing rapid and agile development of rocket engines

Pedro Cordeiro

TU Delft

arianeGROUP

Preliminary Design of a Turbine Test Facility for Rocket Engine Applications

Enhancing rapid and agile development of rocket engines

by

Pedro Cordeiro

to obtain the degree of Master of Science
at the Delft University of Technology,
to be defended publicly on Tuesday, December 16, 2025 at 12:45 PM.

Student number:	5978688	
Project duration:	February 1, 2025 – December 16, 2025	
Thesis committee:	Prof. dr. ir. M. Pini,	TU Delft, supervisor
	Dr. ir. L. Souverein,	ArianeGroup GmbH, supervisor
	Prof dr. ir. J. Guo,	TU Delft, chair
	Prof . dr . ir F. Schrijer,	TU Delft, external assessor

Cover: Artist’s view of Ariane 6 – Flight Model-1

Preface

I am proud to present this master's thesis, which marks the culmination of my studies in Aerospace Engineering at Delft University of Technology (TU Delft). Following the Space track has allowed me to pursue my long-standing passion for working with rocket engines and launch vehicles.

This work was carried out at ArianeGroup's division in Ottobrunn (Munich). I would like to express my sincere gratitude to ArianeGroup for welcoming me as a student and for believing in my skills from the very first day of this project. I could not have wished for a better place to pursue this work and grow as an engineer.

I would also like to express my sincere gratitude to my supervisors, Dr. Louis Souverein from ArianeGroup and Dr. Matteo Pini from TU Delft. I consider myself extremely fortunate to have been guided by two of the most inspiring engineers I have met throughout my academic journey. Their support, feedback, and expertise were instrumental in making this project feasible.

Furthermore, I would like to thank my colleagues at ArianeGroup for the countless hours of discussion, advice, and guidance. Without their help, this project would not have been possible. It would be difficult to name all of them without risking leaving out important names, so I will keep this as a general acknowledgment. However, I would like to extend special thanks to Dr. Antoine Mariot from ArianeGroup France for his extremely valuable guidance on the rotordynamics section.

Finally, I want to thank my family for their unwavering support, for believing in me from day one, and for providing me with the opportunities and resources that have allowed me to reach this point. I would also like to thank my friends, who made Delft a special place for me, allowing me to feel at home. I will remain deeply grateful for the moments we shared and for all the support they have given me.

To my friends back in Portugal, who supported me from a distance and were always there for me whenever I had the chance to return home, I am equally grateful. I am very fortunate to have you all in my life.

Pedro Cordeiro
Delft, December 2025

Abstract

This thesis presents the preliminary design of a modular, flexible turbine test facility for liquid rocket engine applications, aimed at enabling turbine-level testing at Technology Readiness Level 6 (TRL6) under hot, representative conditions. Existing facilities either lack flexibility or do not simultaneously reproduce the key operating parameters of pressure ratio, rotational speed, temperature, and driving medium, which limits turbine characterization and confidence in flight operation.

A three-phase methodology is adopted. First, top-level requirements are derived for turbines representative of 1 MN-class engines, and a scaling strategy is defined. The selected approach fixes Baljé specific speed and specific diameter, together with the inlet spouting Mach number, to preserve the main thermal and aero-mechanical phenomena while reducing power to a feasible range. Applying this methodology to a dataset of hydrogen–oxygen turbines yields a test envelope of roughly $3\ MW$ shaft power at 30–50 $krpm$ and defines the corresponding pressure, temperature, and mass-flow ranges for the facility.

In the second phase, several power-dissipation concepts are surveyed and modelled using zero- and one-dimensional analyses. A Pareto-based Analytic Hierarchy Process is then used to structure the trade-off. A self-designed, directly driven water pump with inducer and impeller stages is down-selected as the preferred concept, capable of absorbing $3\ MW$ of power at $100\ kg/s$ with a total pressure rise of $210\ bar$ while avoiding cavitation through appropriate inlet pressurization.

The third phase focuses on the shaft support subsystem. A parametric rotordynamic model of the coupled turbine–pump shaft and pillow block is developed to derive stiffness, damping, load, and lubrication requirements for angular-contact ball bearings operating in the 30–50 $krpm$ range. Results show that, with bearing stiffness in the 10^7–$10^8\ N/m$ range and moderate external damping, critical speeds can be placed outside the operating window, resonance crossings remain within acceptable displacement limits, and bearing loads and losses lie within achievable catalog values.

Overall, the work demonstrates the feasibility of a multi-MW turbine test facility that combines a high level of representativeness with broad flexibility, and provides ceiling requirements and subsystem concepts that form a concrete baseline for subsequent detailed design and eventual construction.

Contents

List of Figures

List of Tables

Nomenclature

Abbreviations

Abbreviation	Definition
LV	Launch Vehicle
TRL	Technology Readiness Level
NASA	National Aeronautics and Space Administration
ESA	European Space Agency
CFD	Computational Fluid Dynamics
PPA	Power Pack Assembly
GN_2	Gaseous Nitrogen
MIT	Massachusetts Institute of Technology
ILA Stuttgart	Institut für Luftfahrtantriebe Stuttgart
TTE	Turbine Test Equipment
MSFC	Marshall Space Flight Center
RQ	Research Question
H	Hypothesis
AHP	Analytic Hierarchy Process
0-D, 1-D	Zero- / One-Dimensional Modelling
FTP	Fuel Turbopump
OTP	Oxidizer Turbopump
FT	Fuel Turbine
OT	Oxidizer Turbine
OR	Operational Requirement
LOx	Liquid Oxygen
LH_2	Liquid Hydrogen
LCH_4	Liquid Methane
pb	Preburner
gg	Gas Generator
SC	Staged Combustion (cycle)
GG	Gas Generator (cycle)
HydroLOx	Hydrogen–Oxygen Propellant Combination
MethaLOx	Methane–Oxygen Propellant Combination
NPSH	Net Positive Suction Head (available / required)
EMF	Electromotive Force
3φ	Three-Phase (electrical systems)
ph	Phase
Y	Star (winding)
Δ	Delta (winding)
MV	Medium Voltage
HV	High Voltage
ECB	European Central Bank
PPI	Producer Price Index
OC	Operational Complexity
gb	Gearbox
S	Scalability
RBI	Required Base Infrastructure
RM	Reliability / Maintainability
CI	Consistency Index

Abbreviation	Definition
CR	Consistency Ratio
RI	Random Index
BEP	Best Efficiency Point
ISO	International Organization for Standardization
DOF	Degrees of Freedom
HC	Hybrid Ceramic (bearing ball material)

Symbols

Symbol	Definition	Unit
v	Velocity	$[m/s]$
v_{ax}	Axial velocity	$[m/s]$
Δv	Impulse / velocity increment	$[m/s]$
M	Mass	$[kg]$
I_{sp}	Specific impulse	$[s]$
p	Pressure	$[Pa]$
p_c	Chamber pressure	$[Pa]$
p_t	Total pressure	$[Pa]$
p_s	Static pressure	$[Pa]$
T	Temperature	$[K]$
T_t	Total temperature	$[K]$
T_s	Static temperature	$[K]$
c_p	Specific heat at constant pressure	$[J/(kg\,K)]$
c_0	Spouting velocity	$[m/s]$
Q	Volumetric flow rate	$[m^3/s]$
g_0	Standard gravitational acceleration	$[m/s^2]$
s	Seconds (time)	$[s]$
ft	Foot (imperial unit)	$[ft]$
N	Rotational speed	[rpm]
Ω	Angular velocity	$[rad/s]$
U_{tip}	Blade tip speed	$[m/s]$
D_s	Specific diameter	[-]
N_s	Specific speed (Baljé)	[-]
D_{tip}	Tip diameter	$[m]$
SF	Scaling factor	[-]
FT	Thrust (fuel turbine)	$[N]$
Re	Reynolds number	[-]
μ	Dynamic viscosity	$[Pa \cdot s]$
ν	Kinematic viscosity	$[m^2/s]$
$m_{f,e}$	Engine global fuel mass flow	$[kg/s]$
$m_{o,e}$	Engine global oxidizer mass flow	$[kg/s]$
$\dot{m}$	Mass flow rate	$[kg/s]$
$m_{\text{turb,FR–SC}}$	Turbine mass flow (fuel-rich staged combustion)	$[kg/s]$
$m_{\text{turb,OR–SC}}$	Turbine mass flow (oxidizer-rich staged combustion)	$[kg/s]$
O/F	Mixture ratio (oxidizer-to-fuel)	[-]
Δh_s	Adiabatic enthalpy drop	$[J/kg]$
Δh_{eff}	Effective enthalpy drop	$[J/kg]$
A_{son}	Speed of sound	$[m/s]$
A_{in}	Inlet area	$[m^2]$
R	Gas constant	$[J/(kg\,K)]$
η_{ts}	Total-to-static efficiency	[-]
η_c	Compressor efficiency	[-]
P_{output}	Output power	$[W]$

Symbol	Definition	Unit
P_{nom}	Nominal power	$[W]$
P_{scaled}	Scaled power	$[W]$
Δ	Variation	[-]
ρ	Density	$[kg/m^3]$
ρ_s	Static density	$[kg/m^3]$
w	Water (subscript, power brake context)	[-]
abs	Absorbed (power)	[-]
J_p	Polar moment of inertia	$[kg\,m^2]$
J_d	Diametral moment of inertia	$[kg\,m^2]$
τ	Torque	$[Nm]$
α	Angular acceleration	$[rad/s^2]$
f	Final (subscript)	[-]
i	Initial (subscript)	[-]
t_{spin}	Spin-up time	$[s]$
u	Gear ratio	[-]
b	Brake (subscript)	[-]
t	Total or turbine (context-dependent subscript)	[-]
hp	Horsepower	$[hp]$
H_{ad}	Adiabatic head rise (pump)	$[m]$
A_s	Suction area	$[m^2]$
v_{ap}	Vapour (pressure subscript)	[-]
N_{ss}	Suction specific speed (SI)	[-]
S_s	Suction specific speed (imperial)	[-]
S'_s	Corrected suction specific speed	[-]
ϕ	Flow coefficient	[-]
C	Cost	[€]
€	Euro Currency	[€]
$	Dollar Currency	[$]
$\dot{W}_p$	Pump power	$[W]$
$\dot{W}_c$	Compressor power	$[W]$
I	Electric current	$[A]$
R (electrical)	Electrical resistance	$[\Omega]$
V	Electric voltage	$[V]$
f_e	Electric frequency	$[Hz]$
n_p	Number of poles	[-]
F_{Ax}	Axial force (thrust)	$[N]$
k	Slip factor	[-]
d	Disk (subscript)	[-]
b	Blade (subscript)	[-]
l	Labyrinth (subscript)	[-]
res	Resultant (force)	[-]
ε_{per}	Permissible eccentricity	[-]
G	ISO grade (unbalance)	[-]
U	Unbalance	$[g \cdot mm]$
V	Volume	$[m^3]$
k_r	Radial force coefficient	[-]
d_2	Outlet diameter	$[m]$
d_1	Inlet diameter	$[m]$
b_1	Inlet width	$[m]$
b_2	Outlet width	$[m]$
$hydro$	Hydrodynamic (subscript)	[-]
dyn	Dynamic (subscript)	[-]
F_r	Resultant radial force	$[N]$
F_a	Resultant axial force	$[N]$

Symbol	Definition	Unit
S_0	Safety factor (bearings)	[-]
z	Axial direction	[-]
x, y	Radial directions	[-]
P_0	Equivalent bearing load	$[N]$
d_m	Bearing mean diameter	$[m]$
K	Stiffness	$[N/m]$
C	Damping	$[Ns/m]$
α (bearing)	Bearing contact angle	[°]
δ	Displacement	$[m]$
f_n	Natural frequency	$[Hz]$
rad	Radial (subscript)	[-]
ax	Axial (subscript)	[-]
L_{10h}	Bearing expected lifetime	$[h]$

1

Introduction

Launch vehicles (LVs) serve as the primary foundation for scientific and technological advancements enabled by space exploration. Either through the deployment of satellites to enable attitude changes of celestial bodies that could harm planet Earth, or through the exploration of celestial bodies beyond the boundaries of where humankind has sent any machine, LVs are essential to the mission's development.

The propulsion system is the heart of the LV. Providing the thrust required to power the LV, they are the single most complex and essential element of each LV. The engines themselves are complex systems, containing multiple propellant lines and turbomachinery to bring the propellants to the required inlet conditions for feeding into the engine. It is imperative that these systems are reliable and efficient to reduce costs and increase performance, democratizing access to space.

With the increasing need for more frequent and reliable launches, rocket engine development is at an unprecedented pace. Multiple companies surge in this highly competitive environment, where the one that can offer the lowest cost while ensuring reliability and a frequent launch cadence leads the market. As a result, it is fundamental for companies to adopt fast-paced development techniques, moving away from traditional, lengthy development processes.

Innovative development processes have been attempted in the last decades. One of them, which has proven to bring significant improvements in development duration, cost, and reliability, is the iterative development cycle (Figure 1.1). It lays on two main foundations: including testing earlier in the development chain and testing more frequently, after each relevant design iteration.

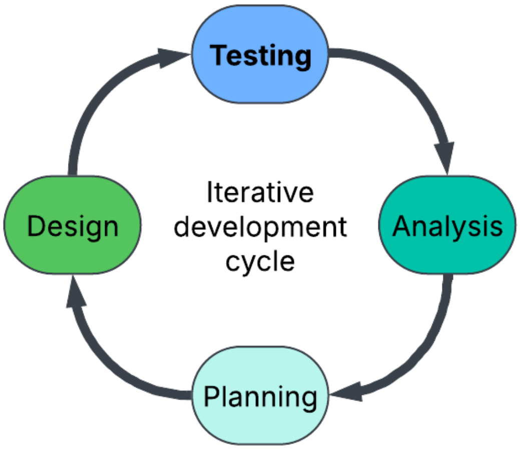

Figure 1.1: Iterative Development Cycle

This cycle uses test data from every test campaign to iterate on the design, improving cost, reliability, and performance. By conducting this cycle multiple times until the target operational requirements are satisfied and therefore testing more frequently, it is possible to achieve a deeper understanding of the system while offering valuable input to optimize existing models to predict performance parameters and ultimately reduce development time.

However, for iterative development to prevail as an improvement over classical design methodologies, key aspects must be considered. The most important of them is the ability to test quickly after each design iteration. This is essential for the cycle to succeed, as waiting several months or years for each design iteration to be tested can lead to significant delays in development. Avoiding such a delay often leads to testing being overlooked, which becomes a project risk because the system behaviour is not sufficiently characterized. The lack of understanding of the system's behaviour can bring substantial risks of cost and delays in a later project phase.

Therefore, the need for adequate and easily adaptable test facilities arises. This project's goal is to address this need by developing a modular, agile, and cost-effective test facility for turbines, a component of the turbopump — one of the most challenging subsystems of a rocket engine, the ”heart” of a launch vehicle.

The power levels attained by such devices often exceed $20\ MW$ during testing. Take, for example, ArianeGroup's Vulcain 2 hydrogen turbopump, which operates at a nominal power level of $14\ MW$, and has been tested at $21\ MW$ [1] to reproduce off-design conditions. To provide some context for this value, it is higher than the power of two high-speed trains operating at full speed. Due to this and other factors, testing such devices can be highly complex and expensive.

The need for such devices as turbopumps arises from the theory behind Launch Vehicles. An LV is all about mass budgets. By taking a look at the rocket equation, we can see that:

$$\Delta v = I_{sp} \cdot g_0 \cdot \ln\left(\frac{M_0}{M_f}\right) \tag{1.1}$$

where I_{sp} represents the specific impulse of the rocket, g_0 the universal gravitation constant and M_0 and M_f the initial and final mass of the LV. All these parameters directly affect the vehicle's velocity change, Δv, which depends on the orbit to be achieved.

Given that Δv is a constant orbit-dependent requirement, I_{sp} is an engine performance parameter, and g_0 is constant, to maximize impulse when designing a launch vehicle, the ratio of initial to final mass should be optimized. Furthermore, by noting the following relations:

$$M_0 = M_{dry} + M_{prop} + M_{payload} \tag{1.2}$$

and:

$$M_f = M_{dry} + M_{payload} \tag{1.3}$$

where M_{dry} represents the dry mass of the LV (i.e., the mass of the LV without propellants) and M_{prop} represents the propellant mass. It is readily apparent that maximizing the mass ratio, and hence the payload capabilities, is achieved by maximizing the propellant-to-structural mass ratio.

The propellant tanks account for a considerable fraction of the LV's structural mass. The higher the pressure at which the propellants are stored, the greater the thickness of the tanks needed to contain that pressure. Therefore, given the substantially high operating pressures inside the combustion chambers, it is unfeasible, from a mass budget perspective, to use a pressure-fed rocket engine, which requires the tank pressure to match the combustion chamber pressure. This would result in massive tanks, reducing (or even eliminating, in extreme cases) the launch vehicle's payload capacity.

To solve this problem, rocket engines have turbopumps. Through a series of complex thermodynamic processes, they allow the propellant stored at low pressure to reach the required pressure for injection into the combustion chamber. These are complex devices, composed of a turbine that generates power to drive a pump. The turbine itself also needs to be driven, which requires meticulous control, as only a small fraction of the propellants need to be combusted to extract heat (generating enthalpy) from the cycle, which then drives the turbine. Given these sequential processes, the turbopump is the most complex element to design, with multiple nuances that must be addressed.

The turbine design itself presents multiple challenges, particularly in blade design, power-torque efficiency, and mass optimization, as it also contributes to the LV's dry mass. The performance parameters are often supported by Computational Fluid Dynamics (CFD) simulations and empirical models. The latter often relies on tuning parameters that are optimized using test data. Additionally, dynamic effects such as the fluid-structure interaction and acoustic phenomena are challenging to predict, even with extensive CFD simulations. Such parameters require realistic testing conditions and corresponding instrumentation. This becomes increasingly important as these phenomena are precisely the source of most anomalies observed in turbine operation.

Due to the need to assess these factors and optimize existing models, testing is crucial in the development phase of every LV. To address this problem, this research presents a preliminary design for a flexible facility that aims to provide support for testing at a higher representativeness level than existing solutions.

2

Background

This chapter presents the foundation for the research, framing the work within its associated scientific domain and introducing the methodology for addressing the problem. Understanding the current solutions to the problem this research proposes to solve, their limitations, and their impact on system performance is vital to determine an adequate methodology and proposed solutions.

2.1. State of the art

The number of existing facilities for rotating machines worldwide is so high that it would be impossible to analyze all of them and their design characteristics. Therefore, the need to categorize test facilities arises. This categorization can be done in several ways, taking into account each facility's purpose and specific design parameters. This section aims to present how these facilities are categorized depending on the maturity level of the intended test specimens. Furthermore, to present a list of test facilities whose design aspects or purpose have a significant interest for the application of this research.

2.1.1. Technology Readiness Level (TRL)/Background knowledge

It has been introduced that iterative development is highly dependent on testing. However, it is still left to determine which testing needs to be performed. The answer to this question is based on the Technology Readiness Level (TRL): a concept defined by NASA and later adapted by ESA that aims to quantify the maturity of the development of a project, on a scale from 1 to 9. [2]

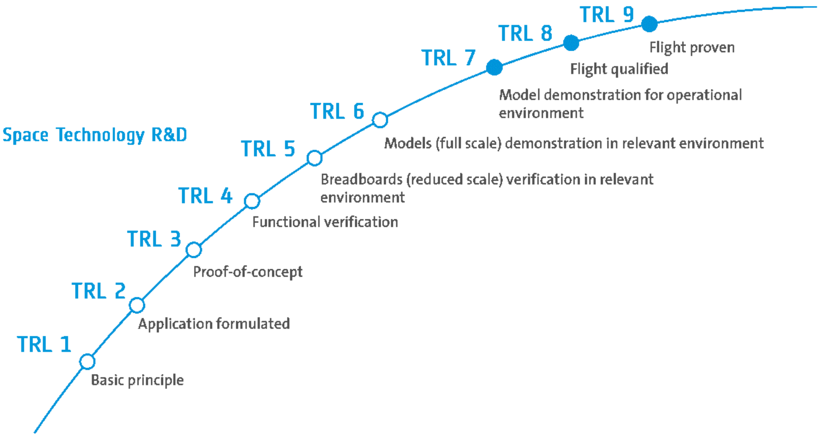

Figure 2.1: TRL by ESA's definition [3]

For each of these maturity levels, different tests with different objectives need to be performed. Therefore, test facilities also evolve with the TRL. An overview of the test characteristics and facilities can be found in the literature [4]:

- **TRL 1-3** - At this level, the objectives lie in proof of concept and the assessment of basic operational principles, as well as academic tests, to investigate specific flow phenomena, for example. For this, lab-scale test facilities are often used, which usually provide the test object (typically a turbine component) with air as the driving medium in a blowdown system (the air is kept at a specified pressure in a tank and fed directly to the turbine).
- **TRL 4-5** - At these levels, the goal is to validate components in a relevant environment. The goal is to assess individual interfaces on quasi-representative conditions. These conditions are more representative than in lab-scale testing. However, some parameters, such as the pressure ratio and the operating medium, are still not replicated (since tests are usually conducted under cold-flow conditions).
- **TRL 6 (Focus of the research)** - At this level, the objective is to demonstrate the full-scale model in a relevant environment. In the case of rocket engine turbines, this typically involves testing the turbine or turbopump under representative conditions. This is achieved by using scaling methods that fix non-dimensional parameters. For all of these objectives to be met, these tests must be performed in hot conditions.
- **TRL 7-8** - At these levels, the system needs to be demonstrated in an operational environment. In the context of this research, this translates into Power-Pack-Assembly (PPA, i.e., Turbopump and its enthalpy source, which may take the form of a gas generator or a preburner) and Engine-level testing at full-scale (i.e., nominal) conditions. Large-scale test facilities capable of delivering high mass flow rates at high pressure and temperature are used for these tests.
- **TRL 9** - At this TRL, the system needs to be qualified and accepted for flight. This is done through stage ground (on the launch pad) and launch vehicle flight testing.

As mentioned, the facility is intended to provide support for turbine testing at TRL 6. Given this TRL level, this facility must be capable of testing the turbine in a relevant environment. This essentially means a fully representative test of a geometrically full-scale turbine at relevant operating conditions, using scaling methods by fixing non-dimensional parameters. At this level, the main objectives of the test campaigns are to assess the following points:

- Thermal behaviour (i.e., thermal loading) of the turbine
- Acoustic behaviour of the turbine
- Fluid-structure interaction (i.e., loading in terms of pressure ratio and rpm)
- Power-torque efficiency

To achieve the required representativeness to fulfill the test objectives at TRL6, the facility needs to be designed to replicate key parameters of interest. Doing so presents various challenges that must be addressed in the design process.

All the specific parameters that need to be replicated, along with the rationale for the scaling methodology, will be presented in a dedicated section. However, for introduction purposes, it is useful to keep in mind that, from the objectives, it is possible to present an initial view of the parameters that need to be replicated:

- Operating temperature - linked with assessing the thermal behaviour
- Rotational speed - to assess the acoustic behaviour
- Pressure ratio - that contributes to the acoustic behaviour and the flow expansion characteristics
- Medium - which directly contributes to all of the parameters to be assessed

2.1.2. Existing test facilities

Testing rotating machinery is standard across multiple industries. This is not only in aerospace applications, as in this thesis, but also in various fields, such as automotive, oil and gas, and even wind turbines. Companies need to test their models to qualify them and better understand their performance and limitations.

Due to this need for testing, multiple test facilities have been built around the world, each one with the key design parameters that make it unique. This chapter provides an overview of existing test facilities and highlights their limitations, underscoring the need for a new test facility that fully meets the requirements for this work.

Given the vast number of test facilities documented in the literature, the literature review focused on a general view of facilities for aerospace applications. The vast majority of the studied facilities were designed for a specific program, with key design parameters that set them apart from the general layout.

Reports providing specifications for multiple facilities were found, so the research was narrowed down to a select group of facilities that represented various test objectives. An overview of the facilities that were studied more extensively can be observed in the following table:

Table 2.1: Overview of existing facilities that support testing of rotating turbo machines

Test Facility	Owner	Reference(s)
NASA-MSFC Turbine Test Equipment	NASA	[5]
ORCHID Test Facility	TU Delft	[6]
LUMEN Test Facility	DLR	[7], [8]
WaterFlow Cavitation Test Facility	University of Michigan	[9]
Cavitation Test Facility	Centrospazio	[10]
Altitude Test Facility	ILA Stuttgart	[11], [12]
DLR Göttingen Test Facility	DLR	[13]
MIT Blowdown Test Facility	MIT	[14], [15]
Turbine Similarity Test Facilities (KARI)	Korea Aerospace Research Institute	[16], [17]
High-Speed Rotating Turbine Rig CT-3	Von-Karman Institute	[18], [19]
ArianeGroup's heritage test facilities	ArianeGroup	[20]

The number of existing test facilities is too high for a description of the design parameters of interest for each one of them to be reported. Therefore, it was decided to classify the facilities on the following criteria:

- Driving Media (Temperature, Composition, Pressure) - which is then classified in terms of temperature (hot/cold), composition (matches the nominal operation gas or uses an alternative media), and pressure (high/low). Following the same logic as the composition, a facility is considered high-pressure and/or high-temperature if it matches the operating conditions for which it was designed.
- Pressure ratio - On whether it is capable of replicating the pressure ratio of nominal operation, or operates at a scaled pressure ratio
- Rotational speed (rpm) - Assesses if the nominal rotational speed is achievable when testing in the facility or if this parameter is scaled when testing.
- Test object - which, for this select list of facilities, can be either a turbine, a pump, or the full turbopump.

After analyzing the facilities in Table 2.1 for this criterion, it was concluded that none of them could replicate all operational conditions at turbine-level testing, and each had one or more limitations.

This section will proceed with an analysis of the most predominant limitations, and their impact on the representativeness.

2.1.3. Limitations

Four key limitations that affect the replication of these parameters were found to prevail among existing test facilities:

- The driving media is air, often blowdown from a tank, which implies it is also limited to its storage pressure, or an alternative gas (for example, gaseous nitrogen - GN_2 - or gaseous hydrogen - GH_2).

- The facility, namely its feed system is only prepared for cold flow conditions
- The attainable pressure ratio in the facility is much lower than the one experienced at nominal operation
- The test facility is prepared to receive a turbopump rather than a turbine as the test article

By taking a more detailed look at the theory underlying the limitations, a better understanding of why they prevent the test objectives from being met can be achieved. Therefore, in this section, an explanation of each of the mentioned limitations will be provided.

2.1.4. Cold-flow and alternative driving media

There are multiple types of driving media used across turbomachinery test facilities. They can be classified by temperature, composition, and pressure, with the criterion being whether they replicate the same driving media used in the nominal operation of the tested object or use an alternative driving media.

Most test facilities are designed for cold testing. In turbine testing, this usually means an alternative cold gas is used to reduce the costs and logistics associated with the test. This, however, comes with a loss of representativeness. First, it is impossible to assess how the turbine's structure reacts to thermal loading, including temperature gradients and peak temperatures observed during nominal operation.

Additionally, if a lower inlet temperature is provided, it can significantly increase the complexity of achieving the same temperature (and therefore also pressure) ratio. For example, if the inlet temperature is 300K and the pressure ratio is 20, which is not far from typical rocket engine turbine temperature ratios, expansion to cryogenic conditions would be required, which is unrealistic and unfeasible. This leads to difficulty achieving the required rpm level, which is vital for assessing fluid-structure interaction.

Finally, when changing the gas that drives the turbine, the gas properties change, with a direct impact on the isentropic relations and the non-dimensional parameters. This directly increases the complexity of achieving complete similarity through a scaling approach, as the fixation of the non-dimensional parameters becomes more challenging.

The trend observed was that, for low-TRL test facilities such as the MIT blowdown test facility, cold air or an alternative gas is used, but only in cold conditions. In higher-TRL test facilities, hot-gas testing is predominantly used, such as at the Altitude test facility in ILA Stuttgart, but the only available medium is air, which is preheated in a dedicated subsystem. In the rare cases in which a combustor is present in the facility, other parameters, such as the pressure ratio, were not replicated.

2.1.5. Pressure ratio

The assessment in terms of pressure ratio is relatively straightforward. A test facility is classified as capable of replicating or reaching values close to the turbine operating point. What is often observed is that test facilities operate at a much lower pressure ratio than the nominal value. This leads to a loss of representativeness in flow velocities, as a lower pressure ratio implies a lower expansion and, therefore, a mismatch in the velocity triangles and flow phenomena. It also directly affects efficiency, which varies with the pressure ratio, as shown in the results for a test campaign for the LE-5 engine fuel turbine [21]:

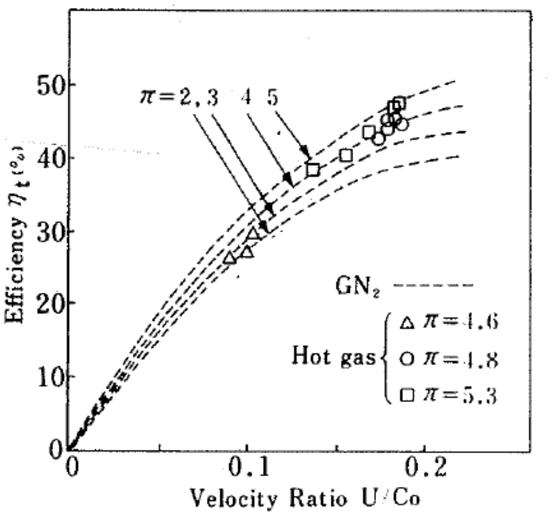

Figure 2.2: JAXA LE-5 LH2 turbine test results [21]

Furthermore, suppose the pressure ratio is reduced below the critical pressure ratio for sonic conditions. In that case, fundamental changes in the flow regime occur, leading to an incorrect assessment of the operating behaviour. The same concern arises regarding the flow velocities and Mach numbers attained, as the behavior of compressibility may be altered and, once again, incorrectly assessed. It will also affect the axial thrust, which depends on the pressure distribution over the stage's structures, and this distribution will be notably different from that experienced in nominal operation. It is important to note that some of these parameters will still be scaled and reduced relative to nominal operation. However, by replicating the pressure ratio, the scaling factors can be correctly predicted and applied during test data processing.

2.1.6. Test object type

Turbomachinery for rocket engine applications is usually tested at various levels, each associated with the TRL level. At low TRL (≈ 1-4), cascade tests are performed in a wind tunnel to obtain data for inspecting flow phenomena and optimizing blade geometry. As technology matures, tests are performed at higher levels of integration, progressing from the turbine level (≈ TRL5-6), then the turbopump (≈ TRL7-8), and finally the engine. Finally, at the highest level of maturity (TRL9), flight testing occurs at the vehicle level.

While some manufacturers include both levels in their development logic, many don't test at the turbine level, skipping it and going directly to turbopump-level testing. This comes with both advantages and disadvantages: if no significant anomalies are observed, it is safe to say that not testing at the turbine level reduces development time and cost, since test planning, operations, and data analysis for this campaign, as tasks that often take several months, would not be performed. However, there are significant disadvantages to not testing at the turbine level. The following can be noted:

- Reduced instrumentation possibilities - due to spatial constraints imposed by the integration of the pump, the turbine, especially its outlet, can't be as heavily instrumented as when tested as a single component. The inability to measure data points in many locations leads to a lower understanding of the system's performance under operation and a more difficult analysis upon failure, as the origin can be harder to track.
- Inability to individually assess the turbine - As the turbine is coupled with the pump, it is not possible to measure the individual performance parameters (efficiency) of the turbine. Additionally, it increases the complexity of thoroughly assessing its behaviour during its transient modes — startup and shutdown.
- More complex assessment upon failure - In case of a failure, it becomes increasingly complex to track the origin of the failure, as it can come from either the turbine or the pump, or the interface

between the two components.

- Higher hardware risk - Upon failure, when testing at the turbopump level, there is a risk of loss of both the turbine and the pump, which inevitably increases the cost of failure.

2.2. Inspiration

Despite the limitations mentioned, the test facilities studied still offer highly interesting design choices that can serve as inspiration for this novel facility. This chapter provides an overview of key design options identified in the literature to inspire the design process in the next chapter.

2.2.1. Flexible interfaces

One key feature of the test facility proposed by this research is flexible interfaces that allow testing different turbines without extensive changes to the test facility. This is vital to the success of iterative development, as multiple design iterations can affect interface geometry. Additionally, this allows the test facility to be used in various programs rather than a ”one-shot” activity, as is frequently observed in the literature. This provides a larger return on investment, making up for eventual increases in cost due to these flexible capabilities in the long run.

Although not the most commonly observed aspect, some facilities described in the literature are also designed to support multiple development programs, with interesting design choices regarding flexibility.

Multiple examples of this can be found in NASA’s Marshall Space Flight Center (MSFC) turbine test equipment (TTE) [5]

- **Variable inlet temperature** - it uses a regenerative thermal matrix, in which the flow that comes out of the storage tanks can go through two different lines: a main line that goes through a heater and a bypass line that does not. Having valves to control the ratio between the mass flows going through the lines it enables an active regulation of the flow temperature, which will be fed to the turbine.
- **Variable length between plenum exit and turbine inlet** - By mounting the feed system on wheels, the pillow block is prepared to receive turbines with various dimensions, by varying the length between the plenum exit (the last component of the feed system) and the turbine inlet.
- **Variable contraction area ratio in the plenum assembly** - In order to control the inlet flow velocity, there is a convergent-divergent section upstream of the test specimen, similar to a nozzle. The convergent component of the plenum has been designed with simple interfaces to allow easy swapping and to allow variation of the contraction area, thereby influencing the inlet flow velocity.

The DLR Göttingen Test Facility [13], provided interesting design choices regarding its wide pressure operating window, and the usage of combustion chamber simulators. A frequent trend observed was the periodic revamping of test facilities to increase their operational capabilities. An example of this is the ILA Stuttgart facility, which was adapted to support engine-level testing in 1998 [12], and more recent studies were already performed in how it can be further upgraded [11].

2.2.2. General design considerations

What was commonly observed was that, aside from some minor changes related to the specific test objectives, the overall layout was very similar across existing test facilities. They were generally composed of the following subsystems:

- Storage and feed system - The tanks where the driving media were stored and the piping system leading from them to the turbine, with air being used for the vast majority of the applications, either heated or cold. For test facilities that preheat the air, it is predominantly done using thermal matrices comprising heat exchangers.
- A pillow block - where the turbine is installed and supported by the bearings. Gearboxes are frequently used, especially when power dissipation mechanisms rated for relatively low rotational speeds, as in water brakes, are used.

- A power dissipation mechanism - A device that can dissipate the power generated in the shaft. Multiple options can be used for this purpose. Lower-power facilities, such as the ORCHID test facility [6], use generators to convert power into electrical energy, which can then be fed into the facility's power network. For higher-power applications, water brakes were the predominant choice, offering power dissipation through water heating achieved through intentional recirculation.
- An exhaust gas guiding system - A piping system that leads the exhaust gas from the turbine into a place where it is stored or disposed of. The system's complexity increases with the physical properties of the outlet medium. For low-pressure medium, it is most often vented from the system or stored in a catch tank.

2.2.3. Inherited Components

To leverage existing knowledge and simplify design processes, components from ArianeGroup's previous programs can be used for the test facility. Namely, gas generators from ArianeGroup's catalogue will be considered in the design of this specific subsystem.

This is done to allow the use of existing resources, reducing the program's overall cost and development time. Additionally, it leaves the focus on the critical subsystems of the facility, for which a higher level of uncertainty remains.

2.3. Problem Statement

Understanding the limitations of the state of the art provides some guidance towards the Research Gap. It follows from a common aspect found to be missing from current facilities: a facility that simultaneously enables representative testing while allowing flexible operating conditions.

2.3.1. Research Gap

The literature review allowed us to conclude that no publicly disclosed test facility can fully replicate the nominal parameters. This does not come as a surprise, as not scaling the operating conditions would lead to power levels that are unfeasible to dissipate while keeping the cost figures and complexity under reasonable boundaries.

It was also noted that the test facilities that most closely replicated operational conditions were those from ArianeGroup's legacy programs. These facilities reproduced the pressure ratio and achieved the operational rpm levels, but used air at medium temperature as the driving medium, which compromises representativeness.

Another common trend observed was that, because the design of most of these test facilities was done with a specific program (for a turbine, pump, or turbopump), the program dictated the requirements. Therefore, while it is possible to test that machine in particular effectively, the flexibility is limited, and significant changes would be needed to accommodate a different test specimen.

However, the opportunity to scale operating conditions to reduce power while still achieving a higher level of representativeness than all facilities with publicly disclosed operating capabilities is theoretically possible. Therefore, the lack of full implementation of flexibility and representativeness in any turbine facility is the research gap this research will address.

Having these limitations in mind, the problem statement of this research can be described as:

The existing test facilities do not fully support representative testing capabilities at hot gas conditions. Rocket engine turbine characterization is therefore limited, which reduces confidence in the system's reliable operation during flight.

2.3.2. Research Objectives

Therefore, the objectives of this research are to provide innovation in this field by achieving a preliminary design for a test facility with the following characteristics:

- **Representativeness** - being able to test standalone turbines, without the presence of a pump, and at an unprecedented level of representativeness, by applying an anchored scaling that preserves the phenomena of interest.

- **Flexibility** - achieving a facility design that is not anchored on requirements derived from a specific program, but rather capable of testing turbines over most of the design domain. The goal is that a turbine does not need to be designed regarding test facility constraints, but rather the test facility shall be adaptable to accommodate turbines with a wide range of operating conditions.

This research lays the foundation for this innovative facility by enabling us to understand the trade-offs in such a design and to assess the feasibility of achieving the representativeness and flexibility it aims to achieve.

2.3.3. Research Questions

The mentioned research objectives allow us to derive the research questions to be addressed in this project. Given that this research focuses on the design of a modular test facility, one main research question was derived.

RQ1 - What is the general configuration of a multi-MW turbine test facility?

To guide towards finding the answer to the main research question, three sub-research questions were identified:

RQ1.1 - How can turbines be tested at reduced power while providing a representativeness level that is sufficient to achieve the similarity required for TRL6?
RQ1.2 – What are the available solutions to dissipate the power generated by the turbine?
RQ1.3 – How can the shaft of the system be supported to allow for a wide range of operating conditions?

2.3.4. Hypothesis

Making use of the knowledge obtained during the literature review, it is possible to draw a hypothesis for the research question.
H-RQ1 - The general configuration follows the one presented in the vast majority of the test facilities studied, with some adaptations to meet the required test conditions. On a top-level view, it is composed of the following sections:

- Propellant storage
- Enthalpy generation device
- Shaft support subsystem
- Test specimen
- Power dissipation mechanism
- Exhaust gas guiding system

And the respective data-acquisition systems and regulation systems.

The following schematic provides a top-level view of the stated systems and their interconnections.

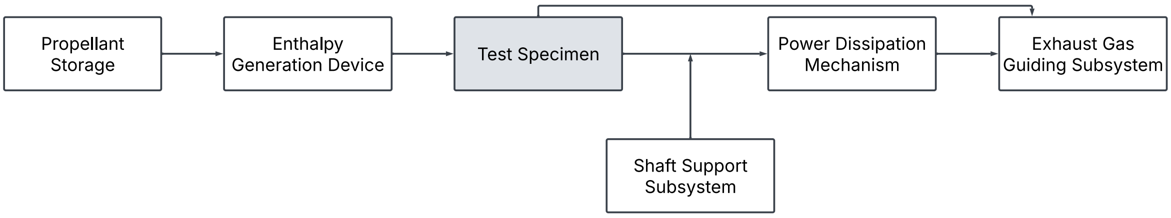

Figure 2.3: Hypothesis for Research Question 1 - General layout of a multi-MW facility

Work will be performed further to specify these subsystems and their connections with greater detail. Such a design will be performed with the research objectives in mind.

2.4. Methodology

To assess the presented hypothesis and ultimately answer the Research Questions, the following plan of activities will be performed:

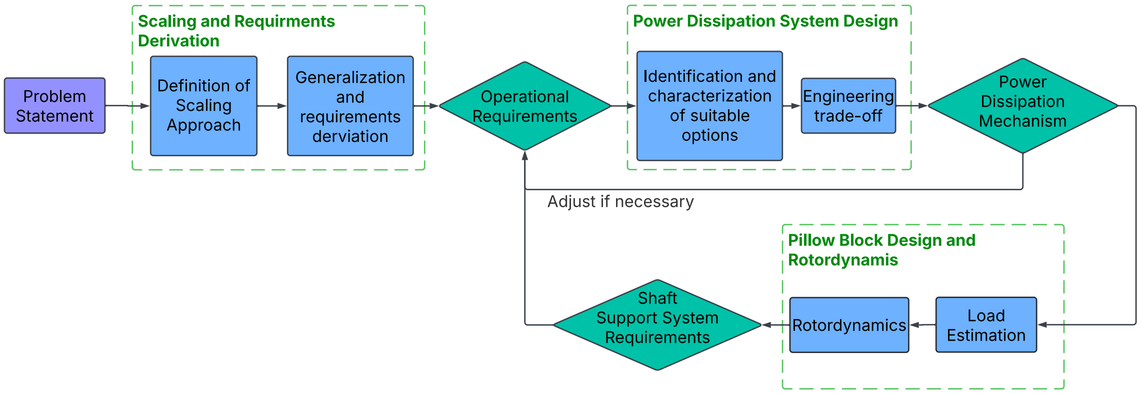

Figure 2.4: Top-Level flowchart with the adopted methodology for the research

As shown in Figure 2.4, the research will be conducted in three phases: the scaling and requirements derivation, followed by the design of the power dissipation system, and finally, the pillow block design and rotordynamics.

2.4.1. Scaling and Requirements Derivation

The objective of this phase is to derive the operational requirements to serve as inputs to other phases. To achieve this, the scaling approach is defined, and a sample of operating parameters for turbines at representative thrust levels is collected.

By applying the scaling procedure to the data points and observing the results, it is possible to generalize and derive the system operational requirements.

2.4.2. Power Dissipation System Design

Having set the system operational requirements, the first critical subsystem is designed: the power dissipation mechanism.

For such a design, the suitable options for such requirements will be identified and characterized. For options that involve customized in-house development, preliminary 0-D and 1-D designs will be conducted to assess their feasibility in meeting the requirements.

After all relevant options are characterized, an anchored engineering trade-off based on a Pareto approach to the traditional Analytic Hierarchy Process [22] will be followed. After all relevant studies are conducted, decision support will be prepared, and a final decision will be made, taking into account the project's specific needs.

By introducing a feedback loop into the test facility design, this research also demonstrates the capabilities of iterative development. The simulation results will provide the researcher with additional knowledge of the system and drive design changes in subsequent iterations, enabling the system to comply with all requirements fully.

2.4.3. Pillow Block Design and Rotordynamics

For the final phase of the project, the pillow block design and rotordynamics will be assessed. Such a process starts with a load estimation in an extreme-case analysis, using the derived operational requirements and the representative turbine sample collected in the first phase.

After the system load estimates are obtained, the Rotordynamics of the system can be analyzed to derive requirements for the shaft support system (bearings), such as load rating, stiffness, damping, and cooling requirements.

Similar to the power dissipation system section, the results will be used to reassess the operational requirements if this section raises questions about their feasibility.

2.5. Structure of the Report

The report is structured in 4 main content chapters, reflecting the different project phases.

Starting with chapter 3 in which the scaling methodology is introduced and used to derive the system operating requirements. The work follows in chapter 4, in which the general layout of the system is presented, along with some brief considerations on the feed system components and design, and the presentation of suitable candidates for enthalpy generation devices for the facility.

After the foundations are set, chapter 5 comes with a detailed characterization of the four different options of power dissipating mechanisms, followed by an engineering trade-off to select the preferred solution for this application.

chapter 6 follows, which starts with an estimation of the loads experienced during the turbine and pump's operation. These loads serve as an input for the rotordynamics and bearing designs that follow. In this second part of the chapter, a geometrical layout of the subsystem is proposed, together with the derivation of the relevant subsystem requirements, namely the bearing stiffness, damping, and lubrication requirements.

As the objectives of the project are accomplished, the Conclusion follows (chapter 7), in which the general takeaways of the studies performed are summarized. This section is followed by the recommendations for future work (chapter 8), in which the key action points for further research are identified and described.

3

Derivation of System Requirements

In this chapter, the methodology used to decide upon the system operational requirements is presented. Furthermore, the final decisions on these requirements are made and presented, constituting the final product of this chapter and an input for subsequent chapters.

3.1. Top Level Requirements

The Top-Level Requirements (TLRs) are derived from the motivation behind this work. The main goal is to develop a test bench concept that is flexible enough to accommodate multiple test objects (which can take the form of a turbine or a turbopump). For this reason, the TLRs are rather general and are followed by a more detailed set of requirements for specific applications, as a result of a scaling exercise.

- **TLR1** - The test facility shall be able to perform testing of high-power turbines, in the power level required for 1 MN class rocket engines of varied turbomachinery cycles.
- **TLR2** - The test facility shall be capable of operating with both cold and hot media
- **TLR3** - The test facility shall be able to operate with at least the following media: hydrogen and oxygen combustion gases, methane and oxygen combustion gases, and gaseous nitrogen
- **TLR4** - The test facility shall favor low operational complexity and be able to support testing rapidly upon demand.
- **TLR5** - The test facility shall be designed and run within a defined budget (TBD).

3.2. Scaling Approach

As mentioned, these are the main requirements that motivate the construction of such a test facility. The remaining operational requirements are case-specific, i.e., will vary with the test object for each campaign. To determine them, a scaling methodology must be followed to ensure the required level of similarity is achieved.

In this section, the selected scaling approach will be presented. Additionally, data from the Vulcain 2 FTP (Fuel Turbopump) turbine will be used as an illustrative example of the impact of scaling on operating parameters.

The ultimate objective of this scaling exercise is to obtain the inlet and outlet parameters that are required to achieve complete similarity at a reduced power level. This significantly reduces testing costs and complexity by enabling a broader range of low-cost power-dissipation mechanisms, which is one of the key systems driving the cost of the facility.

3.2.1. Scaling Parameters

To select among the different scaling options, input from a previous study using Computational Fluid Dynamics (CFD) is needed to understand how the changing parameters have an impact on the phenomena of interest. Such a procedure was followed in a study by ArianeGroup, which served as input for this research. This study concluded that multiple scaling approaches have sufficient agreement with CFD. However, there is one that better suits the application in terms of the similarity goals: the Baljé Ns, Ds [23], and the Mach number of a relevant velocity scaling.

For this approach to be used for scaling, the mentioned parameters shall be fixed, while the parameters that scale with them shall be varied. The parameters are, as mentioned, the specific speed (N_s):

$$N_s = N\frac{Q^{1/2}}{\left(\frac{\Delta h_s}{g_0}\right)^{3/4}} \tag{3.1}$$

where N is the turbine rotational speed in rpm, Q the volumetric flow rate in m^3/s and Δh the adiabatic specific enthalpy drop across the turbine, in J/kg.

The specific diameter is given by:

$$D_s = D\frac{\left(\frac{\Delta h_s}{g_0}\right)^{1/4}}{Q^{1/2}} \tag{3.2}$$

where D represents the Diameter of the machine in m and g represents the gravitational acceleration in m/s^2.

In this form, these parameters are not purely non-dimensional. Alternative definitions allow for such parameters to be written in a truly non-dimensional form [24]. However, to be consistent with [23], and its equations for approximating the efficiency curves (for which existing routines were used), the current form in empirical units will be adopted. This leads to the following dimensions.

$$[N_s] = s^{-1}\frac{(ft^3/s)^{1/2}}{\left(\frac{ft}{ft/s^2}\right)^{3/4}} = ft^{3/2}s^{-1} \tag{3.3}$$

Please note that the rotational speed is non-dimensional but should be handled in rpm, not rad/s, for consistency with the methodology in [23].

$$[D_s] = ft\frac{\left(\frac{ft}{ft/s^2}\right)^{1/4}}{(ft^3/s)^{1/2}} = ft^{-1/2}s \tag{3.4}$$

For the Mach number, a relevant velocity must be chosen. The criteria for this choice were to select a velocity that can be easily tuned by the inlet medium, therefore making it simpler to achieve Mach similarity. For this reason, the spouting velocity - c_0 - was chosen:

$$c_0 = \sqrt{2c_pT_{in}\left[1-\left(\frac{1}{\Pi_{ts}}\right)^{\frac{\gamma-1}{\gamma}}\right]} \tag{3.5}$$

The Mach number at the inlet of the turbine is then given by:

$$M_{c_0} = \frac{c_0}{A_{son}} = \frac{\sqrt{2c_pTt_{in}\left[1-\left(\frac{1}{\Pi_{ts}}\right)^{\frac{\gamma-1}{\gamma}}\right]}}{\sqrt{\gamma RTt_{in}}} \tag{3.6}$$

In the case of hot testing, and in accordance with the test objectives at TRL6 (Figure 2.1.1), the following parameters shall remain within a small margin of the values experienced in nominal operation.

- Inlet temperature - to represent the material response to extreme temperatures and temperature gradients observed during regular operation, the inlet temperature needs to be replicated.

- Driving media - in the specific case of TRL 6, the system shall be tested in a relevant environment. Translated to this specific application, this means the same driving media shall be used, even though at reduced pressure. Since, under ideal gas conditions, the gas parameters — specific heat at constant pressure (c_p) and the gas constant (γ) — depend primarily on temperature and gas composition, they are also considered inputs.
- Rotational Speed - It is an objective to assess the acoustics and the fluid-structure interaction at TRL6. To meet that objective, the rotational speed needs to be replicated. This matching is governed by N_s similarity, which yields a perfect match to nominal conditions in hot-gas testing and a reduced rotational speed in cold testing.

3.2.2. Scaling Metholodogy

To perform the scaling, the parameters N_s and D_s, as well as the Mach number, are held constant at the values observed in nominal operation, while their components can vary.

It is also important to recall the power equation, as this is the ultimate objective of the scaling:

$$P = \eta_{ts}\dot{m}c_p\Delta T_t \tag{3.7}$$

where η_{ts} is the overall total to static efficiency across the turbine, $\dot{m}$ is the turbine operating mass flow rate in kg/s, which is a free scaling parameter, and ΔT_t is the total temperature drop over the turbine, in K.

Using isentropic relations, Equation 3.7 can also be written as a function of the pressure ratio:

$$P = \eta_{ts}\dot{m}c_p T_{in}\left[1 - \Pi_{ts}^{-\frac{\gamma-1}{\gamma}}\right] \tag{3.8}$$

where Δh_s is the adiabatic enthalpy drop Π_{ts} is the total to static pressure ratio, i.e:

$$\Pi_{ts} = \frac{p_{t,in}}{p_{s,out}} \tag{3.9}$$

The concepts of adiabatic enthalpy drop (Δh_s) and effective enthalpy drop (Δh_{eff}) can also be introduced, allowing one to obtain a format which is more easily related to the Baljé parameters as:

$$\Delta h_s = c_p T_{in}\left[1 - \Pi_{ts}^{-\frac{\gamma-1}{\gamma}}\right] \tag{3.10}$$

And:

$$\Delta h_{eff} = \eta_{ts}\Delta h_s \tag{3.11}$$

which represents no more than a correction to the enthalpy drop to account for efficiency.

Therefore, Equation 3.7 can then be also written as:

$$P = \eta_{ts}\dot{m}\Delta h_s = \dot{m}\Delta h_{eff} \tag{3.12}$$

To test at reduced power, the only suitable parameter to tune is the mass flow rate. This is because assessing efficiency is one of the test objectives; therefore, it must be kept at a similar level. Furthermore, changing the adiabatic enthalpy drop is not feasible if similarity is to be maintained, as it would require either changing the inlet temperature or the pressure ratio, both of which are essential for assessing fluid-structure interaction and ensuring flow-expansion similarity.

To address this scaling and ensure the design point remains unchanged, the previously mentioned Baljé non-dimensional parameters (N_s and D_s) are introduced. Using the volumetric flow rate and the rotational speed as tuning parameters, they ensure that the Baljé design point remains unchanged.

The Mach number is also included to ensure the compressibility effects are correctly represented, and the flow field has similar characteristics, by fixing, together with the Gas properties (γ, R, and c_p), the total to static pressure ratio - Π_{ts}:

$$\Pi_{ts} = \left(1 + \frac{\gamma - 1}{2} M_{c_0}^2\right)^{\frac{\gamma}{\gamma-1}} \tag{3.13}$$

Subsequently, D_s comes in to assure flow similarity, by tuning the volumetric flow rate - Q - to compensate any potential differences in the diameter of the turbine and the gas parameters as:

$$Q = \frac{D_{tip}^2 \left(\frac{\Delta h_s}{g_0}\right)^{1/2}}{D_s^2} \tag{3.14}$$

The static pressure at the outlet comes from a convention: it assumes that the ratio between the total and the static pressure remains constant when scaling and is equal to the one experienced in nominal operation:

$$p_{s,out} = \left(\frac{p_{s,out}}{p_{t,out}}\right)_{nom} p_{t,out} \tag{3.15}$$

This is particularly relevant for defining the scaling limitations, as in this initial design, no vacuum system will be added downstream of the turbine. This limits the outlet total pressure to ambient values.

The total pressure to be fed into the turbine is given by:

$$p_{t,in} = \Pi_{ts} p_{s,out} \tag{3.16}$$

Given that the design point is dictated by the Baljé parameters, which are kept constant, the efficiency matches the nominal value, and therefore Δh_{eff} is also matched.

Therefore, the total temperature at the outlet is:

$$T_{t,out} = T_{t,in} - \frac{\Delta h_{eff}}{c_p} \tag{3.17}$$

The static temperature must also be determined to compute the static density at the outlet using the ideal gas law. It comes from isentropic relations as:

$$T_{s,out} = T_{t,out} \left(\frac{p_{t,out}}{p_{s,out}}\right)_{nom}^{\frac{\gamma-1}{\gamma}} \tag{3.18}$$

Thus, the static density, ρ_s, comes as:

$$\rho_s = \frac{p_{s,out}}{R T_{s,out}} \tag{3.19}$$

And the mass flow rate is finally given by:

$$\dot{m} = \rho_s Q \tag{3.20}$$

The previous equations show that, in hot testing with a similar driving media, the inlet temperature is maintained and the total-to-static pressure ratio is preserved. This results in the static temperature at the outlet that also matches the value in nominal operation. By noting this, Equation 3.19 can be used to display that the inlet total pressure is the tuning parameter for this scaling methodology.

$$\frac{P_{scaled}}{P_{nominal}} = \frac{\dot{m}_{scaled}}{\dot{m}_{nominal}} = \frac{\left(\frac{p_{s,in}}{RT_{t,in}} A_{in} v_{ax}\right)_{scaled}}{\left(\frac{p_{t,in}}{RT_{t,in}} A_{in} v_{ax}\right)_{nominal}} = \frac{p_{t,in-scaled}}{p_{t,in-nominal}} \tag{3.21}$$

To ensure representative test conditions and meet the test objectives at this TRL, the flow velocity v_{ax} and the inlet temperature are set to their nominal values. Therefore, the only parameter that can be used to tune the mass flow rate is the inlet pressure $p_{t,in}$. To ensure similar expansion, the outlet pressure must be scaled accordingly to maintain the same pressure ratio.

It is still important to recall that, in case of a complete similarity on the driving media (i.e., an exact match on the gas parameters - R, γ, and c_p - the vast majority of the parameters will be equal to the ones in nominal operation. The exceptions are the total and static pressures and densities at all locations.

3.2.3. Gas Generator Scaling

Turbines designed for gas-generator cycle rocket engines are usually characterized by relatively high pressure ratios (up to 20, generally) and relatively low mass flow rates when compared to other cycles. Additionally, these engines have limited combustion chamber pressures that do not exceed $100\ bar$ in most cases. A schematic of an engine of such a cycle can be visualized in the following diagram:

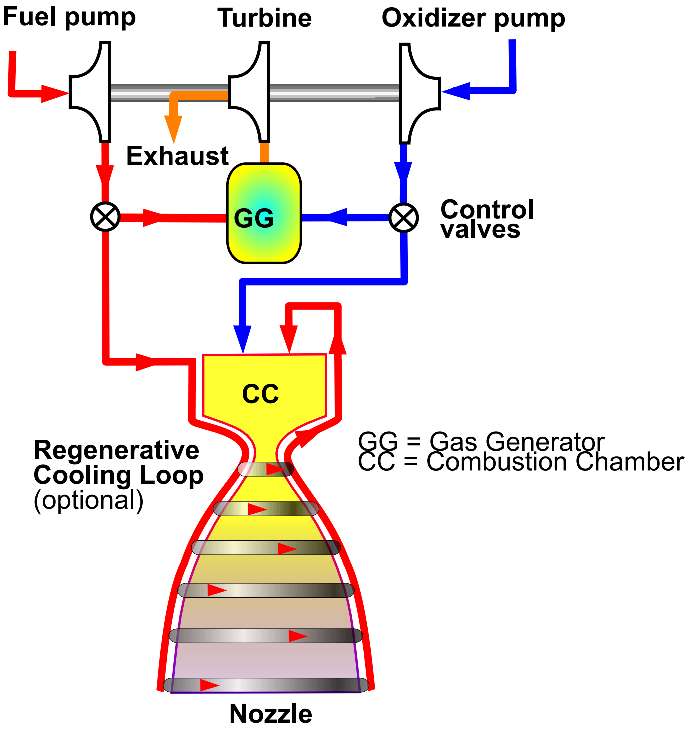

Figure 3.1: Gas generator rocket engine cycle schematic [25]

These design characteristics, along with the undesirable reduction of the outlet pressure below ambient pressure, constrain the scaling process. Therefore, the minimum power required to meet all other requirements is obtained when the outlet static pressure is exactly $1\ atm$. An example of this follows.

Example of Vulcain

An illustration of the effect of the scaling on the power can be done using the data from the upper limit of the operating envelope of the Vulcain 2 fuel turbopump (FTP). This turbine is used as it is in the thrust class of $1\ MN$, and therefore provides a representative check for this study. At the mentioned operating point, the parameters of the turbine are the following [26]:

- $p_{t,in} = 91\ bar$
- $T_{t,in} = 873K$
- $\Pi = 15.5$
- $p_{t,out} \approx 5.87\ bar$
- $P_{output} = 14.29MW$

As previously discussed, scaling brings the static pressure at the outlet down to $1\ bar$. In this application, this means the outlet (and inlet) pressures are reduced by a factor of 5.87. From the ideal gas law:

$$\rho_{s,out,scaled} \approx \frac{p_{t,out,scaled}}{p_{t,out,nom}} \rho_{s,out,scaled} \approx \frac{1}{5.87} \rho_{s,out,scaled} \tag{3.22}$$

Since the volumetric flow rate only depends on the (very slightly changed) gas parameters, it can be assumed that:

$$\dot{m}_{scaled} \approx \frac{1}{5.87} \dot{m}_{nom} \tag{3.23}$$

And since the pressure ratio is also just dependent on the gas parameters, the power level can be given as:

$$P_{scaled} = \frac{\dot{m}_{scaled}}{\dot{m}_{nom}} \cdot \frac{c_{p,scaled}}{c_{p,nom}} \cdot \frac{\Delta T_{t,scaled}}{\Delta T_{t,nom}} P_{nom} \approx \frac{\dot{m}_{scaled}}{\dot{m}_{nom}} P_{nom} \approx \frac{1}{5.87} P_{nom} \tag{3.24}$$

As a result, the scaled power for an N_s, D_s and M_{c_0} scaling would be approximately:

$$P_{scaled} \approx \frac{1}{6} P_{nom} = \frac{1}{5.87} \times 14.29MW \approx 2.43MW \tag{3.25}$$

The complexity of dissipating a power level of $2.43\ MW$ is much lower than for $14.29\ MW$. This makes testing under hot conditions feasible in terms of power dissipation and allows a wide range of power-dissipation mechanisms to be chosen.

3.2.4. Staged Combustion Scaling

Turbines in staged combustion engines have substantially different operating conditions: they are characterized by low pressure ratios (in the order of 1.5), but much higher mass flow rates than in gas-generator engines, since the full mass flow of one propellant (fuel in the case of fuel-rich and oxidizer, on the case of oxidizer rich staged combustion) is used to propelled the turbine, together with a small fraction of the mass flow of the other propellant. Much higher inlet pressures also characterize them, allowing the combustion chambers to operate at much higher chamber pressures than in the gas-generator case. A schematic of such an engine cycle can be visualized in the following figure:

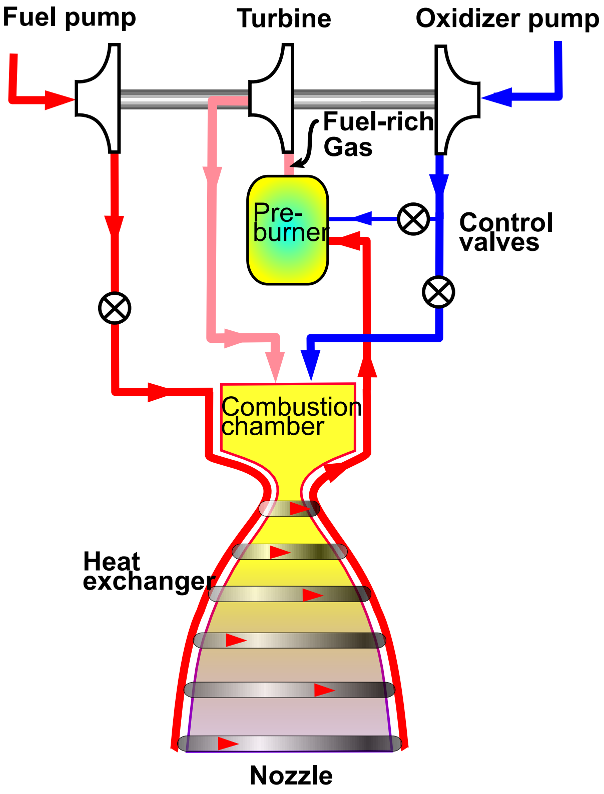

Figure 3.2: Staged combustion rocket engine cycle schematic [27]

This makes the scaling process more challenging, as reducing the outlet pressure to $1\ atm$ would result in a minimal pressure gradient across the turbine, posing new challenges for data acquisition and raising concerns about the effects of a significant Reynolds number mismatch. For these reasons, and given that the scaling factor for gas-generators is, due to the previously mentioned factors, much more limited than that for staged-combustion turbines, the maximum power level will be dictated by a study of the gas-generator engines. Then, for the maximum power level obtained, another study will be conducted to assess the operating window of inlet and outlet pressures for staged combustion engines while remaining below this power threshold.

Example of LE-7A

JAXA/MHI's LE-7A fuel turbine is used as an illustration, as it is part of a staged combustion engine in the power level of $1\ MW$. The design parameters of this turbine follow [28]:

- $p_{t,in} = 209\ bar$
- $T_{t,in} = 701K$
- $\Pi = 1.6$
- $p_{t,out} \approx 129\ bar$
- $P_{output} \approx 14.67MW$ (estimated)

This example perfectly illustrated the scaling capabilities of the staged combustion cycle, as the outlet pressure can be scaled approximately 129 times, leading to a reduced power level of:

$$P_{scaled} \approx \frac{1}{129} P_{nominal} \approx 114\ kW \tag{3.26}$$

It is important to recall that, although it is physically possible to operate, scaling to such high factors raises concerns about flow similarity. Such a scaling factor leads to a Reynolds number mismatch of several orders of magnitude, which, depending on the application, may be excessive and prevent the test objectives from being met.

3.3. Design Space

As previously mentioned, despite the required flexibility, the motivation for this test facility is to conduct hot-gas tests at the turbine level at TRL6 for turbines integrating engines with a thrust class of $1\ MN$. Therefore, it is still fundamental to understand the operating window (in terms of N_s and D_s for this particular application) and to use it to derive specific requirements for the facility design. The design space is a product of the previous exercise, together with some assumptions anchored in data from existing turbines integrating rocket engines in similar thrust classes.

This data, and the respective ROM scaling results, are presented in the following tables:

Table 3.1: Turbine dataset

(a) Full-Scale Turbine data for engines in the 1 MN thrust class

Engine/TP data						Turbine data						Reference(s)
Manufacturer	**Engine**	**Cycle**	**Propellants**	F_T **[MN]**	**TP type**	Π_{tt}	P_{out} [MW]	$p_{t,in}$ [bar]	$T_{t,in}$ [K]	**rpm**	$\dot{m}$ [kg/s]	
ArianeGroup	Vulcain	GG	LOX/LH$_2$	1.1	FTP	17.4	11.41	78.5	875	34070	5.4	[29, 30]
					OTP	14.1	3.076	63.5	875	13290	N.A.	[29, 31]
ArianeGroup	Vulcain 2	GG	LOX/LH$_2$	1.3	FTP	15.5	14.29	91	873	35680	6.0	[32, 33, 34]
					OTP	12.0	5.13	72	873	12660	N.A.	[35]
MHI / JAXA	LE-7A	SC	LOX/LH$_2$	0.844	FTP	1.6	N.A.	209	701	42300	35.4	[28, 36]
					OTP	1.4	N.A.	196	707	18300	16.4	[28, 36]
MHI / JAXA	LE-9	EX	LOX/LH$_2$	1.47	FTP	8.5	N.A.	83	443	41600	9.1	[28, 37]
					OTP	2.5	N.A.	9.4	318	17000	8.3	[28, 37]

Note: Cycle abbreviations—GG: gas generator; SC: staged combustion; EX: expander.

(b) Full-scale vs. scaled parameters for 1 MN-class engine turbines

Engine	**Turbine**	$\dot{m}_{nom}$ **[kg/s]**	$\dot{m}_{scaled}$ **[kg/s]**	$p_{t,in-nom}$ **[bar]**	$p_{t,in-scaled}$ **[bar]**	P_{nom} **[MW]**	P_{scaled} **[MW]**
Vulcain	Fuel	5.4	0.31	78.5	4.51	11.41	2.529
Vulcain	Oxidizer	1.46*	0.10*	63.5	4.50	3.076	0.683
Vulcain 2	Fuel	6.0	0.39	91.0	5.87	14.29	2.434
Vulcain 2	Oxidizer	2.15*	0.18*	72.0	6.00	5.13	0.855
LE-7A	Fuel	35.4	22.13	209	130.63	14.67*	0.112*
LE-7A	Oxidizer	16.4	11.71	196	140.00	5.0*	0.035*

Notes: (i) Scaled quantities defined as $p_{t,in}^{\text{scaled}} = p_{t,in}/\Pi_{tt}$, $\dot{m}^{\text{scaled}} = \dot{m}/\Pi_{tt}$, and $P^{\text{scaled}} = P_{out}/(p_{t,in}/\Pi_{tt})$ (rounded to three decimals, MW). (ii) $*$ Estimated values: *mass flow* for Vulcain OTP (1.46 kg/s) and Vulcain 2 OTP (2.15 kg/s), following efficiency similarity to FT; *power* for LE-7A FTP (14.67 MW) and LE-7A OTP (5.0 MW). (iii) LE-9 entries are intentionally omitted due to the unlikelihood of future developments of expander-cycle engines at these power levels.

Unfortunately, only four engines (corresponding to 8 turbopumps and 8 turbines) met the thrust criterion ($1 \pm 0.5\ MN$), and there was insufficient available literature detailing the turbine parameters required for the scaling methodology to be applied to a larger sample.

However, despite its limitations, the sample provides a good representation of cycles, presenting the three most widely used turbomachinery cycles for rocket engine applications: gas generator, staged combustion, and expander. What is also unfortunate is that all the turbines are driven by hydrogen-oxygen combustion products, leaving no representation of MethaLOx engines, which would be relevant to the design of the test bench.

Given that there is a good representation of the different mass flow rates and pressure ratios observed across the various cycles, the key difference between these two propellant combinations that is not being assessed is the gas parameters.

To understand the extent of the propellant combination effect on these parameters, an analysis using NASA's Chemical Equilibrium with Applications (CEA) [38] software was performed. For this analysis, ideal gas conditions were assumed. Under those conditions, the internal energy of a gas, and thus the gas parameters - γ, c_p, c_v, and R - only depend on its temperature. Therefore, the simulation was run with O/F tuning to achieve a target temperature of $800\ K$, which was considered a representative value given the sample presented in the table above.

Table 3.2: Comparison of LOX/LH$_2$ and LOX/CH$_4$

	LOX/LH$_2$	**LOX/CH$_4$**
O/F ratio	0.811	0.230
R	2277.4	663.4
c_p	8370.1	5110.1
c_v	6092.7	4446.7
γ	1.37	1.15

To assess the real impact of gas parameters on the operating parameters and operating windows, a methodology to derive the Ns-Ds operating windows and resulting thrust and mass flow rate was used. It uses a "worst-case scenario" methodology, where the absolute maximum values are used for each parameter that is assumed. These maximum values are cycle-specific; therefore, the methodology is tuned for each cycle.

3.3.1. Gas Generator

In the case of a gas generator, the following assumptions are made:

- $T_{t,in} = 1000\ K$ - defined as the upper limit, due to material properties of the components of the system.
- $p_{t,in} = 100\ bar$ - the typical chamber pressure limit for gas generator engines, translated into the gas generator itself. The sample corroborates this assumption, along with the literature values for the chamber pressures of other gas-generator cycle engines.
- $\Pi_{ts} = 20$ - as can be observed in the sample, gas generators usually stay under this value, as the attainable chamber pressure on the gas generator is in the order of 100 bar. The flow is then expanded down to a pressure of $5\ bar$.
- $P_{max} = 3\ MW$, following the results of the previous scaling exercise, for gas generators, $3\ MW$ was identified as the maximum attainable value obtained for these conditions, as observed when applying the proposed scaling methodology to the sample.
- $\Omega_{max} = 50000\ rpm$ - this results from a margin applied to the rotation rates of the sample. However, special attention will be paid to verifying the validity of this assumption during the design of the bearings and power braking mechanism.
- $U_{tip,max} = 600\ m/s$ - comes as an engineering rule of thumb for the design of hydrogen turbines. Using the extreme case scenario analysis, this allows us to compute the result for the maximum

diameter, which comes as:

$$U_{tip,max} = \Omega_{max}\frac{D_{max}}{2} \Leftrightarrow D_{max} = 2\frac{U_{tip,max}}{\Omega_{max}} = 2 \cdot \frac{600}{50000 \cdot \frac{2\pi}{60}} = 0.2292\ m \tag{3.27}$$

With these assumptions, it is now possible to plot the power level over the Ns, Ds grid. This process accounts for the efficiency value for each (Ns, Ds) pair, obtained from the Ns-Ds diagram for turbines. This is done following the methodology in [24], which provides a set of equations to reproduce the Baljé diagrams.

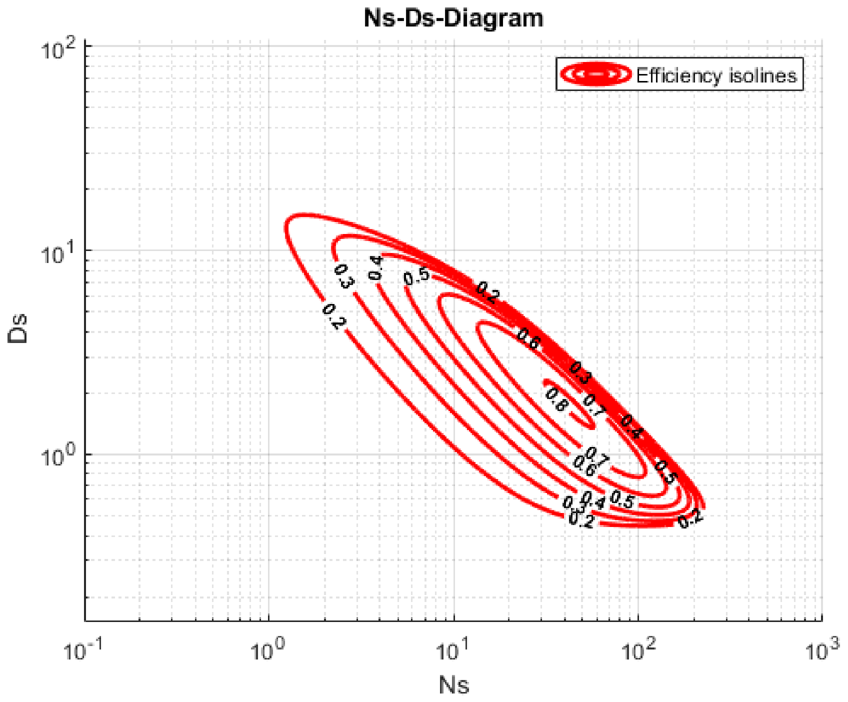

Figure 3.3: Reproduced Ns-Ds diagram for turbines

Among the constraints, the two that set the limits on the design space are Power and Rotational Speed. The other constraints are used in the calculation of these parameters. Recalling the power equation:

$$P = \eta_{ts}\dot{m}\Delta h_s = \eta_{ts}\dot{m}c_pT_{in}\left[1 - \Pi_{ts}^{-\frac{\gamma-1}{\gamma}}\right] \tag{3.28}$$

The adiabatic enthalpy drop is fully defined by the gas properties at $1000\ K$ and $100\ bar$, and the pressure ratio (Π_{ts}). It is also the parameter that drives the difference between the design spaces of the propellant combinations. The following values were obtained:

Table 3.3: Values for the adiabatic enthalpy drop for the studied propellant combinations

Propellant combination	Δh_s [MJ/kg]
HydroLOx	4.329
MethaLOx	2.718

The efficiency (η_{ts}) is obtained from the Baljé diagram for every point of the grid. Points with efficiency below 0.1 are discarded to avoid points with residual efficiency, which do not represent a realistic design space.

The only missing parameter now is the mass flow rate, which, given the fixed diameter, comes directly from D_s in the form of Equation 3.14 as:

$$\dot{m} = \rho_{s,out} Q \left(\frac{ft}{m}\right)^3 = \rho_{s,out} \frac{D_{tip}^2 \Delta h_s^{1/2}}{D_s^2} \left(\frac{ft}{m}\right)^3 = \frac{p_{s,out}}{RT_{s,out}} \cdot \frac{D_{tip}^2 \Delta h_s^{1/2}}{D_s^2} \left(\frac{ft}{m}\right)^3 \tag{3.29}$$

Note that the conversion term between imperial (ft) and SI units (m) is included in the definitions of N_s and D_s, which are expressed in imperial units.

From the extreme case scenario approach $p_{s,out}$ takes the value of:

$$p_{sout} = \frac{p_{t,in-max}}{\Pi_{ts-max}} = \frac{100\ bar}{20} = 5\ bar \tag{3.30}$$

And the static temperature at the outlet of the turbines comes from isentropic relations:

$$T_{s,out} = T_{t,in} \Pi_{ts}^{-\frac{\gamma-1}{\gamma}} \tag{3.31}$$

This is an estimation of the unscaled mass flow rate. As shown before on the scaling methodology, and assuming in this initial phase that the maximum possible static pressure at the outlet is $1\ bar$, the maximum scaling factor for this extreme approach is:

$$SF = \frac{p_{s,out-nom}}{p_{s,out-scaled}} = \frac{5\ bar}{1\ bar} = 5 \tag{3.32}$$

Therefore, the mass flow rate under scaled conditions comes as:

$$\dot{m}_{scaled} = \frac{1}{SF} \dot{m}_{nom} = \frac{1}{5} \frac{p_{s,out}}{RT_{s,out}} \cdot \frac{D_{tip}^2 \Delta h_s^{1/2}}{D_s^2} \left(\frac{ft}{m}\right)^3 \tag{3.33}$$

Having fully derived the equation for the power as a function of N_s and D_s, the same needs to be done for the rotational speed. This is done by replacing the volumetric flow rate in the N_s equation (Equation 3.1) with Equation 3.14, which is a rearrangement of the D_s equation (Equation 3.2). The result is the following:

$$N = N_s \left(\frac{\Delta h_s}{g_0}\right)^{0.5} \frac{D_s}{D} \tag{3.34}$$

The result comes directly in rpm when using imperial units for the diameter (ft) and the adiabatic enthalpy drop (ft^2/s^2).

The rotational speed is then plotted over the Ns-Ds grid to visualize its distribution.

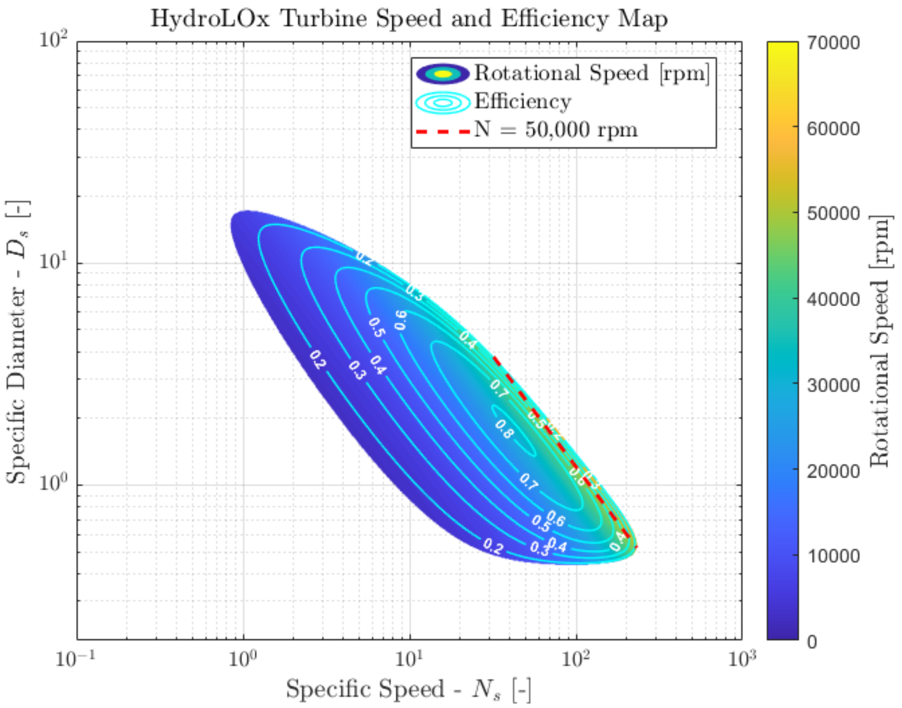

Figure 3.4: Rotational speed contour plot over the Ns-Ds grid for HydroLOx

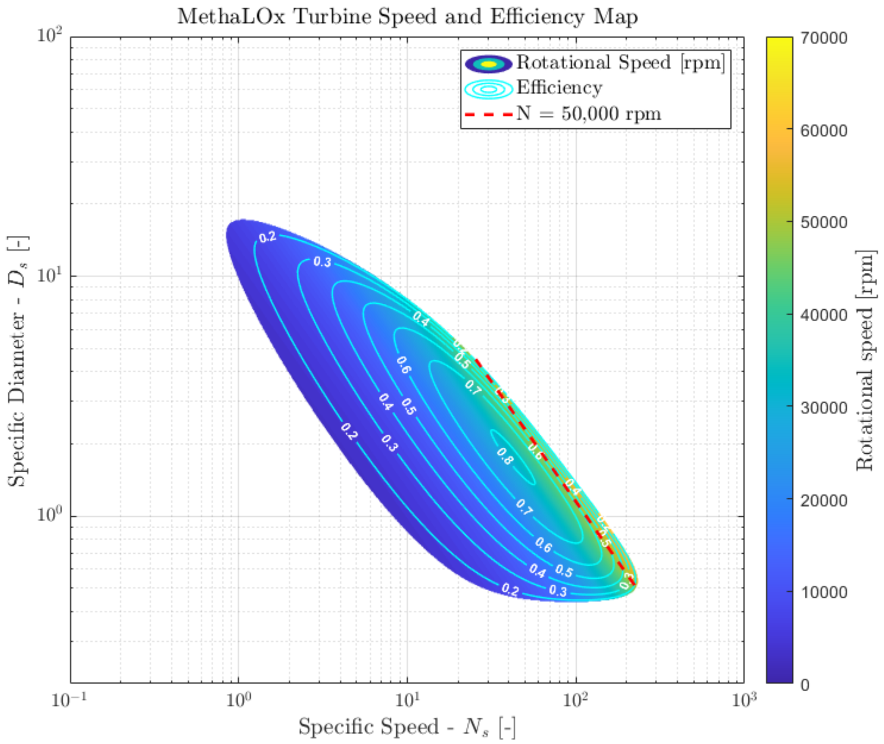

Figure 3.5: Rotational speed contour plot over the Ns-Ds grid for MethaLOx

It is visible that the rotational speed only surpasses the maximum value of $50000\ rpm$ in a small region of the graph, at the upper end of the valid region of N_s. This also corresponds to an area where the efficiency (η_{ts}) is below 50%.

Now that both constraints have been determined, it is possible to plot the design space in terms of power and rotational speed. The following figure shows a contour plot of power (MW) over the Ns-Ds grid. The lines where the limits are reached, i.e., where the power reaches 3 MW (in black) and where the rotational speed reaches the value of 50000 rpm (red), are also plotted.

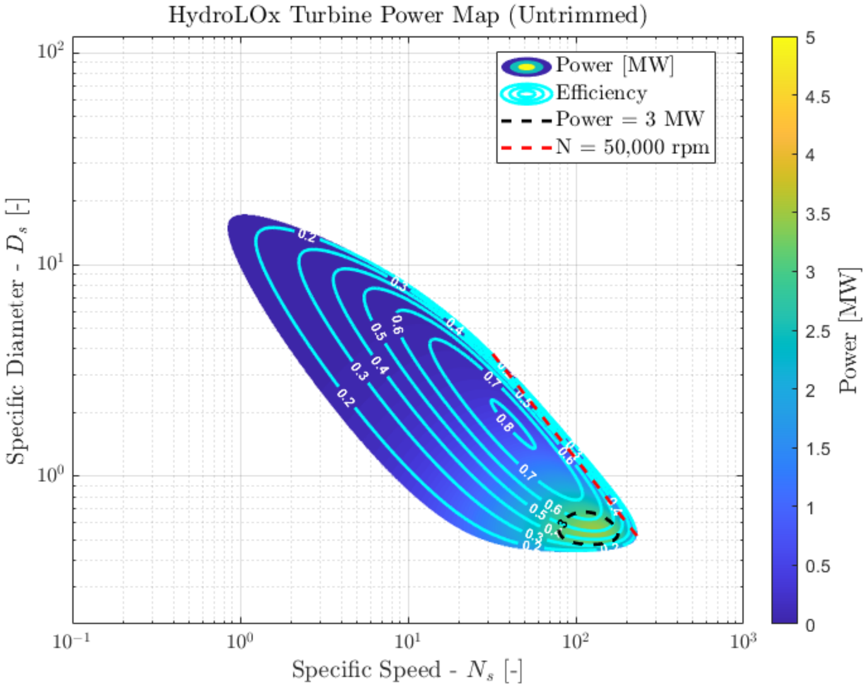

Figure 3.6: HydroLOx - Ns-Ds design space (untrimmed)

To better visualize the design space, this plot can now be visualized after trimming the unacceptable regions. This, once again, follows the rule:

$$\text{Design Space } (N_s, D_s) = (P \leq 3\ MW \quad \& \quad \Omega \leq 50000\ rpm) \tag{3.35}$$

Resulting in the following region:

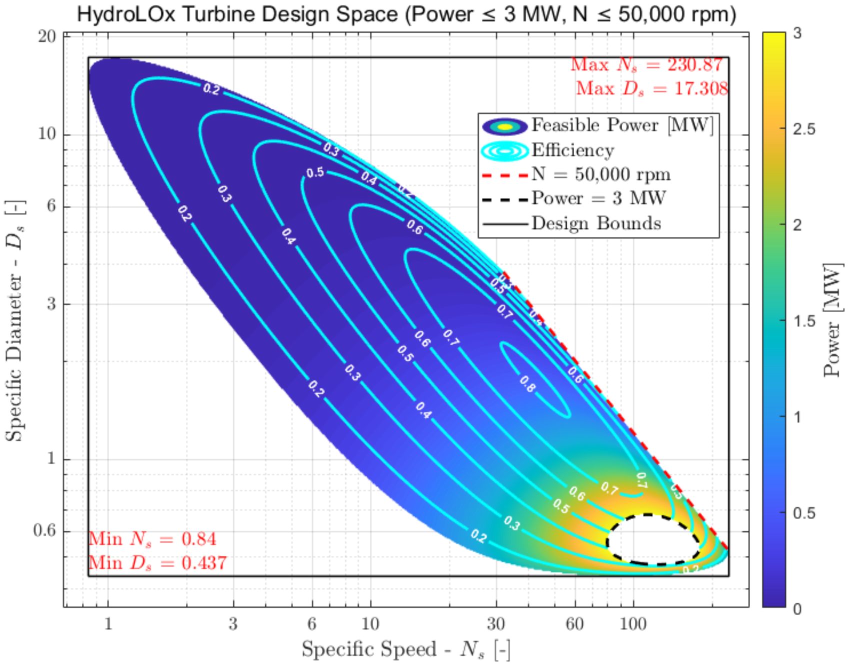

Figure 3.7: HydroLOx - Ns-Ds design space (trimmed)

It is essential to note the physical meaning of the extreme-case analysis. For the operating window, it means that it is guaranteed that the test facility can operate for any turbine whose Baljé parameters are within the specified boundaries, provided that its operating parameters are under the specified limits ($T_{t,in} \leq 1000\ K$ and $\Pi_{ts} \leq 20$).

However, it may still be possible to test a turbine outside the (N_s, D_s) design space in the facility, provided it has lower operating parameters, such as inlet temperature and pressure ratio. This can be assessed by calculating the mass flow rate (to compute the power) and the rotational speed from N_s and D_s, and comparing the results with the facility capabilities.

For methane, the design is more restrictive, as a product of the higher density, leading to higher values of mass flow rate for the same D_s. This effect is notorious in the untrimmed plot:

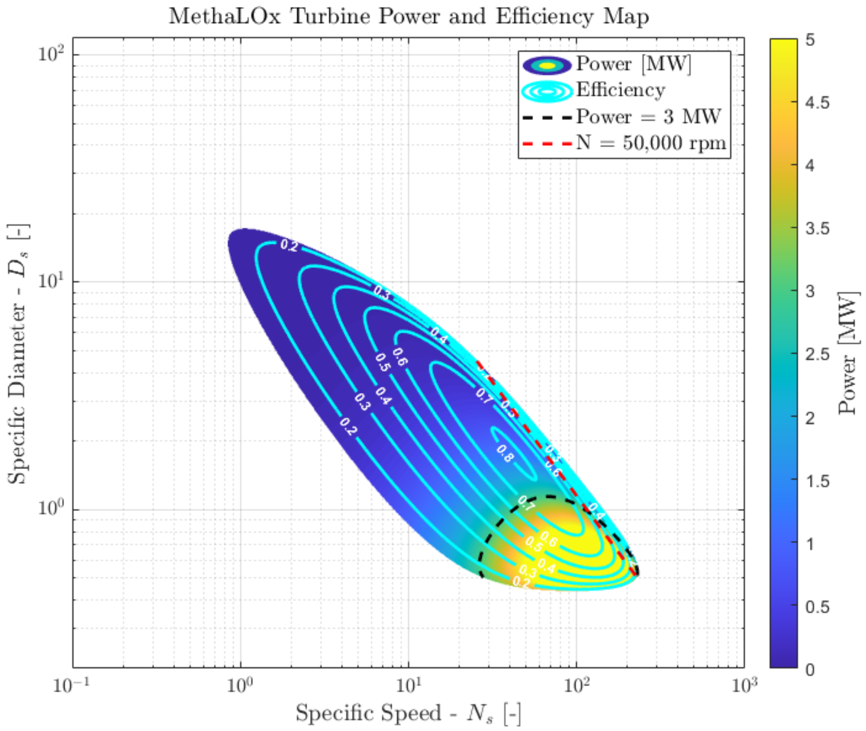

Figure 3.8: MethaLOx - Ns-Ds design space (untrimmed)

And becoming even more visible in the trimmed plot

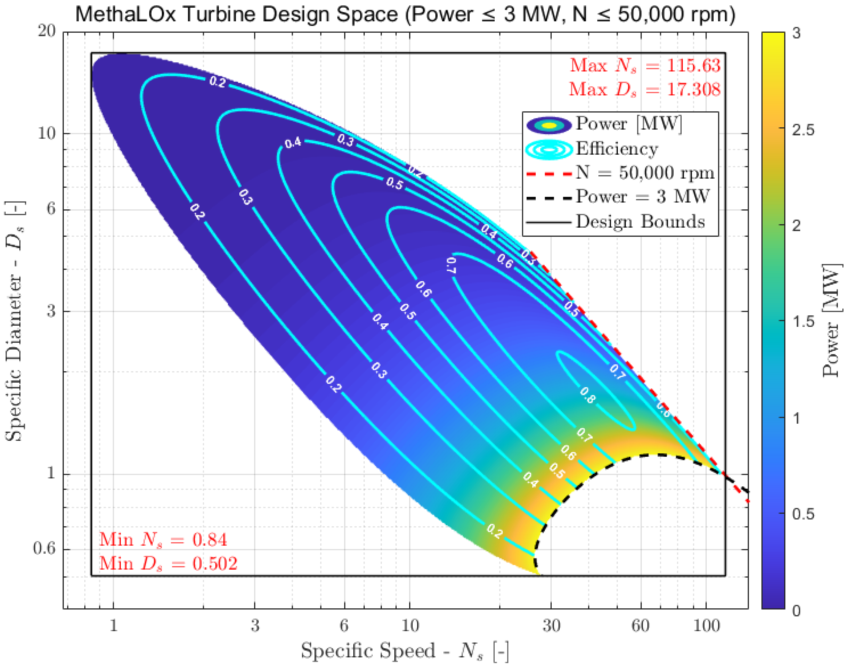

Figure 3.9: MethaLOx - Ns-Ds design space (trimmed)

It is also possible to assess how this design space translates into mass flow rate boundaries. This can be done by plotting the results of Equation 3.29 and Equation 3.33 against D_s:

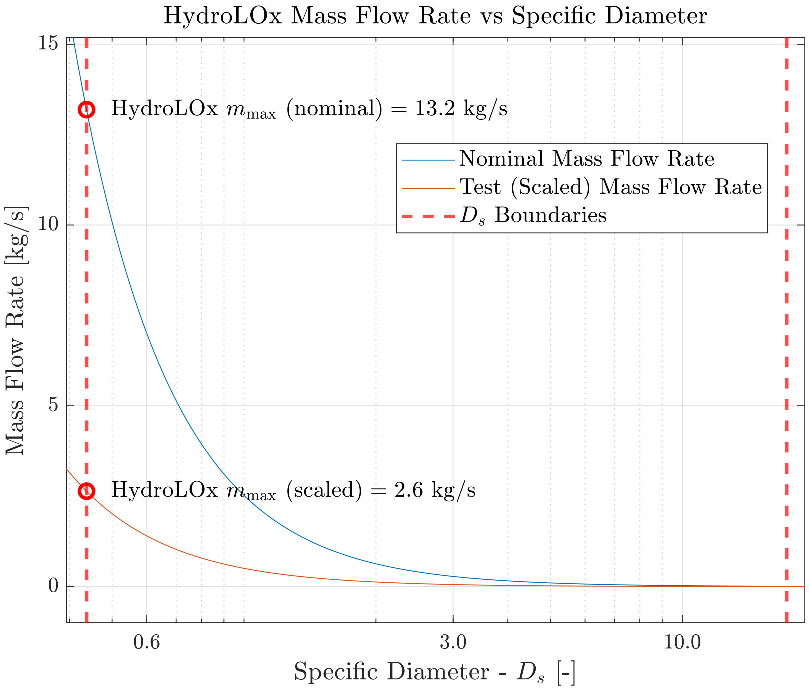

Figure 3.10: HydroLOx Mass Flow Rate over the D_s domain

For these conditions, the maximum nominal mass flow rate of a gas generator to be tested in the facility would be $13.2\ kg/s$, which would be scaled down to $2.6\ kg/s$ in order for it to be tested at a power level of $3\ MW$.

It is once again to be noted that this plot shows the operating region of the mass flow rate for the most extreme conditions. Any deviations from these conditions (ex, a lower inlet temperature or pressure ratio) will result in a larger operating window, allowing for a larger design space in terms of D_s, thus higher mass flow rates. For MethaLOx, the results are the following:

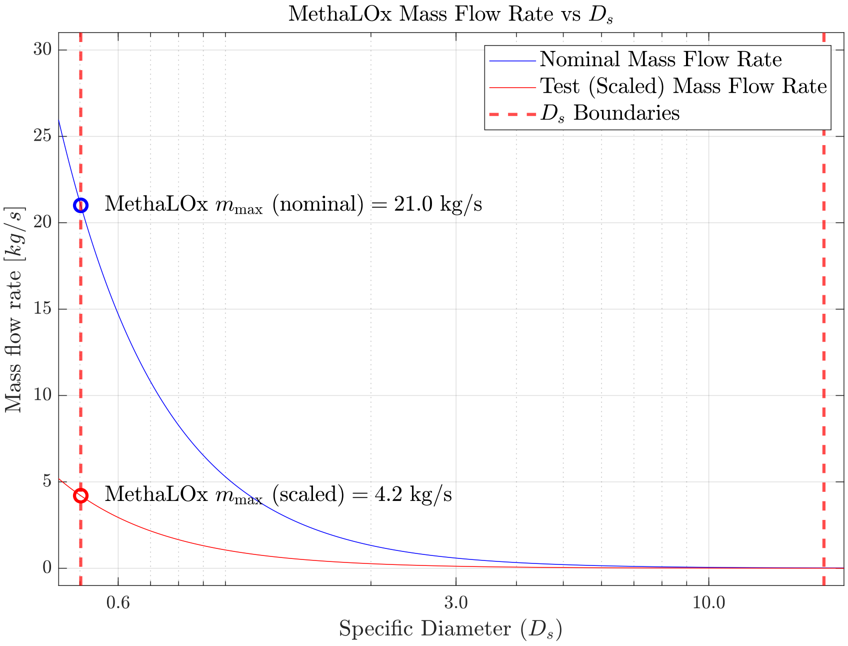

Figure 3.11: MethaLOx Mass Flow Rate over the D_s domain

The values are generally higher at $21.0\ kg/s$ in full-scale conditions tested at $4.2\ kg/s$, due to the higher density of MethaLOx combustion gases.

In addition, it was identified that it was useful to include an estimate of the engine thrust for which the turbines could be tested. This is particularly important for assessing the test bench flexibility for future engine developments, where the thrust level may be increased. The methodology for this estimation was based on the following equation:

$$F_T = \dot{m} I_{sp} g_0 \tag{3.36}$$

Given that the main driving factor for the specific impulse is the combination of propellant, a common value for specific impulse for each combination of propellants was taken from the literature. For hydrolox, an average between Vulcain 1 and Vulcain 2 provides a specific impulse of $430\ s$. For Methalox, the value of $350\ s$ from the Raptor engine was taken. Since this is a ROM analysis, this rough estimate of the I_{sp} values is sufficient to provide an overall figure for the engine thrust. It should, however, be noted that there may be a significant error margin in these results.

Estimating the mass flow rate is more challenging. Given that the turbine mass flow rate can be computed from the turbine diameter, pressure ratio, and gas parameters, it was decided to estimate the engine mass flow rate based on the turbine mass flow rate. This estimation has a different methodology for each cycle, given the significantly different operating conditions.

For gas generators, given the absence of any suitable method to estimate it, it is based on the sample. The values can be seen in the following table:

Table 3.4: Gas-generator turbines mass flow data

Engine	Turbine	$\dot{m}_{engine}$	$\dot{m}_{turbine}$	m_t/m_e (%)
Vulcain	Fuel Oxidizer	235	5.40 1.46[1]	2.30 0.61
Vulcain 2	Fuel Oxidizer	270	6.00 2.15[1]	2.22 0.80

Despite the small sample, this table provides fundamental information. First, the fuel turbine requires a significantly higher mass flow rate than the oxygen turbine, which, together with other parameters already displayed in the complete table for the sample, indicates that the fuel turbine generally operates at much higher conditions.

Additionally, it allows selecting a specific value for the fraction of the mass flow rate that passes through the turbine. Given the limited size of the sample, a value of 2.5% was chosen to include a margin above the maximum value obtained. This was done to underestimate the engine's mass flow, providing a more conservative and general thrust prediction. Having more specific data, this analysis can be improved to mitigate the error.

Given that the only turbine parameter from which this thrust estimation is dependent is the mass flow rate, which only depends on D_s and the gas parameters, the thrust can also be plotted as a function of D_s. The results can be visualized in the following plot:

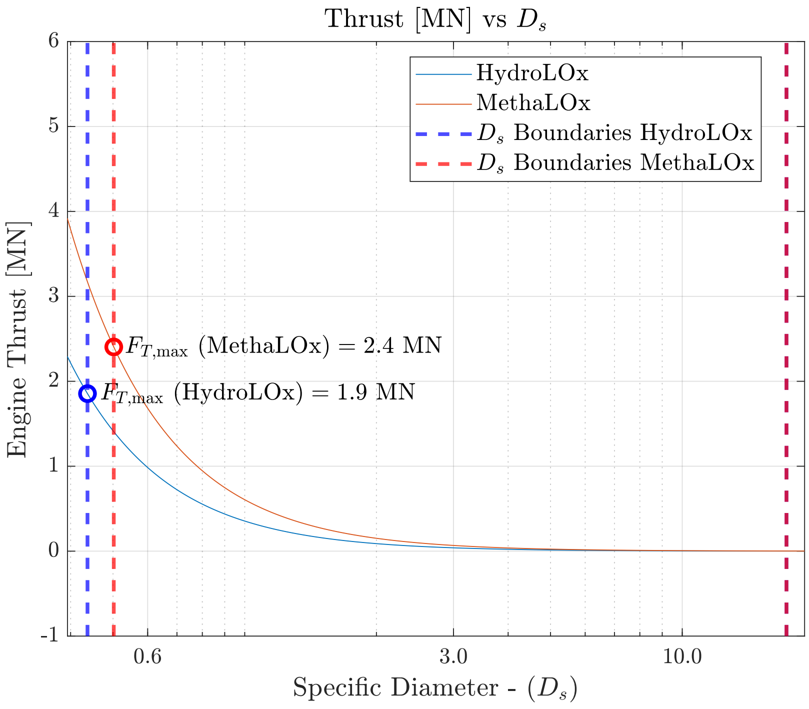

Figure 3.12: Thrust [MN] vs D_s

This plot can be interpreted as indicating that the test facility can test turbines for gas generator cycle engines with a maximum thrust of $1.9\ MN$ for HydroLOx engines and $2.4\ MN$ for MethaLOx engines under the specified conditions. The point of maximum thrust occurs for the minimum value of D_s, and the larger D_s, the lower the maximum engine thrust. This condition is verified since, given the fixed parameters, the mass flow rate scales inversely with the D_s, as can be observed in Figure 3.10 for HydroLOx and in Figure 3.11 for MethaLOx, with both gas mixtures displaying similar behaviour.

3.3.2. Staged Combustion

As mentioned in subsection 3.2.4, to perform scaling of Staged Combustion engines, it is not feasible to bring down the outlet static pressure to $1\ atm$, as it would imply a reduction of the density and mass flow rates on a factor of more than 100, loosing representiveness in the flowfield, represented by the decrease in the order of magnitude of the Reynolds number:

$$Re_D = \frac{\rho\, UD}{\nu} \tag{3.37}$$

---

[1] Predicted value assuming the same efficiency value as the one reported for the engine's fuel turbine.

Therefore, the following assumptions are made:

- $p_{t,in-nom} \leq 250\ bar$ - obtained from the sample and adding a 20% margin on top
- $\Pi_{ts} \leq 2.0$ - also obtained from the sample with a 20% margin
- SF_{max} - Maximum scaling factor applied on the inlet and outlet pressures depends on the test objectives. As mentioned, the reduction of the Reynolds number (Equation 3.37) with the scaling (due to the decrease in the density) leads to an inherent loss of representativeness. The test objectives shall define the acceptable reduction and will not be an object of this research. So, the design spaces will be plotted for an example scaling factor and combined with considerations that generalize the results.
- $T_{t,in} \leq 1000\ K$ - for the same reason as the in gas-generator case, in the thermomechanical limit of the materials.

With the current assumptions, the following values for the adiabatic enthalpy drop were obtained:

Table 3.5: Values for the adiabatic enthalpy drop for the studied propellant combinations (SC)

Propellant combination	Δh_s [MJ/kg]
HydroLOx	0.90
MethaLOx	0.46

These values are substantially lower than the ones observed for the gas generator cycle, due to the much lower pressure ratio.

With these values, it is possible to plot a similar design space to that for gas-generator engines for the two propellant combinations. A safety factor of 10 was chosen for this plot for illustration purposes.

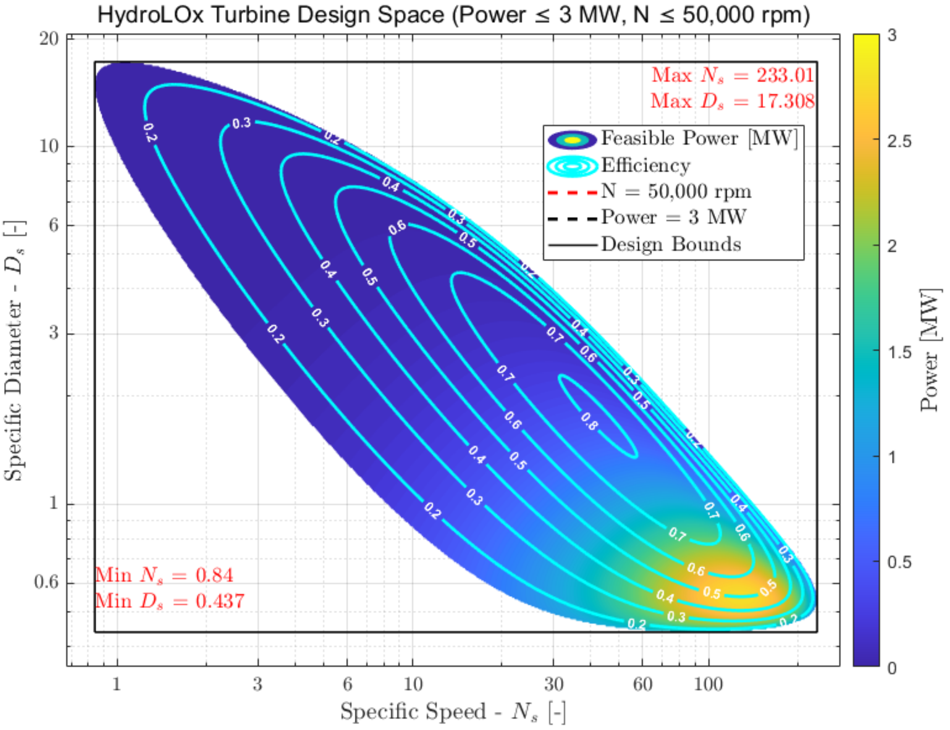

Figure 3.13: HydroLOx design space for a staged combustion cycle with a scaling factor of 10

Due to the reduced volumetric flow rate limitations and the reduced mass flow rate of HydroLOx combustion gases associated with their low density, the plot has no forbidden region for this scaling factor.

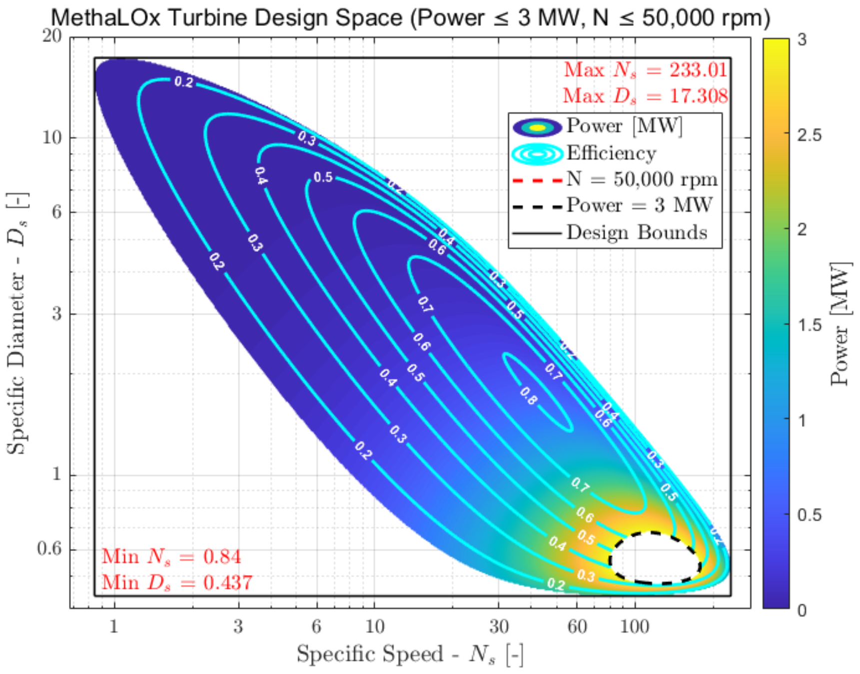

Figure 3.14: MethaLOx design space for a staged combustion cycle with a scaling factor of 10

For the methane, due to the higher density, there is a forbidden region. These plots represent the Ns-Ds design space boundaries for staged combustion turbines. However, this forbidden region can be eliminated by further increasing the scaling factor.

In regions where the power is below $3\ MW$, there is room to reduce the scaling factor if the test specification benefits from closer Reynolds-number matching. Similar to the plot for gas-generator turbines, this plot is for the extreme case, where all properties are at their maximum values. Similarly to the gas-generator case, any reduction in these operating parameters will allow for a larger operating range of the facility by decreasing Δh_s.

It is also possible to plot the nominal and scaled mass flow rates as a function of D_s. Since it was found that for such a scaling factor, the boundaries of the (N_s, D_s) range are maximum, and equal for both propellant combinations, the mass flow rates can be combined into a single plot:

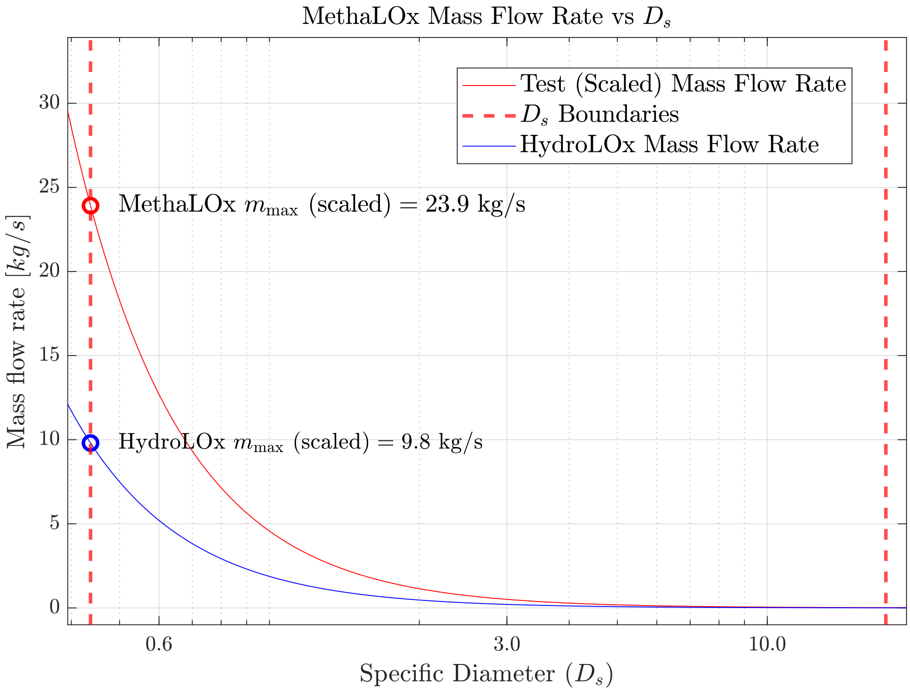

Figure 3.15: Mass flow rate capabilities for both propellant combinations

These results shall be interpreted primarily from a scaling factor perspective. The facility is capable of operating turbines up to $98\ kg/s$ of HydroLOx combustion gases and $239\ kg/s$ of MethaLOx combustion gases. These values are then scaled by the scaling factor, resulting in the values presented in the plot for an SF of 10. The significant difference in the mass flow rate capabilities among the propellants is due to the difference in density. This is because the limiting parameter is the volumetric flow rate rather than the mass flow rate, and attributed to the substantially higher density of the MethaLOx combustion gases.

Finally, the engine thrust corresponding to the determined operating window can also be computed. For staged-combustion-cycle engines, estimation is performed more precisely, leveraging the cycle characteristics. First, recall that there are three types of staged combustion engines: fuel-rich, oxidizer-rich, and full-flow staged combustion. The difference among these different cycles is which propellant mixture is driving the turbine(s).

In a fuel-rich staged combustion, the full mass flow of fuel to be injected in the engine is injected upstream in the preburner, with a small fraction of the oxidizer, producing a fuel-rich stream (the oxidizer is fully combusted, while a fraction of the fuel remains unburnt). The O/F ratio (i.e., the required oxidizer mass flow) to be injected into the preburner depends on the target temperature. Following the same process as before, where the most ”extreme-case scenario” is always applied, in this case, the O/F ratio for which a preburner chamber temperature of $1000\ K$ is determined.

For oxidizer-rich staged combustion, the logic is similar. The only difference is that, contrary to fuel-rich conditions, the preburner operates in oxidizer-rich conditions in this case. The full oxidizer mass flow to be injected into the engine is also injected into the preburner, along with a small fraction of the fuel. This produces an oxidizer-rich stream at the outlet of the gas generator, which will drive the turbine. Once again, the O/F ratio for which the preburner operates at $1000\ K$ is computed.

Finally, full-flow staged combustion combines the two previous cases. There are two turbines, each driving a single pump. One turbine operates in fuel-rich conditions, while the other operates in oxidizer-rich conditions. In this case, the fuel and oxidizer streams are split upstream of the preburner using a control-valve mechanism to achieve the desired mass flow rates of each propellant to be injected into each preburner.

It is usually not a design choice to opt for fuel-rich or oxidizer-rich staged combustion, but rather a propellant combination constraint. For example, for hydrogen, by plotting the adiabatic flame temperature for different values of O/F, it is noticeable why fuel-rich is the usual choice (Figure 3.17)

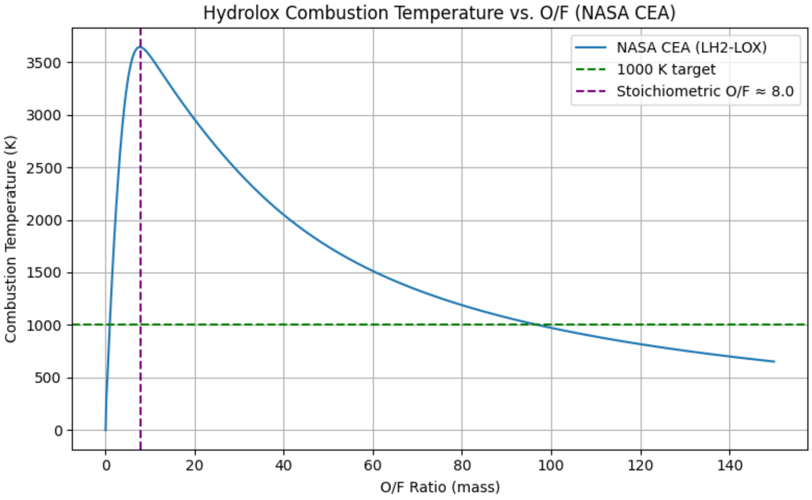

Figure 3.16: O/F ratio vs Adiabatic Flame Temperature - HydroLOx combustion (large O/F range)

The boundaries of this plot were purposely exaggerated to show that, despite having two numerical solutions - one close to 1, and the other close to 100 - it is impractical to operate in an O/F ratio of 100. It would require unattainable precision in the control mechanisms for fuel flow, and it would run into other issues with flow and mixing inside the combustion chamber, making this solution unfeasible. Therefore, it can be clearly stated that, for HydroLOx combustion, any staged-combustion engine design should be fuel-rich. By adjusting the boundaries of the plot to a more reasonable interval of mixture ratio values, the intersection with the $1000\ K$ (material limits without cooling) can be more easily observed:

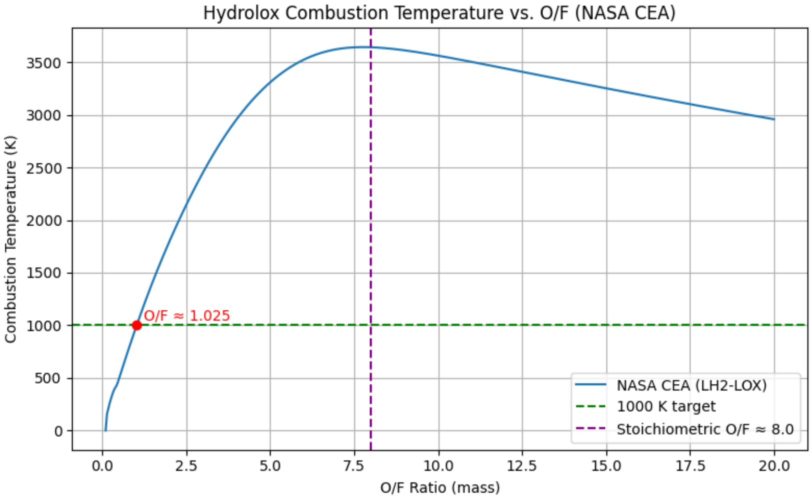

Figure 3.17: O/F ratio vs Adiabatic Flame Temperature - HydroLOx combustion

The plot now shows that to achieve a chamber temperature of $1000\ K$ in the preburner, a mixture ratio of 1.025 shall be injected. The results on excess fuel after combustion, given that the O/F ratio is much lower than the stoichiometric one (close to 8). Therefore, the resulting stream, which will drive the turbine, is highly fuel-rich.

By plotting the same results for methane, the O/F ratios required to achieve $1000\ K$ of preburner chamber temperature can also be determined:

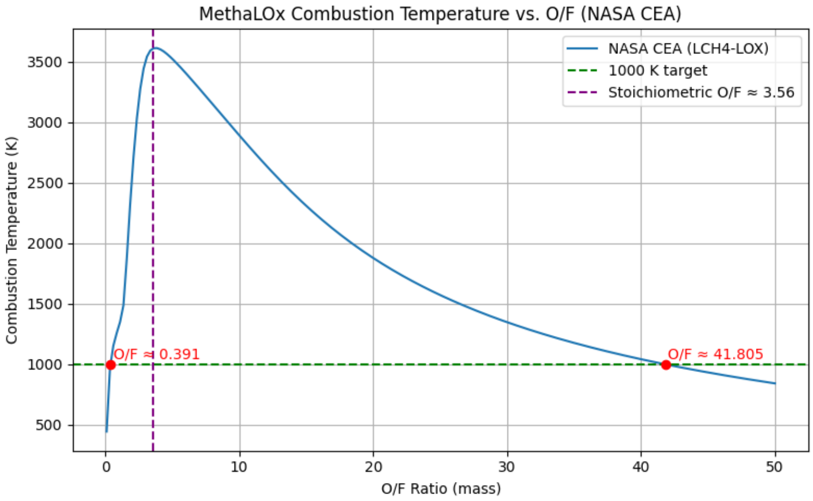

Figure 3.18: O/F ratio vs Adiabatic Flame Temperature - MethaLOx combustion

In this case, there are two values of O/F within reasonable boundaries that return a combustion temperature of $1000\ K$ - 0.391 and 41.805. Despite this last value still being relatively high and adding complexity to the operation, it is far more manageable than the value close to 100 observed in the hydrolox case. This highlights the better suitability of a MethaLOx propellant combination for a full-flow staged combustion, where both a fuel-rich and an oxidizer-rich combustion at high temperatures is required, since each gas generator feeds its own turbine.

The following table sums up the findings regarding the required O/F ratios to achieve the target temperature for both propellant combinations:

Table 3.6: O/F ratios for each type of Staged Combustion for which $T_{c,preburner} \approx 1000$ K

Propellant Mixture	O/F for Fuel-Rich SC	O/F for Oxidizer-Rich SC
HydroLox	1.025	≈ 100 (unfeasible)
MethaLox	0.391	41.085

Using these values, equations can be derived for both fuel-rich and oxidizer-rich turbine mass flow rates, based on the engine mass flow rates. For fuel-rich:

$$m_{turb,FR-SC} = m_{f,e}(1 + O/F_{pb}) \tag{3.38}$$

Where $m_{turb,FR-SC}$ represents the full mass flow rate going through the turbine, $m_{f,e}$ the engine overall fuel mass flow rate, and O/F_{pb} represents the preburner operating oxidizer to fuel ratio, taken from Table 3.6.

For oxidizer-rich staged combustion, the solution is similar, but with the oxidizer mass flow rate acting as the driving parameter:

$$m_{turb,OR-SC} = m_{o,e}\left(1 + \frac{1}{O/F_{pb}}\right) \tag{3.39}$$

Where $m_{turb,OR-SC}$ once again represents the full mass flow rate going through the turbine, $m_{o,e}$ the engine overall oxidizer mass flow rate.

These equations can be rewritten to yield explicit expressions for the engine mass flow rates in terms of the turbine mass flow rate (which is determined by Ns-Ds and the propellant combination density).

For fuel-rich, Equation 3.38 becomes:

$$m_e = m_{f,e}\left(1 + O/F_e\right) = \frac{m_{turb,FR-SC}}{1 + O/F_{pb-FR}}\left(1 + O/F_e\right) \tag{3.40}$$

For oxidizer rich, similarly Equation 3.39 becomes:

$$m_e = m_{o,e}\left(1 + \frac{1}{O/F_e}\right) = \frac{m_{turb,OR-SC}}{1 + O/F_{pb-OR}}\left(1 + \frac{1}{O/F_e}\right) \tag{3.41}$$

In these equations, the engine oxidizer-to-fuel ratio (O/F_e) is introduced. For this, the average of the common values from existing engines will be used for thrust estimation.

Having derived the estimation for the mass flow rate of the engine from the mass flow rate of the turbine, Equation 3.36 can now be used to estimate the operating domain of the test bench in terms of engine thrust.

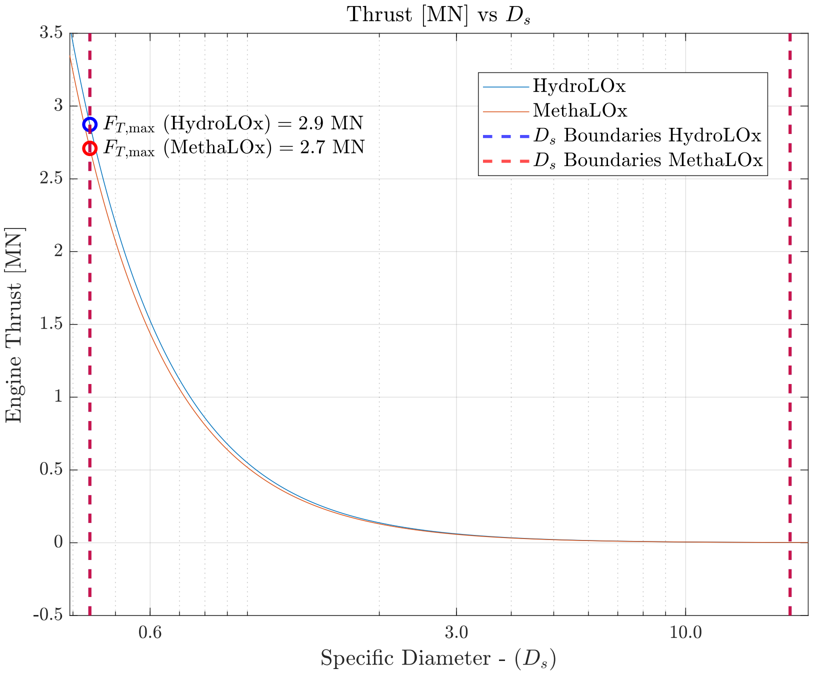

Figure 3.19: Facility's capabilities translated into engine thrust for both propellant combinations, for a scaling factor of 10

For staged combustion cycle engines, the thrust-translated capabilities of the facility are generally higher than for gas generator cycles. These findings reflect the higher scaling capabilities when compared to the gas generator cycle (in this case, the scaling factor is twice as large, allowing for testing turbines with higher mass flow rates, corresponding to engines with higher thrust levels). Further increasing the scaling factor may yield even higher thrust levels.

3.4. Operational Requirements

As a product of this scaling methodology and application to the sample, a set of operational requirements can be derived. Starting with the requirements whose values are known at this level:

- **OR1** - The test facility shall support testing at pressure ratios up to 20
- **OR2** - The test facility shall support temperatures of up to $1000\ K$ at the turbine inlet
- **OR3** - The test facility shall support gas generators, allowing for hot gas testing

  - **OR3.1** - The gas generator support infrastructure shall be compatible with both HydroLOx and MethaLOx propellant combinations
- **OR4** - The test facility shall contain a driving media storage system rated to no less than 20 bar
  - **OR4.1** - The test facility shall contain a liquid hydrogen tank rated for no less than 20 bar.
  - **OR4.2** - The test facility shall contain a liquid oxygen tank rated for no less than 20 bar.
  - **OR4.3** - The test facility shall contain a liquid methane tank rated for no less than 20 bar.
  - **OR4.4** - The test facility shall contain a gaseous nitrogen tank rated for no less than 20 bar.
- **OR5** - The test facility shall contain a regulating system capable of supplying a target pressure to the test specimen or to the enthalpy generation device.
- **OR6** - The test facility shall support testing up to rotational speeds of $50000\ rpm$
- **OR7** - The test facility shall have the capability to dissipate no less than 3 MW of shaft power

These are the main operational requirements that result from the test objectives and the scaling exercise. Further operational requirements are needed to fully characterize the facility. However, due to the uncertainty level at this stage, the values are still to be determined (TBD). In the cases for which values are needed for the subsequent chapters of this research, anchored assumptions will be made for those parameters. A list of the TBD operating requirements follows:

- **OR8** - The test facility shall be able to operate for TBD consecutive seconds at the maximum mass flow rate
- **OR9** - The test facility shall be able to operate TBD consecutive transient modes (startup and shutdown)
- **OR10** - The test facility shall have a startup time (from static to nominal rotational speed levels) of TBD seconds.
- **OR11** - The test facility shall have the capability of thermally conditioning the turbine test article
- **OR12** - The test facility shall comply with safety standards according to the local health and safety law
- **OR13** - The test facility shall comply with local environmental regulations
- **OR14** - The test facility shall have the capability of being fully assembled and disassembled in a maximum of TBD days
- **OR15** - The test facility shall be able to adapt to support test specimens with different geometrical parameters by switching no more than TBD components

4

General Layout and Feed System

Having defined the requirements for the test facility, it is now possible to proceed with the system's design. This chapter begins by presenting the facility's general layout, based on the requirements. Subsequently, it proceeds to a selection among the options for each module.

4.1. General Layout

To achieve a facility capable of conducting tests in hot conditions at power levels up to $3\ MW$, a set of building blocks is required. The following subsystems need to be present: a propellant storage and feed system, a gas generator, a shaft supporting system (i.e, a "pillow block" containing the bearings and respective housings, and eventually dampers), a power dissipation mechanism, and an exhaust gas guiding and storage mechanism. The following diagram presents the top-level schematic of the facility containing the mentioned subsystems:

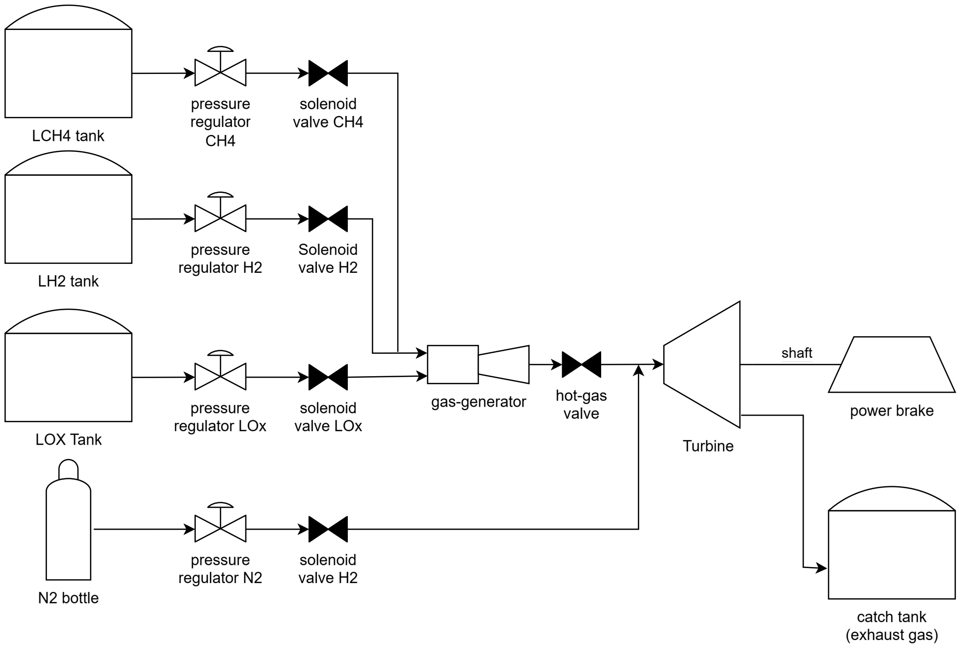

Figure 4.1: General system schematic overview

4.2. Focus of the design exercise

The previous section highlighted a potential issue for the System Design component of this master's thesis. Given that there are multiple subsystems to consider, it is not feasible to address all of them with the same level of detail due to time and resource constraints. Therefore, it was decided that the research would focus on the critical subsystems of the facility, which coincide with those that enable its flexibility.

First, the pillow block must ensure adequate rotordynamic support for the turbine; for that, detailed calculations are required to determine the mass distribution along the shaft, bearing placement, and cooling and lubrication requirements.

The other critical subsystem is the shaft-power-dissipation mechanism. Given the very high power levels the facility is required to support (up to $3\ MW$), an extensive overview of available alternatives, their compatibility with operational requirements, and a robust systems-engineering trade-off are needed.

For the remaining subsystems, a less detailed design exercise will be performed. The goal is to define viable solutions or present subsystem-specific requirements to serve as a foundation when selecting the specific components of the test facility. In practical terms, this means, for example, that no effort will be allocated to designing a particular valve for the feed system. Instead, the requirements the valve must meet will be presented, leaving future work to select an adequate valve that meets them.

During the literature review, it was observed that there are significant disparities in the information available for each subsystem. This leads to different levels of detail achievable with the same effort allocated. Therefore, the extent of the results may differ across subsystems. It will, however, be guaranteed that, for every subsystem, this design exercise provides a foundation with sufficient detail to fulfill the preliminary design role, leaving further details to be built on top of this work in a detailed or critical design phase.

The following sections highlight the available options for each subsystem, followed by a decision on the most suitable choice for each application.

4.3. Propellant storage and feed system

This subsystem shall consist of the interface between the existing and the gas generator. There are a few points to be taken into consideration for such a system:

- It is a requirement that the test facility shall be flexible in terms of propellants. This essentially means it should allow multiple propellant combinations to be burned in the gas generator, as well as cold flows of a single propellant.
- The feed system shall be able to operate within the range of pressure and temperature of the stored propellants, and also to support the mass flow rates and pressure gradients experienced during the operation. Every piping line and valve must comply with these requirements.
- The interface between the base structure (i.e., plant storage) shall be flexible to allow the test bench to be rapidly assembled and disassembled,

In terms of propellants, the recent developments of rocket engines and turbomachinery testing, together with the existing infrastructure at Lampoldshausen, allow for testing with the following propellant combinations:

- Cold Gaseous Nitrogen (GN_2) -, gaseous nitrogen testing provides a cheaper alternative compared to hot-gas testing for lower TRL and rotordynamics testing, for which the extreme temperatures and temperature gradients don't necessarily need to be replicated
- Hot testing with Liquid Oxygen (LOx) and Liquid Hydrogen (LH_2) - allows for driving media similarity to be attained for testing of turbomachinery for HydroLox . These propellants need to be burnt in a gas generator that has been previously tested to operate at the required chamber pressure.
- Hot testing with Liquid Oxygen (LOx) and Liquid Methane (LCH_4) - Similarly to HydroLOx engines, this propellant combination allows for a driving media similarity to test turbomachinery for MethaLOx engines. It requires a different gas generator, designed to operate with these propellants for the desired chamber pressure.

The pressures to be fed into the gas generators are dependent on the head and pressure losses of the components of the feed systems, following the rules:

$$p_{t,in} = p_{c,GG} + \Delta p_{GG \rightarrow Turbine} \tag{4.1}$$

Where $p_{c,gg}$ is the chamber pressure at which the gas generator is operating and $\Delta p_{GG \rightarrow Turbine}$ is the sum of the pressure losses from the outlet of the gas generator to the turbine inlet.

Following the same logic, the pressure downstream of each propellant tank is given by:

$$p_{out,tank} = p_{c.GG} + \Delta p_{feed} + \Delta p_{inj} \tag{4.2}$$

Where Δp_{feed} corresponds to the total pressure losses along the feed line, from the pressure regulator to the gas generator inlet, and Δp_{inj} represents the pressure losses over the injector of the gas generator.

Given that the tank pressures are usually much higher than those fed to the gas generator, an adjustable pressure regulator set to $p_{out,tank}$ needs to be placed downstream of each tank. This also enhances safety, minimizing the section of the test facility operating at extreme pressures.

The feed system also includes multiple components to pressurize the propellant tank with an inert gas, usually stored in a bottle. This system consists of an inert gas bottle, a pressure regulator that sets the pressurization line to the desired tank pressure, and the pressurization valve, which, when opened, allows inert gas to enter the propellant tank, pressurizing it.

In addition, two valves are integrated into the propellant tank for safety reasons. First, a safety relief valve that opens and vents the propellant from the tank if it reaches the defined trigger pressure. As a redundant mechanism, a rupture disk, which bursts and opens the tank to the atmosphere at a pressure slightly higher than the safety relief valve trigger pressure, is also added. The detailed P&ID diagram of the feed system can be visualized in the following figure:

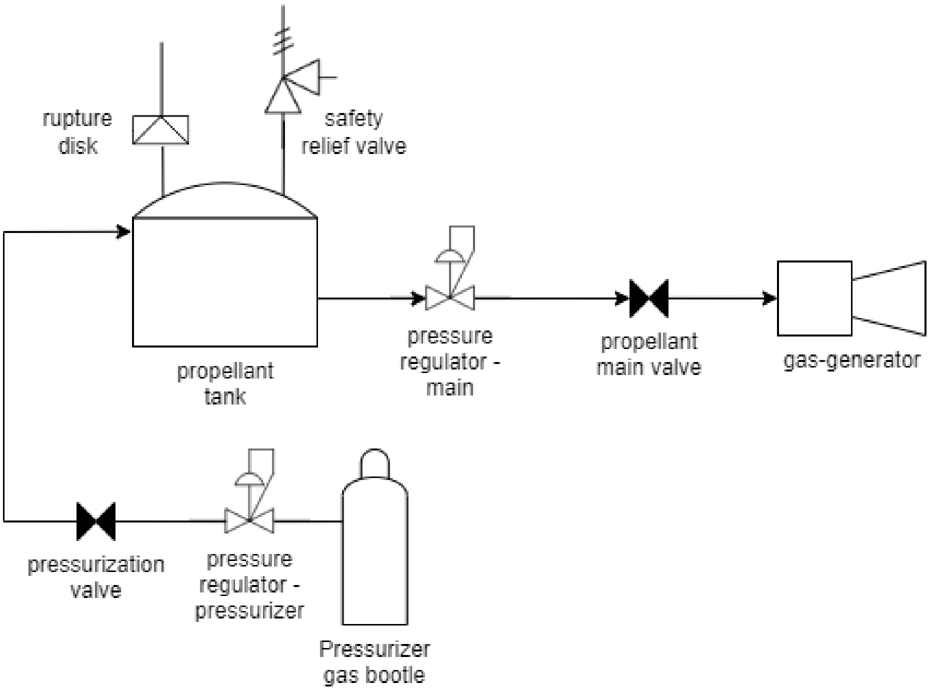

Figure 4.2: Gas-Generator Feeding Line P&ID Diagram

4.4. Gas Generator

As previously mentioned, the facility shall be prepared for three types of testing: cold testing with gaseous nitrogen and hot testing with both hydrolox and methalox propellant combinations. For these last two, a gas generator is required to heat the mixture in its combustion chamber and supply the hot gas to drive the turbine. Additionally, the interface between the gas generator and the test facility shall be flexible, allowing rapid switching between gas generators without requiring significant modifications to the interfaces.

4.4.1. MethaLOx gas generator

For a combination of methane and liquid oxygen as propellants, a straightforward option is available: ArianeGroup (former Airbus Defence and Space business division Propulsion & Equipment) has developed and fully characterized, in 2013, a gas generator over an operating range from 20 to 70 bar, by varying the O/F ratio. The test campaign that led to this characterization was performed in the P8 test cell at DLR - Lampoldshausen [39].

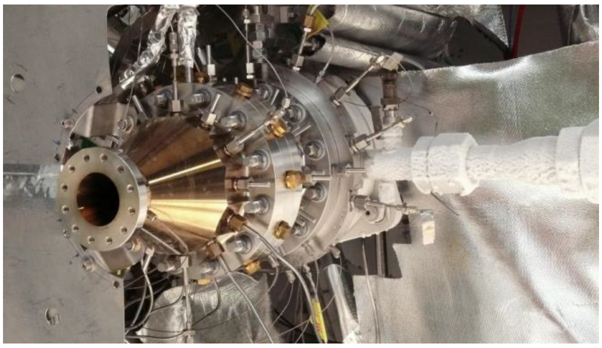

Figure 4.3: Gas Generator test setup at DLR Lampoldshausen P8 [39]

This once again demonstrates the capabilities of the mother infrastructure at P8, which is key to the development of this turbine test facility. This not only qualifies the gas generator for the required application but also the existing feed system and mother infrastructure, which have already reproduced the operating point needed for the turbine test campaign.

The characterization was performed for a wide operating interval, going from 20 to 70 bar of chamber pressure (Figure 4.4a). This is particularly useful for testing turbines for staged combustion engines, given that, as previously mentioned, there are some cases where it is advantageous to test at a higher pressure, provided the power level remains below the defined threshold.

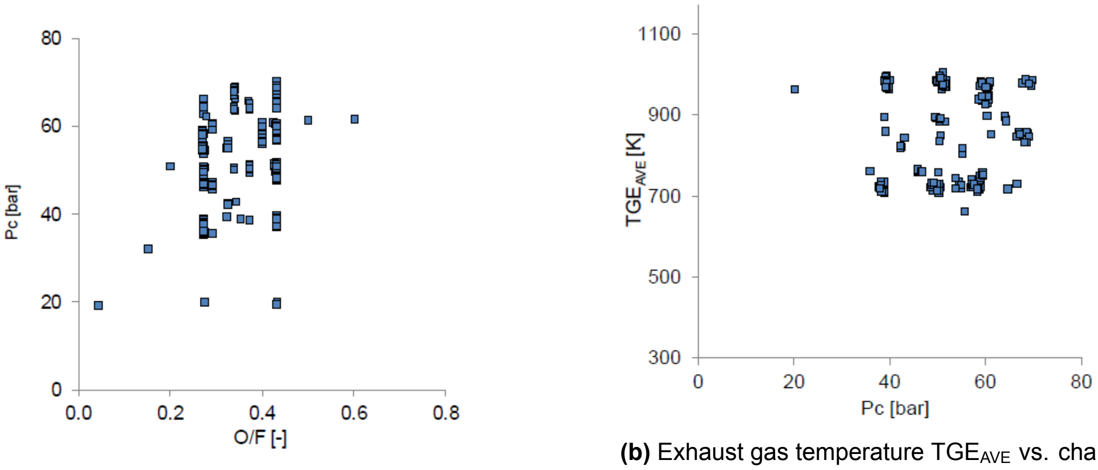

(a) Chamber pressure Pc vs. mixture ratio O/F

(b) Exhaust gas temperature TGE$_{AVE}$ vs. chamber pressure Pc

Figure 4.4: Operating envelope of gas generator tests [39]

Finally, the test campaign demonstrated the ability to vary the outlet temperature of the gas generator (to be fed into the turbine) at constant pressure by changing the O/F ratio (Figure 4.4b).

Since this activity was performed by ArianeGroup, it is considered accessible in-house technology. This makes this gas generator clearly the most accessible and flexible option, which, together with the lack of other promising candidates, makes the design decision quite simple. Therefore, it has been chosen for this test facility application without any trade-offs.

4.4.2. HydroLOx gas generator

To perform hot testing of turbines integrating engines propelled by a combination of liquid hydrogen and liquid oxygen, it is necessary to incorporate a gas generator that has been characterized for the required chamber pressure and O/F ratio.

In chapter 3, it was observed that having a reduced pressure at the inlet and outlet of the turbine, while preserving the pressure ratio, is the solution to achieve high-similarity tests at reduced power. Considering the initial (flexible) assumption that the expansion is performed to ambient (i.e. $p_{s,out} \approx 1\,bar$), together with the observed pressure ratios, this would mean a gas generator that is characterized for a chamber pressure in the order of $20\,bar$ is required.

Unfortunately, no gas generator meets these conditions and is usable by ArianeGroup. There are multiple options to tackle this issue, to be decided after careful consideration in a detailed design:

- Perform the hot testing for HydroLOx turbines with methane and oxygen. Given that there is a MethaLOx gas generator characterized from 20 to 70 bar, this presents a solution. However, given the substantially different gas properties (Table 3.2), there will be a loss of representativeness, particularly in the pressure ratio and flow properties, as different gas parameters yield different expansions. However, it can still be helpful to test for lower TRL levels (for which the representativeness level requirements are lower) in an initial stage, until a HydroLOx gas generator is available.
- Develop a new HydroLOx gas generator - developing a gas generator for this specific application with a large characterized operating interval is also a solution for this issue. It does, however, entail significant delays in development time and cost, as a new component must be developed from scratch.
- Adapt and perform a characterization test campaign to increase the operating envelope of an existing HydroLOx gas generator - this can be done using, for example, Vulcain 2.1 gas generator. It is already qualified for flight over at the nominal operation interval. However, the lower end of the chamber pressure operating interval is most likely still too high for the current application. This can be reduced by adapting the design of the injector's elements, followed by a characterization test campaign. This option is promising because it can provide results similar to the previous option for a fraction of the cost and development time.

A decision shall be made after a compliance check with the available time and budget for this test facility. As mentioned, a combination of these solutions, where one is initially used and later replaced by a more representative option as it develops, can be the most suitable approach.

5

Power Dissipation Mechanism

As a strict requirement for the facility, it must be able to test turbines at a power level up to $3\ MW$. Despite this already being a significant reduction compared to the power levels during nominal turbine operation in rocket engines, it is still a considerable amount of power that needs to be dissipated. Doing so can be quite challenging and requires systems that are very costly and complex to operate, thereby presenting a significant challenge when designing a turbine test facility.

An overview of the identified options can be observed in the chart below:

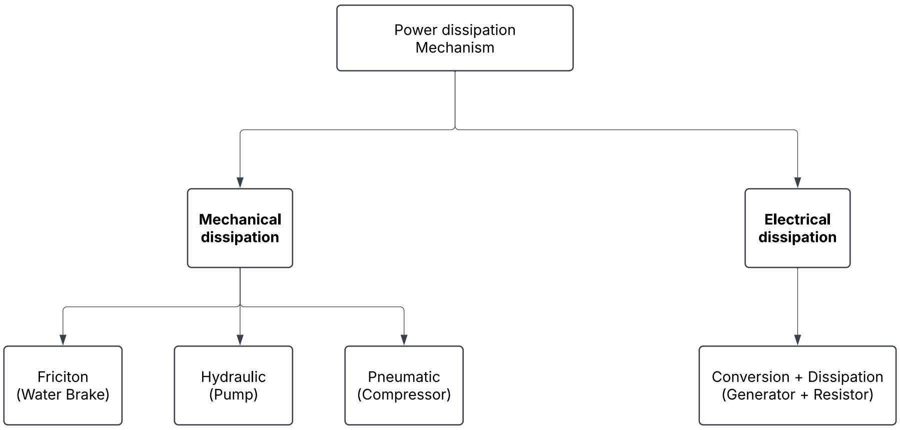

Figure 5.1: Power Dissipation Options

There are essentially two ways of dissipating the power of a rotating shaft at a level of $3\ MW$: either through mechanical disposal, for which there are several suitable methods, or by electric conversion and disposal. For the power level of this application, only one method of electric power dissipation was found to be appropriate.

Such devices shall also provide an accurate measurement of the shaft's power and torque. The methodology for such measurements is usually by measuring the outlet media of these devices, which, combined with their efficiency characterization curves, allows for computing the power and torque supplied by the turbine.

For the design of this subsystem, an extensive overview of the options for dissipating this power will be provided, followed by a system engineering trade-off to define the most suitable candidate, which will be integrated into the test facility.

5.1. Hydraulic Dynamometer (Water Brake)

There are multiple types of hydraulic engine dynamometers. As introduced in the state of the art, the most widely used in turbomachinery test facilities is the water brake.

The reason for this is the high power and torque ratings of such equipment, and the relatively simple design scalability, allowing for wide ranges of operating conditions.

A water brake is a power-dissipation mechanism that uses water circulating around the shaft to dissipate energy while measuring torque. It does so by injecting water into a disk with toroidal pockets. The water is heated by friction as it collides with the brake housing, removing energy from the disk. This disk is coupled to the shaft, and the water's mass flow (controlled by the feeding line, upstream of the brake) controls the energy dissipated from the system, actively controlling and measuring the disk's power. The system is designed to be inherently inefficient at increasing water pressure, thus very efficient at dissipating energy while keeping pressure low. This allows for the dissipation of large amounts of power from the shaft without significantly increasing the water temperature. As these instruments are well characterized, the power can be accurately measured by monitoring the temperature of the outlet water stream.

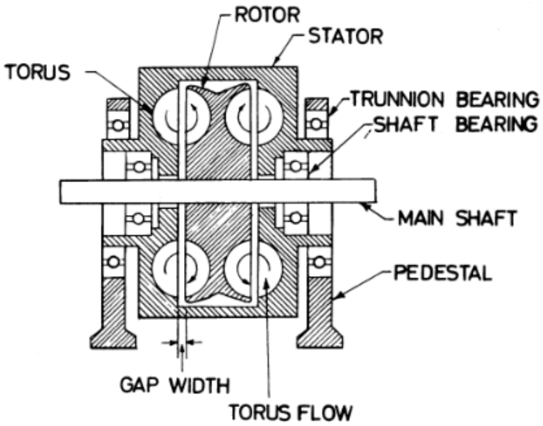

Figure 5.2: Schematic diagram of hydraulic dynamometer [40]

It requires a constant flow of cold water at the inlet and produces a flow of hot water at the outlet. The energy absorbed by the water brake is given by Equation 5.1, through an energy balance:

$$P_{diss} = \dot{m}_{water} c_{p\ water} (T_{out} - T_{in}) \tag{5.1}$$

As T_{in} is defined by the storage temperature of the facility, $\dot{m}$ is regulated to obtain an outlet flow at a temperature that can be disposed of or stored in a catch tank. Additionally, this outlet temperature is limited to about $50 - 70°C$ to prevent cavitation [40].

As this is one of the most widely used power-dissipation mechanisms for turbine testing applications, there is a wide range of COTS options available. However, for such high-speed applications as $50000\ rpm$, this system usually needs to be paired with a gearbox upstream to reduce the rotational speed and convert it into torque. This is advantageous because these devices are typically rated for high torque rather than high speed.

To perform the trade-off, it is useful to have a figure for the required base infrastructure. In this case, the relevant parameter is the required water mass flow rate to achieve a specific temperature. For that, the following assumptions were made:

- $T_{in,w} = 25°C$
- $T_{out,w-max} = 50°C$
- $c_{p,water} = 4.18\ kJ/KgK$ - as the variation of the specific heat in this temperature range is minimal

Rearranging Equation 5.1 to be expressed as an explicit expression for the mass flow rate:

$$\dot{m}_{water} = \frac{P_{abs}}{c_{p\ water}(T_{out} - T_{in})} \tag{5.2}$$

Therefore, to dissipate $3\ MW$ of power, given the temperature constraints, the required mass flow rate of water is given by:

$$\dot{m}_{water} = \frac{3 \times 10^6}{4.18 \times 10^3 (50 - 25)} \approx 28.7\ kg/s \tag{5.3}$$

To compensate for variations in operating points, the mass flow rate is actively regulated upstream of the brake via flow-controlling mechanisms installed on the feeding lines.

It is also useful to plot the mass flow rate requirements for various values of the temperature rise within the brake - ΔT as a function of the output power, to assess the scalability of this power dissipation solution:

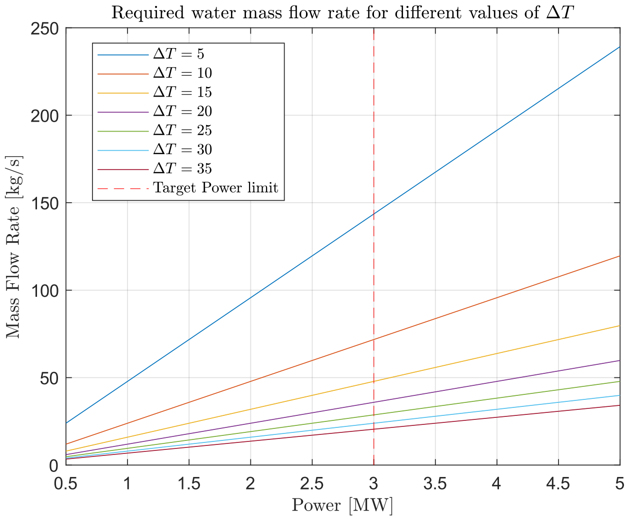

Figure 5.3: Required water mass flow rate for different values of ΔT

As could be derived from Equation 5.2, the mass flow rate requirements scale linearly with the power requirements. If the power were to be increased to $5\ MW$, a mass flow rate of water under $50\ kg/s$ would be enough to guarantee a water brake outlet temperature under $50°\ C$, under the mentioned assumptions.

It is also noticeable that for any temperature rise above $10\ °C$, the mass flow rate is already significantly below $100\ kg/s$. This highlights the water brake's ability to dissipate large amounts of power while keeping operating conditions within reasonable thresholds.

Regarding the geometrical considerations, the datasheet from a commercial water brake from Taylor Model H3606 [41] provides the following characteristics:

- Maximum power dissipation = $3.679\ kW$
- Maximum torque = $37993\ Nm$
- Maximum rotational speed =$2500\ rpm$
- Shipping weight = $5557\ kg$
- Dimensions: $1.600 \times 1.928 \times 1.867\ [m]$
- Moment of inertia (J) = $50\ kg \cdot m^2$

This datasheet highlights two significant concerns. The first is that, as expected, the rotational speed capabilities are significantly lower than those required by the test bench. This once again highlights the need to use a gearbox to reduce the rotational speed to a value the dynamometer can support. The second concern is the size of the machine, which is a relatively large system occupying a volume of over $5\ m^3$ and weighing over 5 tons, raising serious handling concerns during assembly and disassembly.

Finally, regarding scalability, these systems are usually limited by a maximum power dissipation (as shown in the example above). To increase the facility's power capabilities, an over-dimensioned water brake would need to be purchased and operated at an operating point below its maximum capabilities. However, the cost, size, and weight of such devices scale with the maximum power capabilities. Therefore, if this option is selected, a decision on the scalability capabilities against the increase in the overall cost of the system would need to be made.

5.1.1. Gearbox

As mentioned, this solution requires a gearbox because the input rotational speed is too high for the water brakes available on the market. This adds an axial interface, which contributes to the system's residual imbalance.

The nominal point is taken as the one for which a power of $3\ MW$ is obtained for $50000\ rpm$, corresponding to the following torque:

$$P = \tau\Omega \Leftrightarrow \tau = \frac{P}{\Omega} = \frac{3 \times 10^6}{50000\frac{2\pi}{60}} \approx 573\ Nm \tag{5.4}$$

The plot below shows how the torque-rpm conversion behaves in a gearbox:

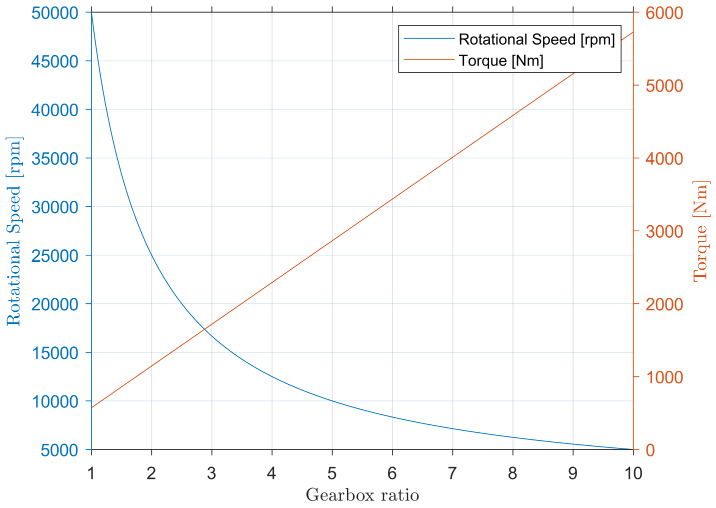

Figure 5.4: Torque-rpm behaviour for different gear ratios

The results for the most common gear ratios (1:2, 1:5, and 1:10) are highlighted in the table below:

Table 5.1: Torque and rotational speed values for the most common gear ratios

Gear ratio	Ω [rpm]	Torque - τ [Nm]
1:1 (No gearbox)	50000	573
1:2	25000	1146
1:5	10000	2865
1:10	5000	5730

This allows us to find a suitable gear ratio for which the input shaft conditions are compliant with the water brake curve, which is usually limited to rotational speeds approximately one order of magnitude lower than the nominal rotational speed of this application.

5.1.2. Startup

Regarding the startup process, there is an important figure to consider: the spin-up time (or startup time), t_{spin}. This parameter is usually limited by the test characteristics, so that the turbine reaches its nominal operating point (OP) within a time that still allows a sufficiently long test duration after the nominal point is reached. It is also considerably crucial from a rotordynamics point of view. If the turbine is operating in supercritical condition in its normal OP, the system must ensure that during startup, the critical frequencies are passed through quickly enough so that there is no risk of damage from resonance.

Given that the Rotordynamics analysis heavily depends on the chosen power dissipation mechanism, this preliminary analysis will focus primarily on the test duration.

Tests at this TRL, with the same test objectives as those the present facility aims to achieve, are usually in the order of 10 minutes. During this period, several operating points are conducted; therefore, the assumption that the startup procedure accounts for up to 10% of this time - i.e., 1 minute - is followed. Looking at Newton's second law for rotation, the parameters that have an impact on t_{spin} can be observed:

$$\tau = J\alpha = J\frac{\omega_f}{t_{spin}} \tag{5.5}$$

where J is the moment of inertia of the system, α the angular acceleration, which is determined as the target final rotational speed - w_f - divided by the spin-up time.

For illustrative purposes, in the case that no gearbox is used, τ is simply the turbine torque, and w_f it's nominal operational speed. Therefore, the spin-up time comes as:

$$t_{spin} = \frac{J\omega_f}{\tau_{turb}} \tag{5.6}$$

In reality, the turbine torque is not constant throughout startup and increases until it reaches its operational point. However, even if an optimistic approach of achieving the maximum turbine torque throughout the startup duration would lead to a spin-up time of 7.61 minutes, considering the brake's inertia of $50\ kg \cdot m^2$.

This value is well above the previously set limit, indicating that a startup auxiliary system is required. For options that would meet the required rpm, an electric motor could be used to spin up the shaft during startup. However, this is not the case, as a gearbox is needed, and the gearbox itself has a significant impact on spin-time through the concept of transmitted inertia [42]. Through the transmission and conversion of rotational speed into torque, the transmitted inertia as "seen by the turbine", for a transmission ratio of u, is given by:

$$J_{transmitted} = \frac{J_{brake}}{u^2} \tag{5.7}$$

This effect is also more intuitively visible using Newton's second law of motion for rotations on the brake side, now including the gearbox effect. Equation 5.5 becomes:

$$\tau_b = J_b\frac{\omega_{f,b}}{t_{spin}} \tag{5.8}$$

Where the subscript b refers to the brake side of the system. Adding the gearbox ratio - u - to express this equation as a function of the turbine parameters, it comes as:

$$\tau_t u = J_b\frac{\omega_f}{u \cdot t_{spin}} \tag{5.9}$$

Rearranging, an explicit expression for the spin-up time is attainable and comes as:

$$t_{spin} = \frac{J_b\omega_f}{\tau_t u^2} \tag{5.10}$$

In this equation, it is clear that the gearbox reduces the spin-up time by the square of the transmission ratio. Numerically, for a transmission ratio of 1:10, which is a likely ratio for the water brake application, and assuming no losses in the gearbox itself, it would lead to an improved spin-up time of 4.6 seconds. This value is well below the previously set maximum, indicating that a gearbox can solve the startup problem for this application. The effect of the gearbox ratio on the spin-up time is represented in the following figure:

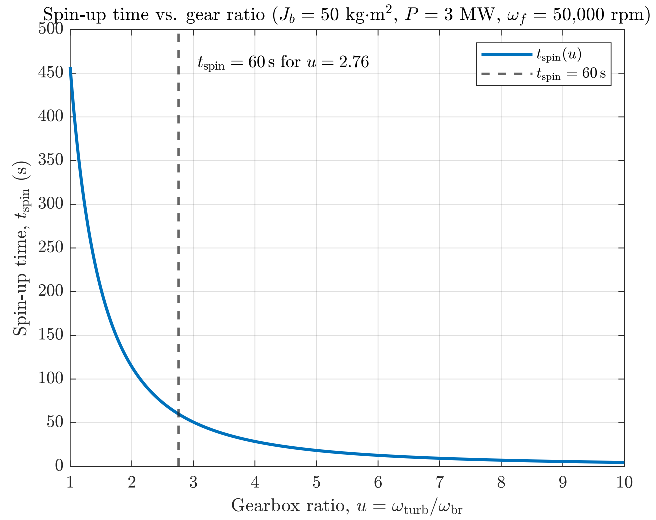

Figure 5.5: Gearbox effect in reducing the spin-up time

This clearly demonstrates the gearbox ratio's practical impact on reducing spin-up time, with a gearbox ratio of just 2.76 reducing it from 456 seconds (no gearbox) to 60 seconds.

The following plot shows, for the case of no gearbox, what the maximum inertia is that still enables the startup process to be under 1 minute. This is valuable input to determine whether a gearbox and/or an auxiliary electric motor are required for the other options.

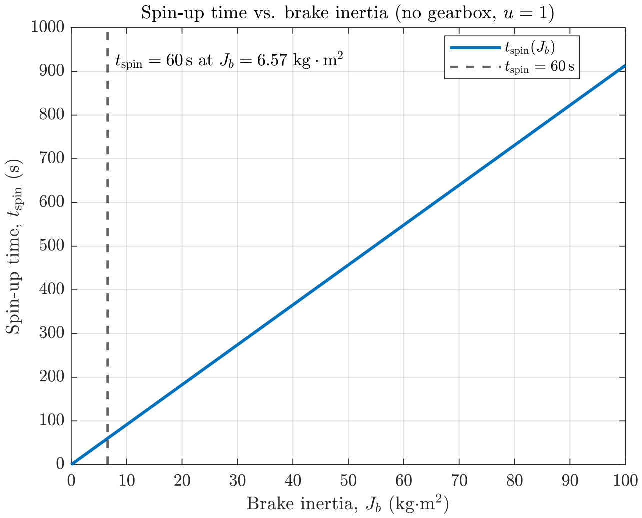

Figure 5.6: Spin-up time as a function of the brake inertia when no auxiliary startup system is used

The value of $6.57\ kg \cdot m^2$ is provided as a figure to be considered for the following options, as the absolute maximum inertia for which an auxiliary startup system may not be required. Please note that a reduction factor would still need to be applied to this value to account for the turbine's inertia, gearbox losses, and the torque overestimation in this analysis, which uses nominal operating parameters for the whole envelope.

5.1.3. Cost Estimation

There are multiple off-the-shelf power-brake solutions that, with a gearbox, are ready to meet the requirements of the current application with their default specifications (i.e., there is no need for a custom-made model). However, given that these devices are still considered highly specialized equipment, the supplier does not provide direct price quotes, as they depend on customer-specific requirements regarding lead time and additional mechanisms.

For this investigation, and to get a general idea of the order of magnitude of the price, it is possible to look at reports on contracts sealed with water brake suppliers for different power levels and estimate how the cost would be translated for a power level of $3\ MW$. Most of the cost quotes found referred to the fuel test bench, rather than the water brake itself. However, it was still possible to narrow down to two cost figures. First, Capax, a Croatian marine Engineering company, purchased in 2018 a package consisting of a fixed water brake with the capacity of $3.3\ MW$ ($4500\ hp$) and a portable water brake rated for $985\ kW$ ($1200\ hp$), for the value of 1,807,940 HRK, which is approximately 240 k€. [43] Applying a correction to account for inflation in Croatia from 2017 to 2025, a corrected figure of 308 k€ is obtained.

Despite these values referring to the three mentioned components, not the isolated cost of the $3.3\ MW$ water brake, they are still considered a relevant figure. This conclusion is based on the assumption that, because this component has significantly higher operating capabilities than the second brake, it was the major driver of the package price, given that the cooling system is assumed to be of a lower order of magnitude.

However, other data points suggest that the cost of the control mechanisms and additional system can significantly increase the cost of the power dissipation subsystem. For example, in December 2023, the US Government awarded a contract for a $900\ kW$ water brake and its respective control mechanisms at $489,563.50\ \$$ [44]. The inflation-adjusted value is $512760.80\ \$$, which, converted to euros, represents approximately 436 k€ at the current rate.

Given the significant variations in reported costs across different institutions, the level of uncertainty remains relatively high. Therefore, for illustrative purposes, a cost figure in the $0.5-1$ M€ band will be used for the analysis, assuming that while the control mechanisms make up for a significant fraction of the subsystem cost, their cost does not scale with the power brake as significantly as the brake itself, and are handled as a ”quasi-fixed” cost.

The lower boundary of this gap (0.5 M€) is based on the assumption that the cost of the additional mechanisms would amount to at least 50% of the total system costs, given the significant variation between the brake standalone and subsystem-level cost figures. In this case, this would represent 218 k€ for the lower-power brake awarded by the US Government, which, added to the 308 k€ from the Capax figure, would amount to 526 k€. This is considered an optimistic approach, as the control system’s cost will certainly scale with the increase in power level by a factor of 3, and this increase is expected to exceed the cost of the $1200\ hp$ portable brake included in the package. The upper boundary assumes a 100% error margin on the upper side, given the high uncertainty and limited data points.

Some additional cost figures for complete test facilities from the University of Nottingham, at between 1.2 M£ and 1.8 M£ ($1.37-2.06$ M€) [45], and the University of Strathclyde, at 1.89 M£ (2.17 M€) [46]. The mentioned Capax total facility cost of 2.1 M€ [47], suggests that the assumed range of values is plausible, considering that the power brake makes up for a significant fraction of the global facility budget, amounting to 50% of this value.

5.2. Water Pump

Another suitable option is to design a water pump that operates with a constant low-pressure water supply and dissipates the turbine-generated power by increasing water pressure. By developing the pump to operate at the same rpm as the turbine, it eliminates the need for a gearbox, removing that additional interface and the residual unbalance that results from it.

The enthalpy increase of the fluid is a function of the power input of the turbine as:

$$P = \frac{\dot{m} g_0 H_{ad}}{\eta_{pump}} \tag{5.11}$$

Where $\dot{m}$ is the mass flow rate at which the pump is operating in kg/s, η_{pump} is the pump efficiency, and H_{ad} is the adiabatic head rise in m, corresponding to, in the case of incompressible flow:

$$H_{ad} = \frac{\Delta h_s}{g_0} = \frac{\Delta p_t}{\rho g_0} \tag{5.12}$$

Where Δh_s is the adiabatic enthalpy increase in the pump.

Equation 5.14 can be rewritten as an explicit expression for the pressure increase of the working fluid as:

$$\Delta p_t = \frac{P}{\dot{m}} \rho \; \eta_{pump} \tag{5.13}$$

Δp_t is the usual design parameter for a test facility, as the existing base infrastructure constrains it. The mass flow rate is also a tuning factor for the outlet pressure and directly impacts efficiency, as shown in the pump's Ns-Ds chart.

This option can be seen as an alternative to the water brake, in which, instead of a significant increase in temperature, there is an increase in pressure. It should also be seen as an in-house developed alternative to a water brake (COTS), benefiting from the team's expertise in designing pumps.

To also obtain a figure of the required mass flow rate of water, the following assumptions are made:

- $\eta_{pump} = 0.7$ - following common values for rocket engine pumps
- $\Delta p_t = 210 \; bar$

Leading to a mass flow rate of water to dissipate $3 \; MW$ of power:

$$\dot{m} = \frac{P \rho}{\Delta p_t} \eta_{pump} = \frac{3 \times 10^6 \times 1000}{210 \times 10^5} \cdot 0.7 = 100 \; kg/s \tag{5.14}$$

The presented values for head rise and mass flow rate may sound quite high. However, they are comparable to values from rocket-engine pumps and therefore fall within the in-house field of expertise.

Looking at the Baljé design chart for pumps, it is visible that, similar to the case for turbines, the efficiency depends on the Ns-Ds pair, which depends, among other factors, on the head rise and the volumetric (thus mass) flow rate, whose relations are the following:

$$N_s = N \frac{Q^{0.5}}{{H_{ad}}^{0.75}} \tag{5.15}$$

$$D_s = D \frac{{H_{ad}}^{0.25}}{Q^{0.5}} \tag{5.16}$$

It is noticeable that these equations are very similar to the ones for turbines. The only difference is that the concept of adiabatic head rise is used instead of the adiabatic enthalpy drop in turbines.

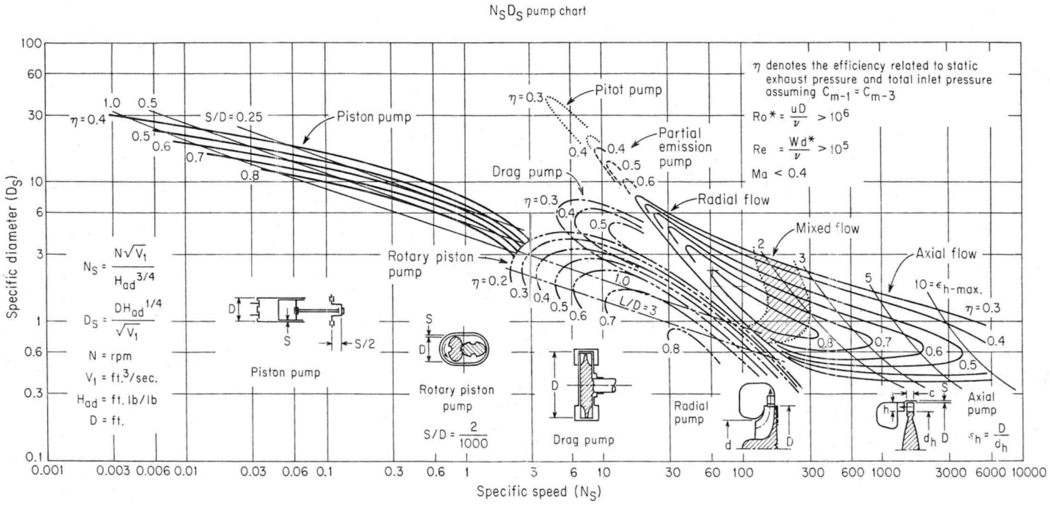

Figure 5.7: Baljé $N_s - D_s$ pump chart [48]

For this solution, different configurations using more than one pump can also be interesting. A configuration of two pumps in series represents a division of the head rise between the two pumps, with the mass flow rate remaining the same. In the opposite direction, a configuration with two pumps in parallel represents a subdivision of the mass flow rate between them, with both operating at the same head rise. These variations represent translations in the Ns-Ds diagram (Figure 5.7) that enable various design options.

While, at first glance, it would seem interesting to tune these translations in the Ns-Ds to obtain a lower efficiency, thus softening the mass flow rate and/or head rise requirements, this idea was later abandoned. The reason for this decision is that by staying in the optimal line, despite the higher operational requirements, the system operates in a well-researched domain with little room for unpredictable phenomena.

By designing an inherently inefficient pump, the risk of encountering this unpredictable behaviour was found not to outweigh the softening of the technical requirements. This is especially enhanced by the nominal requirements - a mass flow rate in the order of $100\ kg/s$ and a head rise of about $200\ bar$, not being significantly larger than the ones observed in pumps previously developed by ArianeGroup, and in this case using water, which is inherently easier to operate than LOx and LH$_2$.

5.2.1. Impeller feasibility study

Given that this solution would be developed in-house, it is helpful to conduct a feasibility study. This serves the purpose of not only checking if a pump with such characteristics would be attainable as a product of a design loop, but also to make use of the findings of this study to better anchor the scores for this option when performing the AHP.

Considering the indicative value of $200\ bar$ of pressure head, it is unfeasible to conceive of a purely axial turbine design capable of providing that. Therefore, this feasibility study will first consider the design of an impeller for a centrifugal pump, starting with the derivation of the Net positive suction head (NPSH) requirements to prevent cavitation. The available Net Positive Suction Head ($NPSH_A$) for a specified pump operating point is given by: [49]

$$NPSH_A = \frac{p_{s,in} - p_{vap}}{\rho g} \tag{5.17}$$

Where $p_{s,in}$ is the static pressure at the inlet, obtained from the total pressure by subtracting the dynamic pressure:

$$p_{s,in} = p_{t,in} - p_{dyn} = p_{t,in} - \frac{1}{2}\rho V_{in}^2 \tag{5.18}$$

V_{in} corresponds to the inlet velocity, which can also be expressed as a function of the mass flow rate and the impeller inlet area as:

$$V_{in} = \frac{\dot{m}}{\rho A_s} \tag{5.19}$$

Where A_s represents the pump's inlet suction area. This result can be introduced in Equation 5.18, to arrive at the final expression:

$$p_{s,in} = p_{t,in} - \frac{1}{2}\frac{\dot{m}^2}{A_s^2 \rho} \tag{5.20}$$

Returning to Equation 5.17 and its driving parameters, p_{vap} corresponds to the vapor pressure of the working fluid. This represents the value beyond which, if the static pressure exceeds it, gaseous water bubble formation begins.

Having an $NPSH_A$ larger than 0 is not enough to prevent cavitation from happening due to fluctuations around the operating points. To tackle this problem and quantify the $NSPH_A$ requirements, the concept of the required net positive suction head, $NPSH_R$, is introduced. This parameter is a characteristic of the pump that dictates the required inlet head needed to avoid cavitation. Therefore, the pump's operation, namely the media that is fed into it, shall obey the following rule:

$$NPSH_R \leq NPSH_A \tag{5.21}$$

Given the uncertainties of a design, a safety factor is usually taken. In this case, the value of 2 will be used, meaning the available net positive suction head shall be at least twice the required value.

To define the $NSPH_A$ and therefore the inlet pressure and suction duct size requirements, it is necessary to estimate $NSPH_R$. This is done through the Pfleiderer criteria [50], which models the $NPSH_R$ as a function of the suction diameter and the inlet velocity triangles as:

$$NPSH_R = \frac{\left(\lambda_C C_1^2 + \lambda_W W_1^2\right)}{2 g_0} \tag{5.22}$$

Where C_1 and W_1 are the absolute and relative inlet velocities, which in the case of a purely axial inlet flow are given by:

$$C_1 = C_{m,1} = \frac{\dot{m}}{\rho A_s} = \frac{4\dot{m}}{\rho \pi (D_{tip}^2 - D_s^2)} \tag{5.23}$$

$$W_1 = \sqrt{U^2 + C_{m,1}^2} = \sqrt{U^2 + C_1^2} \tag{5.24}$$

where U is the peripheral speed given by:

$$U = \Omega R = \Omega \frac{D_{tip}}{2} \tag{5.25}$$

By using the mentioned relations in Equation 5.22, and using the coefficients $\lambda_C = 1.15$ and $\lambda_W = 0.2$ as the midpoints in the recommended range on the CF Turbo software [51], it is possible to determine the suction diameter for which the $NPSH_R$ is minimum. This is the optimum diameter, as it is the one for which the $NPSH_A$ and, thus, the inlet static pressure requirements are lower, satisfying the criteria to avoid cavitation. Finally, a shaft diameter of $30\ mm$ was assumed to achieve a compact design and minimize operating loads.

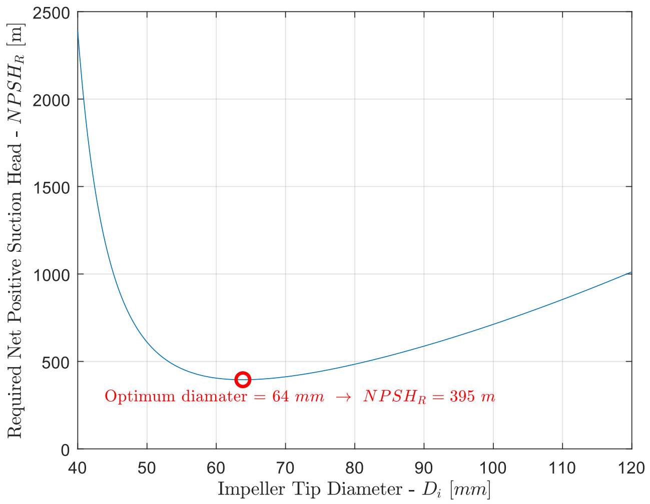

Figure 5.8: Required Net Positive Suction Head vs Inducer Diameter (Pfleiderer criteria)

As it is visible from the plot, the diameter that minimizes the required net positive suction head $64\ mm$ for which the $NSPH_R$ has a value of $395\ m$.

It is now important to determine how this value translates into the required inlet pressure to avoid cavitation. Given the safety margin taken as a factor of 1.5, the target $NPSH_A$ is given as:

$$NPSH_A = 1.5\ NPSH_R = 1,5 \times 195 = 592.5\ m \tag{5.26}$$

This allows us to compute the required pressure through the Equation 5.17, using a p_{vap} of $2.3kPa$, which is the experimental value for water at $20°C$. Please note that, despite being quite low, especially compared to the inlet total and static pressures, the vapour pressure is quite sensitive to the water inlet temperature. Therefore, special attention shall be paid if the inlet temperature varies significantly from $20°C$ to assess its impact on $NPSH_A$ and the required inlet pressure.

Combining Equation 5.17 and Equation 5.20 and rearranging as an explicit equation for the required inlet total pressure comes:

$$p_{t,in-R} = \rho g_0 \cdot NPSH_A + p_{vap} + 0.5\frac{\dot{m}^2}{\pi A_s^2 \rho} = 66.1\ bar \tag{5.27}$$

Where the suction area - A_s is given by:

$$A_s = \frac{\pi}{4}(D_{tip}^2 - D_{shaft}^2) \tag{5.28}$$

This result can be better visualized in the $NPSH_A$ plot, where a line representing required NPSH is added:

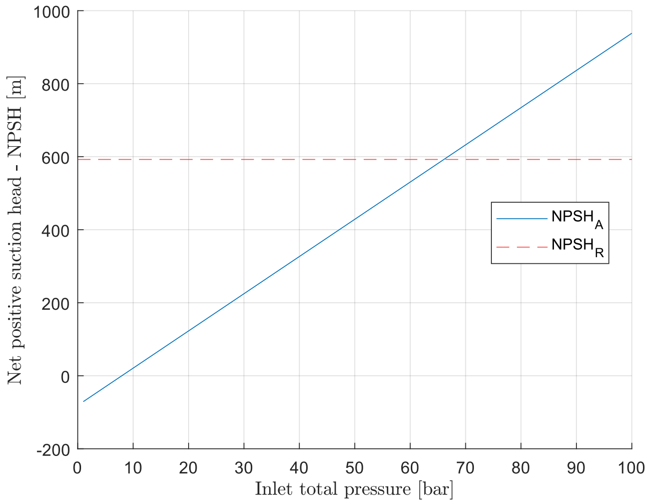

Figure 5.9: Inlet total pressure vs $NPSH_A$

As expected, the required inlet pressure to prevent cavitation is significantly higher than the ambient pressure. This issue can be solved by pressurizing the water tank with an inert gas such as gaseous nitrogen, which, given the mass flow rate of $100\ kg/s$, will require a significantly large volume of gas.

However, it may not be possible to pressurize the existing water tank to this pressure. If that is the case, there is an alternative solution. It consists of designing an inducer (axial pump) located upstream of the impeller, which is usually characterized by a lower $NPSH_R$ and a lower head rise. Due to the system's characteristics, it is not feasible to design a single inducer capable of achieving a pressure rise of 200 bar; therefore, it must always be combined with the impeller. However, a design of an inducer with a head rise of about $65\ bar$, to match the impeller requirements, is feasible. It can either remove the tank pressurization requirement or significantly reduce the inlet pressure required for the entire system (inducer + impeller) compared to the standalone impeller, thereby decreasing the inert gas mass needed for this process.

5.2.2. Inducer Feasibility study

To better understand the requirements for each option, a feasibility study will also be performed for the inducer. The goals of this study are to determine the minimum $NPSH_R$ that occurs for the optimal tip diameter - D_{tip}.

First, following a similar methodology to that used when designing the impeller, the required net positive suction head needs to be determined. In this case, it is done from the definition of the suction specific speed itself, as it is defined in [52]:

$$N_{ss} = \frac{N\sqrt{Q}}{NPSH_R^{3/4}} \tag{5.29}$$

where N is the rotational speed of the inducer in rpm, Q the volumetric flow rate in m^3/s. Given that in this definition, the factor g used in the non-dimmensional definition in [49] is missing, N_{ss} has the dimmensions of:

$$[N_{ss}] = \left[\frac{1}{g}\right]^{3/4} = [m]^{-3/4}[s]^{3/2} \tag{5.30}$$

To match the dimensions of the $NPSH_R$, which is expressed in m.

Given the values for the N_{ss} presented in [52], a specific suction speed value of 600 was assumed. A lower value than the ones provided in the reference was chosen, due to the higher density of the working fluid for this application (water) compared to the one used in the mentioned study - liquid oxygen.

Applying the target design point:

- $Q = 0.1\ m^3/s$, corresponding to a mass flow rate of $100\ kg/s$, similarly to the impeller
- $N = 50000\ rpm$ as the shaft is coupled to the turbine

Which, when replaced on Equation 5.29 returns the value for the required Net Positive Suction Head of $78.42\ m$

Given this value and the safety factor of 1.5 adopted, similarly to the one used in the impeller design, the target available Net Positive Suction Head comes as:

$$NPSH_A = SF \cdot NPSH_R = 1.5 \times 78.42 = 117.49\ m \tag{5.31}$$

To determine the inlet total pressure requirements, the inducer must be sized first to allow computation of the dynamic pressure.

To do so, a relation for the optimum diameter, which maximizes the cavitation number - K_d - minimizing the risk of cavitation is also provided through the Brumfield criteria [49]:

$$D_{opt}(ft) = 0.37843 \left(\frac{Q[gpm]}{(1-\nu^2)\Omega[rpm]\phi_{opt}} \right)^{1/3} \tag{5.32}$$

For this, a hub-to-tip radius ratio of 0.3 was assumed, based on the sample provided by [53]. A sensitivity study will be performed on this parameter to assess the impact of this assumption.

Equation 5.32 shows that the diameter also comes as a function of the optimal flow coefficient - ϕ_{opt}, which is obtained from the following relation:

$$\phi_{opt} = \frac{3574/S'_s}{(1+\sqrt{1+6(3574/S'_s)^2})/2} \tag{5.33}$$

S'_s is the corrected suction specific speed, using the hub to tip radius ratio as:

$$S_s = S'_s(1-\nu^2) \Leftrightarrow S'_s = \frac{S_s}{(1-\nu^2)} \tag{5.34}$$

However, this suction specific speed is in imperial units, which can be computed from the American definition described in [49]:

$$S_s = \frac{N[rpm]\sqrt{Q[gpm]}}{(NPSH_R\ [ft])^{3/4}} = 30987.0 \tag{5.35}$$

The corrected suction specific speed - S'_s comes as:

$$S'_s = \frac{S_s}{(1-\nu^2)} = \frac{30987}{(1-0.4^2)} = 34051.7 \tag{5.36}$$

Which leads to a value of ϕ_{opt} from Equation 5.33 of 0.0956. Equation 5.32 then leads to a D_{opt} of $0.270\ ft$, corresponding to $82.3\ mm$.

With this value of ϕ_{opt}, it is also possible to compute the cavitation parameter, to cross-check the validity of the N_{ss} assumption [53]:

$$K = \frac{2\phi_{opt}^2}{1-2\phi_{opt}^2} = 0.0186 \tag{5.37}$$

This is well aligned with the values presented in [53], being slightly above the lower limits. The ϕ_{opt} is also aligned with the values reported for inducers integrating the rocket engines presented by [53].

These results allow us to define, together with the target $NPSH_A$, the required inlet total pressure, which comes similarly as from the impeller, from Equation 5.27:

$$p_{t,in-R} = \rho g_0 \cdot NPSH_A + p_{vap} + 0.5\frac{\dot{m}^2}{A_s^2\rho} = 13.9\ bar \tag{5.38}$$

Similarly to the impeller, a visualization of the threshold pressure is presented in the following plot:

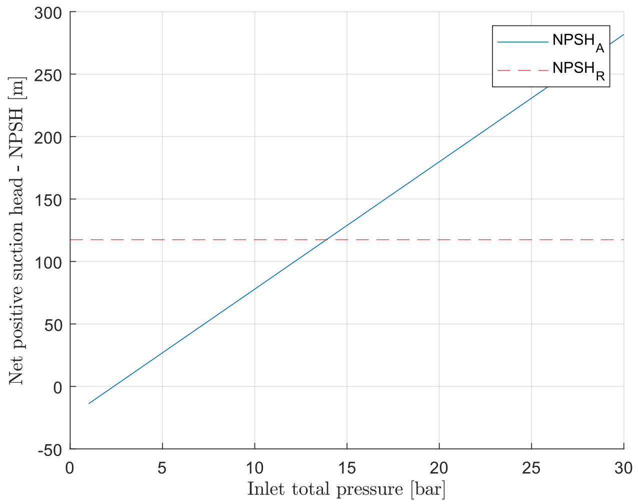

Figure 5.10: Inlet total pressure vs $NPSH_A$

Despite not being able to fully remove the tank pressurization requirement, the introduction of an inducer reduced the upstream pressure head requirement from $66.1\ bar$ to just $13.9\ bar$. This significantly reduces the resources needed to pressurize the water tank, while still preventing cavitation.

Following these results, the following pressure head rise requirements are set for the inducer and the impeller:

Table 5.2: Values for the required pressure rise for each pump stage

Stage	$\Delta p_t\ [bar]$	Tip Diameter $[mm]$
Inducer	52.2	82.3
Impeller	157.8	64.0
Total	210	$-$

With these values, the inducer can take the pressure from $13.9\ bar$, at which the water is pressurized in the tank to prevent cavitation on the inducer, to $66.1\ bar$, to prevent cavitation on the impeller. The impeller will then provide the majority of the head rise, to achieve a total pressure rise of $210\ bar$, required to dissipate the $3\ MW$ of power generated by the turbine (Equation 5.14).

5.2.3. Design with CF Turbo

To finalize the feasibility study, a simple design based on the calculated parameters will be generated in the CF Turbo software. The design will be conducted primarily in accordance with CF Turbo's suggestions, which are anchored in empirical relations, while adapting some inputs to align with the values obtained in the previous analyses. The goal of this exercise is to assess how the design parameters compare with the recommended ranges and to visualize the impeller geometry.

The following inputs were introduced:

- Inlet suction diameter - $D_{in} = 64\ mm$
- Inlet pressure - $p_{t,in} = 66.1\ bar$
- Shaft diameter - $D_{shaft} = 30\ mm$
- Mass flow rate - $\dot{m} = 100\ kg/s$
- Total pressure rise - $\Delta p_t = 157.8\ bar$

Furthermore, a pump diameter needs to be chosen from the Baljé $N_s - D_s$ design point. The empirical relations returned a value of $64.6\ mm$ to ensure that the pump design was in the optimal line. However, this value is not feasible as it is less than $1\ mm$ larger than the one inlet diameter. Therefore, a value outside the optimal range must be chosen. The value of $84\ mm$ was selected, providing enough radial length to have acceptable flow physics and velocity triangles. The Baljé chart returns an efficiency of 73.5% for this point. These values lead to the following geometrical design:

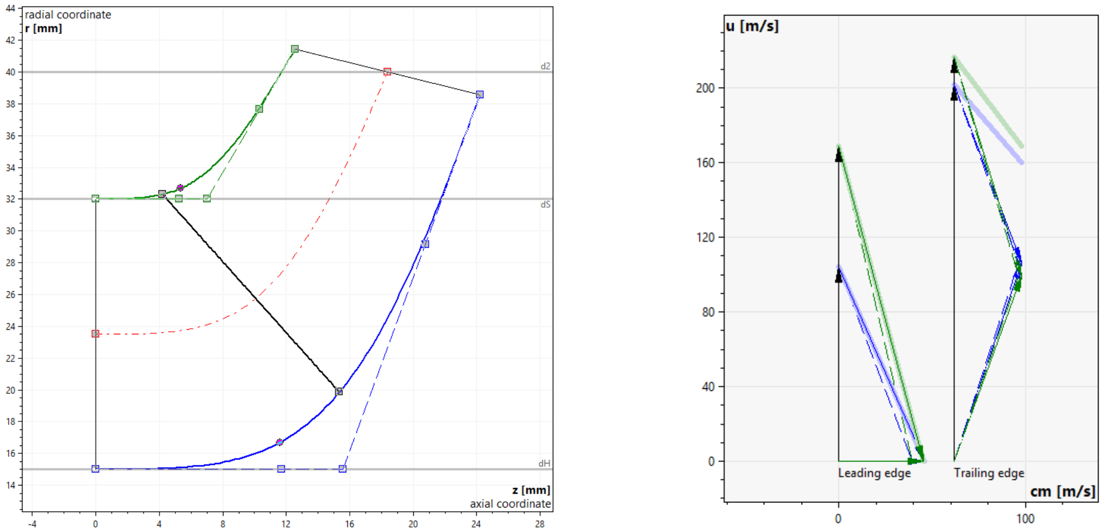

(a) Meridional View **(b)** Velocity Triangles

Figure 5.11: Impeller geometrical results of the design process

Representing a purely axial inlet flow (design parameter taken for simplicity), and an outlet flow following the geometry of the impeller (mixed-flow). The flow angles fall within the software's recommended intervals, indicating a feasible design.

Finally, a 3-D visualization of the geometry of the impeller can be found in the figures below:

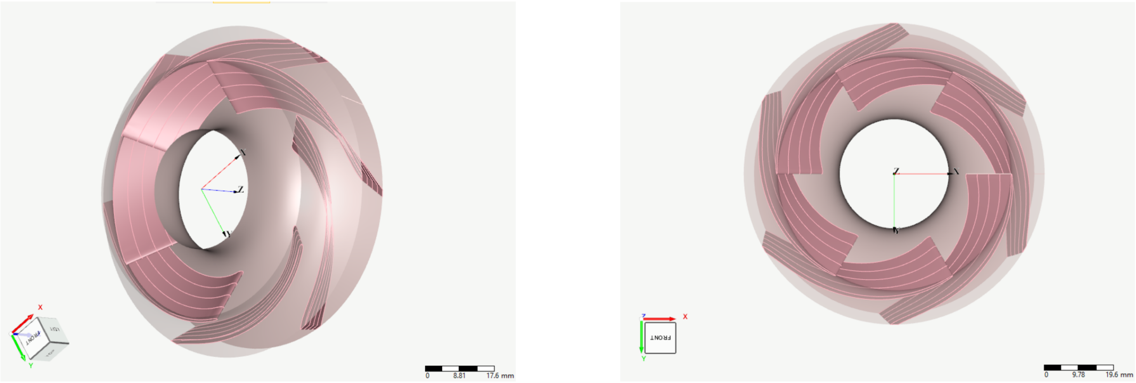

(a) Isometric view **(b)** Front view

Figure 5.12: 3-D impeller geometry

The conclusion drawn from this study is that, among the relevant parameters, the current design falls within the recommended range or is relatively close to it. This allows us to conclude that, in principle, such a design is feasible, though it requires further optimization through CFD simulations and structural analysis.

The efficiency of this stage is, as mentioned, 73.5%, which leads to a power dissipation of $2.15\ MW$, which represents 71.5% of the total power to be dissipated.

A similar procedure was followed for the inducer. The inputs used in the CFTurbo design were the following:

- Inlet suction diameter - $D_{in} = 82.3\ mm$
- Inlet pressure - $p_{t,in} = 13.9\ bar$
- Shaft diameter - $D_{shaft} = 30\ mm$
- Mass flow rate - $\dot{m} = 100\ kg/s$
- Total pressure rise - $\Delta p_t = 52.2\ bar$

Given these inputs, the ideal diameter, which would meet the optimal efficiency line from the $N_s - D_s$ chart (Figure 5.7) was found to be lower than the optimal suction diameter that minimizes the pressure requirements. Therefore, a decision to follow a suboptimal point, with an efficiency of 70%, was taken. By choosing this point, it was possible to match the suction diameter with the impeller shroud diameter. These design parameters lead to the following results for the geometrical parameters:

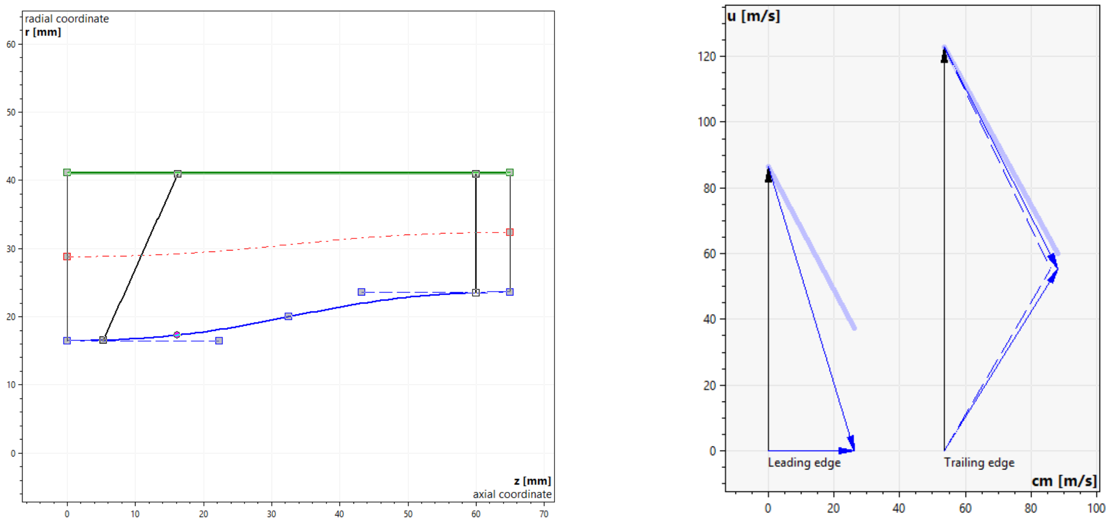

(a) Meridional View

(b) Inducer - Velocity Triangles

Figure 5.13: Inducer geometrical results of the design process

Similar to the impeller case, these velocity triangles represent a purely axial inlet flow that is diverted as the water pressure builds, increasing the radial component towards the inducer outlet. Additionally, the flow angles and the slip angle were found to be inside the CFTurbo recommendation margins, suggesting a feasible design in terms of the flowfield.

Finally, the following figure provides a 3-D visualization of the inducer:

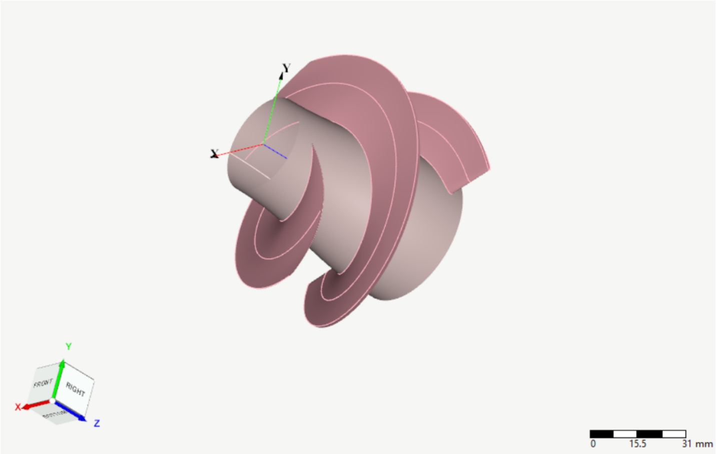

Figure 5.14: Inducer - 3-Dimensional Isometric View

As a final remark regarding power dissipation, the stage efficiency of 66.2% results from the CFTurbo design performance prediction (slightly lower than the one provided by Baljé, due to the introduction of the volumetric efficiency concept). This leads to a power dissipation of $0.79\ kW$ (from Equation 5.14), which represents 26.3% of the total power to be dissipated. By adding this result to one of the impellers, the total power dissipation is $2.94\ kW$, which is very close to the target, which can be easily achieved by slightly increasing the mass flow rate or the recirculation over the pumps, if necessary.

5.2.4. Startup

Importing the geometry into a CAD software, it is possible to perform an estimation of the moment of inertia of the impeller and the inducer. The values were obtained using the SolidWorks software [54] and are presented in the following table:

Component	Mass (kg)	J_p (kg m^2)	J_d (kg m^2)
Inducer	2.202	1.78×10^{-3}	2.12×10^{-3}
Impeller	5.24	2.53×10^{-4}	4.68×10^{-4}
Total	$\mathbf{2.726}$	$\mathbf{2.033 \times 10^{-3}}$	$\mathbf{2.588 \times 10^{-3}}$

Table 5.3: Mass and moments of inertia for the inducer and impeller

J_p represents the polar moment of inertia, which is the parameter of interest for this analysis. J_d represents the diametral moment of inertia, which will be later needed as an input for the rotordynamics analysis.

Additionally, the shaft can be modelled as a solid cylinder for which the moment of inertia is known and is given by:

$$J_{shaft} = \frac{\pi d^4}{32} = 7.95 \times 10^{-8}\ kg \cdot m^2 \tag{5.39}$$

It amounts to an almost negligible contribution due to the shaft's reduced dimensions.

This results in a total moment of inertia of $2.03 \times 10^{-3}\ kg^2$, which is far lower than the turbine's spin-up capabilities without a gearbox, while keeping the startup time under 1 minute. Therefore, it is concluded that, for the current pump design, neither a gearbox nor an auxiliary electric motor would be required for startup.

A gearbox may, however, be required if the base infrastructure cannot supply the required $13.9\ bar$ to the inducer, as the rotational speed is a driver of the large $NPSH_R$. The work will follow under the assumption that this is not the case, but the option is left as a recommendation for future work, in case limitations from the base infrastructure are encountered.

5.2.5. Cost Estimation

The fact that the pump is treated as an in-house-developed option makes cost estimation even more challenging than for off-the-shelf options. Fortunately, Shamoushaki et al. [55] provide cost correlations for power plant equipment, specifically compressors and pumps, among others.

These relations are purely a function of the input power and are anchored on a sample of 140 pumps in the range of $20 - 3500\ kW$, for which a regression coefficient (R^2) of 0.97 was obtained, indicating a suitable fit.

For the pump cost correlation, the formula is the following;

$$C(\$) = log(\dot{W}_p) - 0.03195(\dot{W}_p)^2 + 467.2(\dot{W}_p) + 2.048 \times 10^4 \tag{5.40}$$

The application of this equation would lead to an estimated cost of $1.13\ M\$$ by April 2021 (the date of the mentioned study). To translate this into today's currency, a correction using the Product Price Index (PPI) for Pump and Compressor Manufacturing was performed. This index increased from 163.500 points at the time of the study to 234.557 points by August 2025 [56], leading to an updated cost of 1.63 M, which corresponds to 1.38 M€ at the current exchange rate.

The results are reported to have a confidence interval of $\pm 9.4\%$ [55], placing the lower and upper boundary of the cost range at 1.25 M€ and 1.51 M€, respectively.

Based on the assumption that half of this value is spent on testing and manufacturing of the pump, the other half - 690 k€ is left for engineering labor costs. Using the standard value of 100 € per hour for hourly expenses per employee, this would translate into a team of 4 engineers working full-time (7 hours a day) for one calendar year, corresponding to 230 working days. This value is considered realistic and supports the application of the cost correlation in [55] to this application. Despite recognizing that significant deviations from this value can occur, it remains usable in the context of comparative studies of the options' costs. Finally, it is still important to note that having an experienced engineering team and developing a pump for which the optimization to increase efficiency is minimal can bring considerable savings and ultimately reduce this cost figure, as in the case of an in-house-developed pump.

5.3. Electric Generator + Resistive load

An electric generator of the alternator type can convert mechanical shaft energy into electrical energy. This energy conversion is achieved through the principle of electromagnetic induction, as described by Faraday´s law. Essentially, the alternator's rotor carries a magnet, which is situated inside the stationary coils of wire (the alternator's stator). When the rotor spins, its magnetic field sweeps past the stator coils, inducing an electromotive force (EMF) in them.

Then, up to a certain power level (facility-dependent), the electrical energy can be absorbed by the facility's power network. If this is not possible, a resistive load, in the form of a load bank, must be added to dissipate the electrical energy.

As with the hydraulic brake, there are no options on the market that simultaneously meet the requirements for power and rotational speed without a gearbox. Therefore, this option suffers from the same disadvantage of requiring the integration of another component axially, which contributes to rotordynamic unbalance and adds to the cost and complexity of the subsystem.

The key difference between this option and the previously mentioned ones is, inherently, that power is dissipated as electric energy rather than mechanical energy. This system requires a resistor that is sized based on the power levels.

This particularity is a positive factor for scalability, as power dissipation can be easily scaled by adding more resistors in series with the current infrastructure. However, the power level is also limited by the generator, which may also need to be replaced if the shaft power is increased significantly.

If a generator has a high enough power threshold, the limitations are primarily on the resistor side; the cost scales linearly with power output, as more resistors of the same grade can be added without replacing the current ones.

As mentioned, the resistor is a system composed of multiple resistor segments. The general upper limit for widely available segments in terms of power dissipation is $100\ kW$, despite reports on resistors up to $480\ kW$ being present in open literature [57]. If these widely available solutions, which can go up to $100\ kW$, were used, it would lead to 30 segments in an initial phase.

For a multi-MW application, as the one that is the object of this study, there are commercially available solutions denominated (containerized) load banks. These devices consist of pre-integrated resistor segments that can be handled as a single unit, with simplified interfaces. These solutions usually allow for scalability, leaving additional space to install more resistor segments, thereby increasing the system's power dissipation capabilities.

The internal wiring of the load bank (e.g., star or delta resistor arrangements) is typically specified by the manufacturer and thus outside the scope of this project. However, it is still relevant to illustrate the basic relationships between line voltage, phase voltage, and current. This provides decision support for selecting which generator and load bank voltage ratings are more practical at the multi-megawatt scale.

Using the common 3-phase network configurations— star (Y) or Delta (Δ)—it is possible to obtain a figure of the current (I) and voltage (V) at the load bank lines.

The total power in a 3-phase system is given by:

$$P_{3\varphi} = \sqrt{3} I_L V_L = 3 I_{ph} V_{ph} \tag{5.41}$$

Where I_L represents the line current, and V_L the line-to-line voltage. The parameter of interest when choosing an alternator/load bank pair is precisely V_L, as it is a specification of both systems. Given that the total power to be dissipated is $3\ MW$, the per-phase power is given by:

$$P_{\varphi} = \frac{P}{3} = 1\ MW \tag{5.42}$$

For the star configuration (Y), the phase current is equal to the line current, and the voltage is given by:

$$V_{ph} = \frac{V_L}{\sqrt{3}} \tag{5.43}$$

while the line current equals the phase current. The per-phase resistance is then given by:

$$R_{\phi}^{Y} = \frac{V_{\phi}^2}{P_{\phi}} = \frac{V_L^2}{P} \tag{5.44}$$

For a Delta (Δ) configuration:

$$I_L = \sqrt{3} I_{\phi} \tag{5.45}$$

While the line-to-line voltage (V_L) has the same numerical value as the phase voltage (V_{ϕ}), leading to the following phase resistance:

$$R_{\phi}^{\Delta} = \frac{V_{\phi}^2}{P_{\phi}} = 3\frac{V_L^2}{P} \tag{5.46}$$

Therefore, it is visible that for the same line-to-line voltage - V_L (equipment specific), and total power - P, a load bank whose wiring is arranged in a Delta (Δ) configuration uses 3 times the per-phase resistance of one in a star (Y) configuration. Nevertheless, due to the relation shown in Equation 5.41, the line current is the same, regardless of which configuration is used.

It is then possible to plot the line current as a function of the line-to-line voltage to better understand the implications of choosing a specific voltage rating, using once again the relation in Equation 5.41 rewritten as:

$$I_L = \frac{P}{\sqrt{3} V_L} \tag{5.47}$$

And using a power factor (PF) of approximately 1 for simplicity. The most common design points for the rated voltage are highlighted in red, along with the corresponding line current.

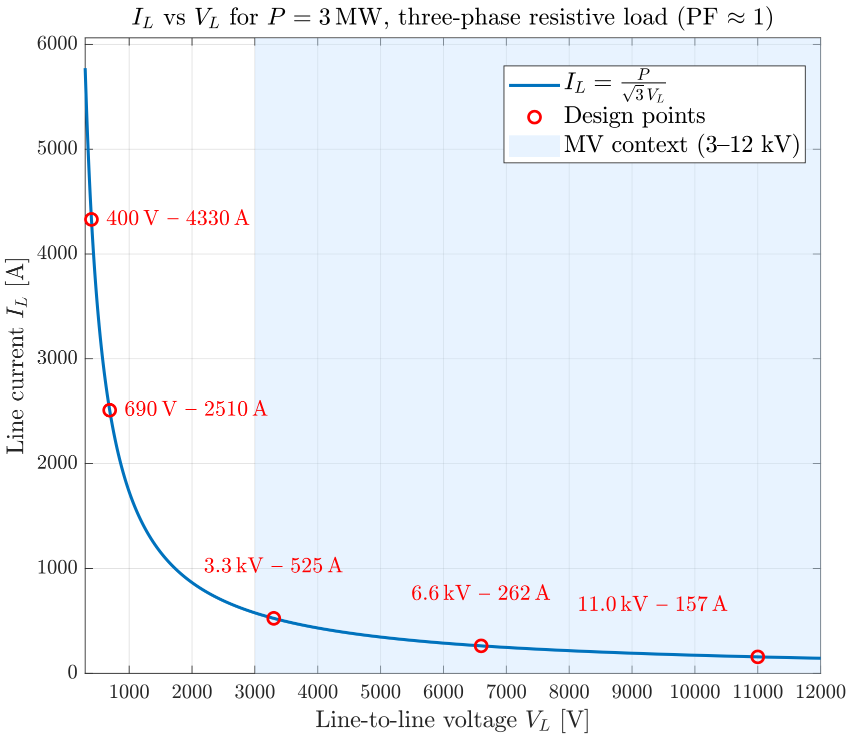

•

Figure 5.15: Line current (I_L) as a function of the rated line-to-line voltage (V_L)

As shown, reasonable current values begin to appear in the medium-voltage (MV) range, approximately $3\,kV$ to $12\,kV$. For this reason, and given the wide availability of commercial options within these voltage boundaries, only alternators and load banks rated within these values will be considered. The choice of going to the lower or upper end of this voltage interval depends on the existing base infrastructure and/or local regulations and is thus not within the scope of this research.

Startup

There are many alternator options available in suppliers' catalogs, each with direct values for inertia and rotational speed. The research on the standard capabilities of these devices highlighted technical results similar to those of the water brake. The first is that, without specialized and extensive equipment (transformers), it would be necessary to use a gearbox, as these devices are not rated for a mechanical shaft input spinning at $50000\ rpm$. The rotational speed is instead set by the number of poles and the electric frequency of the output signal, and is ruled by the following equation:

$$N[rpm] = \frac{120 f_e}{n_p} \tag{5.48}$$

where f_e is the electrical frequency and n_p the number of poles. Systems are mostly designed with 4 or 6 poles, and load banks are usually designed for $50\ Hz$, limiting the rotational speed from $1000\ rpm$ for 6 poles to $1500\ rpm$ for 4 poles. There are special models with only 2 poles, and some load banks are rated for higher frequencies, but this would lead to a significant cost increase and still not allow attainment of the required input speed of $50000\ rpm$, highlighting, once again, the need for a gearbox.

Secondly, because the values for the inertia are in the same order of magnitude as the ones for the water brake, with values ranging from 50 to $165\ kg \cdot m^2$. [58] [59]

Therefore, with a mandatory gearbox, the startup times remain within reasonable values. For example, if a gearbox with a transmission ratio of 1:10 is used, at the upper end of the range, the spin-up time using only the turbine would still be about 15 seconds. Once again, this value is still underestimated due to overestimating turbine torque during startup and the non-inclusion of gearbox efficiency. However, the margin relative to the previously defined 1-minute margin still leaves room for a 4x increase in spin-up time, which is far higher than the expected increase from including these effects.

5.3.1. Cost Estimation

There is a wide availability of off-the-shelf options for both alternators and load banks, as these devices are used in a wide range of applications. The cost estimate can be split between the alternator and the load bank. Starting with the alternator, the cost heavily depends on the rated voltage (Figure 5.15).

For a fixed rated power, the operating voltage ultimately determines the current over the lines, and therefore the complexity associated with cabling. $3\ MW$ alternators and load banks usually operate in Medium Voltage (MV) to High Voltage (HV) regime, ranging from $1\ kV$ to $36\ kV$ [60]. The most relevant design points sit at 3.3, 6.6, and 11 for this application, meaning a current of 525, 262, and $157\ A$, respectively. Going higher than this voltage is possible, but it results in further decreases in current and higher prices, along with concerns about working with high voltage.

The voltage is a project-specific trade-off: the cost of the alternator generally increases with voltage, but as current decreases, cabling becomes simpler and less expensive. Therefore, it is helpful to define a cost margin to allow flexibility in choosing different alternators rated for different voltages as a function of parameters such as base infrastructure capabilities or local environmental and safety regulations.

Fortunately, there is a published catalog from Marathon Electric [61] that lists prices for multiple alternators with different voltage ratings. The models that meet the requirements for this application and allow for providing a reasonable cost gap are presented in the following table:

Table 5.4: New MV alternator list prices (Marathon MagnaPower/MagnaMax, 4-pole, 50 Hz) [61] with 2025 PPI-adjusted values and EUR conversion (ECB ref. rate).

Model	# Poles	Frequency	Rated voltage (line)	Continuous rating (kVA)	List price (USD)	2025 (€) ECB ref. rate
1020FDH1228	4	50 Hz	6.3 kV	3,050	$351,202	€436,927
1030FDH1230	4	50 Hz	6.3 kV	3,288	$393,349	€489,362
1040FDH1232	4	50 Hz	6.3 kV	3,513	$430,723	€535,858
1040FDH1234	4	50 Hz	6.3 kV	3,988	$482,411	€600,162
1020FDH1228	4	50 Hz	6.6 kV	3,050	$351,202	€436,927
1020FDH1228	4	50 Hz	6.9 kV	3,050	$351,202	€436,927
1040FDH1256	4	50 Hz	11 kV	3,500	$411,274	€511,662
1040FDH1260	4	50 Hz	11 kV	4,025	$493,129	€613,497
1040FDM1194[a]	4	50 Hz	3.3 kV	3,300–4,250	$347,531	€432,360

Notes. [a] Model appears on the 3.3 kV table spanning multiple continuous ratings (approx. 3.3–4.25 MVA) depending on options.
PPI adjustment: Jan. 2018 list prices scaled to Aug. 2025 using U.S. PPI *Motors, Generators, Motor-Generator Sets* (WPU1173) [62].

EUR conversion: ECB euro reference rate on 2 Oct 2025 [63], 1 EUR $= 1.1754$ USD; EUR values computed as USD$_{2025}$/1.1754 and rounded to the nearest euro.

Regarding the load bank, Avtron - one of the largest manufacturers of such devices - has published a white paper [64] specifying the cost per kW for a $6\ MW$ load bank scenario. In this paper, the solution proposed by Avtron (True Direct-Connect Medium Voltage) is compared with the conventional medium-voltage solution using a step-down transformer and two load banks of $3\ MW$ each, which is the value of interest for the current application. It places the cost at $56.37\$$ per kW, leading to an estimated cost of $169,110\$$ in 2022. Corrected for inflation, this value would be equivalent to around $187\ k\$$ in 2025, or about 160 k€ at the current conversion rate.

Given the satisfactory level of cost datapoints for this particular power dissipation mechanism, the confidence interval is smaller than in the case of the water-brake. Factoring in uncertainties, a cost range of $0.6 - 0.8$ M€ was assumed.

5.4. Compressor

A compressor is a pneumatic solution for dissipating shaft power. Similar to a pump, a compressor increases the head (and thus the pressure) of a fluid. This process requires energy input from the turbine's shaft, dissipating the generated power.

The key difference between this solution and the pump is that in this case, the working fluid is a gas, which, for simplicity, can be ambient air.

The key advantage of this system is that the output is just high-pressure gas (air), which, up to a pressure level determined by environmental and safety regulations, can be vented from the system. This system eliminates the need for a catch tank or the disposal of large amounts of warm water. It also benefits from not requiring a base operating fluid, being more scalable, and being adaptable to variations in power, as it can operate at higher mass flow rates by simply sucking more air from the atmosphere.

Its power input (i.e., dissipated power) is driven by a similar equation to the pump:

$$P_{diss} = \frac{\dot{m}\Delta h_s}{\eta_c} = \frac{\dot{m}c_p T_{t,in}\left(\Pi_{ts}^{\frac{\gamma-1}{\gamma}} - 1\right)}{\eta_c} \tag{5.49}$$

In which the mass flow rate ($\dot{m}$) and the inlet total temperature ($T_{t,in}$) refer to the conditions of the media being driven by the compressor, in this case, the air being sucked from the atmosphere.

Equation 5.49 also shows that, similarly to the pump case, a design with low efficiency is advantageous, as it is capable of dissipating the same power level while keeping the outlet pressure at a lower value, for the same mass flow rate. Therefore, the tuning parameters for this application are the mass flow rate and the compressor's design efficiency.

Given the wide range of COTS compressor options, this power dissipation mechanism is not considered a development option in-house. The downside is that compressors are usually designed to maximize efficiency rather than minimize it. This leads to high outlet pressures or high mass flow rates to keep the pressure below a certain threshold.

Based on some assumptions, it is possible to obtain a rough estimate of the air mass flow rate required to dissipate power levels in the range of this application. The assumptions are made based on existing COTS compressors:

- $\Pi_{ts} = 20$ - considering a multi stage compressor from $1\ bar$ to $20\ bar$
- $\eta_c = 0.8$
- $T_{t,in} = 25^\circ\ C$ corresponding to a $c_p = 1.04\ kJ/kgK$

These parameters can vary from model to model, but the values are representative for an order-of-magnitude analysis. The following plot shows the evolution of the air mass flow rate and volumetric flow rate requirements for a shaft power varying from $0.5\ MW$ to $5\ MW$:

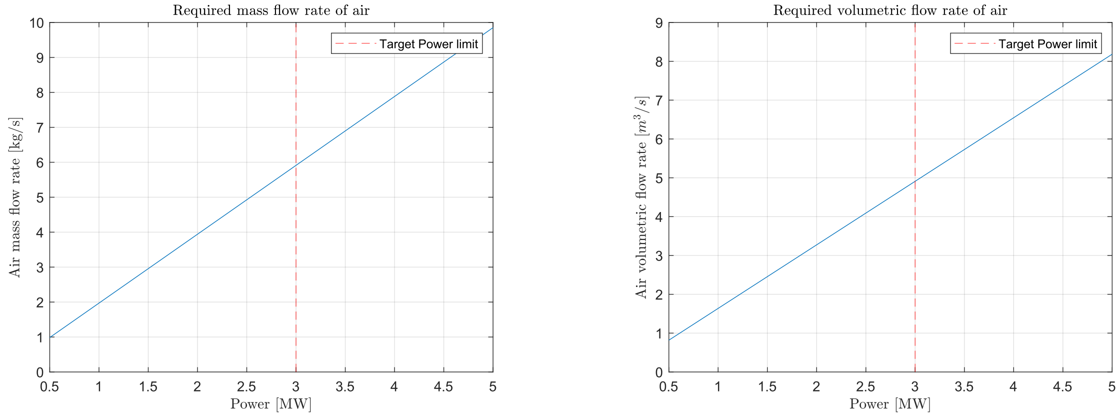

(a) Air mass flow rate requirements vs shaft power

(b) Air volumetric flow rate requirements vs shaft power

Figure 5.16: Compressor operating requirements

As shown, if these assumptions are met, a mass flow rate of roughly $6\ kg/s$ or a volumetric flow rate of $5\ m^3/s$ is sufficient to dissipate the target $3\ MW$ of power from the shaft. The mass flow rate increases linearly with the power dissipation requirements, leading to a dissipation capability of $5\ MW$ with a mass flow rate of air under the level of $10\ kg/s$ or slightly more above $8m^3/s$.

To keep the Mach number of the inlet airstream under 0.1, preventing any compressibility effects, the maximum inlet velocity is roughly $34.3\ m/s$. This allows for a preliminary sizing of the compressor's inlet duct as:

$$Q_{in} = A_{in} v_{in} \Leftrightarrow A_{in} = \frac{Q_{in}}{v_{in}} \tag{5.50}$$

To match the required volumetric flow rate of $5m^3/s$, the resulting inlet area is $0.146\ m^2$.

Assuming a circular duct, the diameter comes directly as:

$$D_{in} = 2\sqrt{\frac{A_{in}}{\pi}} = 0.43\ m \tag{5.51}$$

This value can be used as an estimate of the compressor's size, excluding any additional cooling or startup mechanisms. It shows that the system can be quite compact, enhancing flexibility during assembly and disassembly.

Regarding scalability, and given that this system is considered a COTS solution, it suffers from the same trade-off as the water brake. To achieve scalability, an over-dimensioned compressor would need to be purchased and operated at a lower operating point. The compressor, however, benefits from two characteristics compared to the water brake.

First, at $3\ MW$ of power dissipation, the indicative size and weight of such a device remain relatively compact, leaving a margin for an increase without a significant increase in assembly/disassembly complexity.

Furthermore, an initial market search revealed a wide range of models available for high-power applications. This can suggest that, contrary to the water brake (for which only the models with the highest specifications from the suppliers would comply with the power requirements), a compressor requiring such power input may not be close to the extreme end of the market solutions, leaving more options to explore and tentatively reduce the cost.

5.4.1. Startup

Regarding the startup, it is once again necessary to have a value for the inertia. After an extensive review of supplier catalogues, it was not possible to find a direct quote for the moment of inertia of an air compressor at a power input of $3\ MW$. However, [65] explicitly states in a Corrigendum published after the initial article publication that ”the mass moment of inertia for a compressor of around $1.5\ MWe$ is expected to be around $10 - 20\ kg \cdot m^2$.

Despite the compressor, the object of the article’s research, being a steam compressor, not an air compressor, as in the current application, and operating at half the power level, this can still be assumed to represent the lower end of the inertia of such a compressor. This assumption follows the principle that, in general, the size of the compressor (and, by consequence, its mass and inertia) scales with the power level. At the same time, the media generally has little impact on those parameters.

Therefore, the value of $10\ kgm^2$ could be considered very optimistic, given that it is expected to be significantly higher. Nevertheless, this optimistic value is already substantially larger than the capabilities of the turbine, so that it could meet a spin-up time lower than 1 minute, which occurs for a maximum of $6.57\ kg \cdot m^2$ as per Figure 5.6. As mentioned, there is a wide range of off-the-shelf options for compressors which meet the requirement of $50000\ rpm$, a trade-off would still need to be performed between a model with lower rpm capabilities combined with a gearbox, which would reduce the transmitted inertia and meet the spin-up time as shown in Figure 5.5. Alternatively, a compressor that allows for $50000\ rpm$ could be used, eliminating the need for a gearbox. Still, it would need an auxiliary electric motor to spin the shaft during startup. However, and despite which solution ends up being chosen, the takeaway of this analysis is that to use a compressor, either one of the options (power brake or auxiliary motor) would need to be used, while using none of them is unfeasible.

5.4.2. Cost estimation

Similar to the pump, the correlations presented in Shamousaki et al. [55] will be used to predict the cost of a compressor at the power level of this application. A sample of 160 centrifugal compressors in the power range of $10 - 10,000\ kW$ was used to derive the regression, obtaining a regression rate (R^2) of 0.99, indicating an almost perfect fit. The relation for compressors presented in the mentioned work is the following:

$$C(\$) = log(\dot{W}_p) + 0.03867(\dot{W}_p)^2 + 446.7(\dot{W}_p) + 1.378 \times 10^5 \tag{5.52}$$

which, for a power level of $3\ MW$, returns an estimated cost of $1.83M\$$ in April 2021, which, after applying the PPI to convert to present cost figures, returns a cost of $2.62M\$$ by August 2025, corresponding to 2.23 M€ at the current conversion rate.

For the centrifugal compressor case, the results are reported to have a confidence interval of $\pm 10.5\%$ [55]. Therefore, the lower and upper boundaries of the cost estimate are 2.00 M€ and 2.56 M€, respectively.

5.5. Trade-Off Process

Performing an engineering trade-off process is complex because it requires mitigating the bias of the person or group assigning scores to each option.

It requires an academic and industry-proven method, for which the Analytic Hierarchy Process (AHP) [22] has been chosen. The motivation for this choice is that it is the most well-researched and documented method for trade-off analysis in the literature. Furthermore, it has multiple metrics to assess the bias factors in the decisions, which are extremely valuable to this research, to mitigate to the maximum extent possible the bias that is introduced in the decision process.

However, to further control the bias that is input into the final score, performing a simple AHP is not enough. This happens due to the extreme importance of two criteria in every engineering project: cost and lead time. Trading off between technical and budget/logistics aspects in a single matrix often leads to a strong bias towards non-technical criteria, as most engineering projects operate under tight budgets and time constraints.

An improvement on the classic single-AHP trade-off is to perform an AHP trade-off between the technical criteria and plot the scores against the non-technical variables — cost and lead time. This is an application of the Pareto principle [66], which provides a methodology for trade-offs between criteria with conflicting objectives. By following this approach, it is possible to assess whether specific options are dominated by one another (for example, Option X has both a higher technical score and it is cheaper than Option Y). Before filtering out the Pareto-dominated options, a sensitivity study will be conducted to assess the robustness of the results to slight deviations in the criterion weights and candidate scores. Once the robustness of the analysis is ensured, the dominated options can be removed, reducing the list to contain only the most advantageous solutions. [67].

For the non-dominated options, or Pareto-optimal solutions, the trade-off is finalized through a project-specific preference, assessed by the relationship between the technical score and the non-technical parameters. For that, a decision support is written, which consists of a simple translation of the results into text (ex, Option X has a better technical score than Option Y, but it has a higher cost and lead time). The result may highlight a clear ”ideal” candidate, or lead to a more project-management-dependent decision when the candidates are ranked similarly. For the scope of this research, a final decision on the preferred solution will be made based on the available information. However, it is left to the critical design phase to reassess the options in case of relevant findings that may affect their scores and, consequently, the final result.

A flowchart diagram with the trade-off logic can be visualized in the following figure:

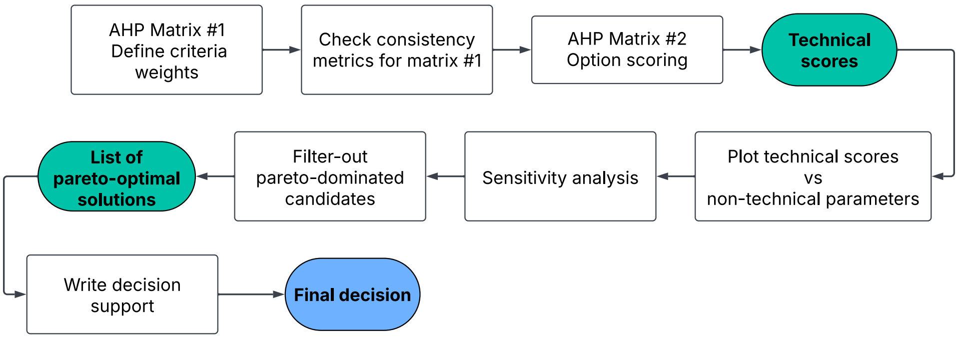

Figure 5.17: Trade-off process logic

5.5.1. Tecnhical Criteria

Having set the methodology for the trade-off and presented the non-technical criteria - cost and lead time - it is now left to define the technical criteria to be used in the initial AHP.

To avoid overlapping, a total of 4 technical criteria has been derived. These criteria reflect the objectives for the facility expressed in the requirements chapter (chapter 3).

In the classical AHP, pairwise matrices in which the options would be ranked for each criterion relative to each other would follow. However, it was identified that a hybrid model would be advantageous in this case.

This hybrid model translates the score directly into tangible parameters, so that scores in the range of 1 to 9 can be linked to absolute quantities. Therefore, there will be no consistency assessment after the second step of the AHP, as it is only applicable when relative judgments are performed. The presentation of the criteria and respective score translation follows:

Operation Complexity (OC) - quantifies the system’s operation regarding the complexity of meeting the safety standards, the assembly and disassembly times of the setup, and the nature of the inputs and outputs (high pressure, high temperature …), which is directly reflected in the extent of the safety protocol.

Score translation:

1. Multiple high-energy interfaces (high pressure, high temperature, hazardous fluids, high voltage >10 kV or >1 MW low-voltage current) which may require formal permits. System certification and shutdowns for assembly and disassembly take several weeks, intensive operator training, and specialist contractors.
3. Several primary hazardous interfaces; commissioning/assembly measured in multiple weeks; recurring special checks and operator training required. Extensive safety protocol reflecting the system's hazards.
5. Some local hazardous interfaces (local high-pressure or high-temperature sections, or HV panels). Needs a formal safety protocol and a few days up to 2 weeks for assembly and certification of the system; trained operators required.
7. Mostly routine industrial hazards; one or two higher-risk components; assembly under 1 week; standard operator training and modest special checks. The safety protocol is relatively simple, emphasizing the most hazard-prone sections.
9. Low-hazard system (low pressure/temperature, low-voltage control), simple safety protocol, can be assembled/commissioned within a day by regular staff. The nature of the systems allows for a straightforward safety protocol.

For this and all subsequent criteria, the scores (2), (4), (6), and (8) are intermediate scores to distinguish between candidates that, while fitting in the same category in the description, still have notable differences that favor one over the other.

Gearbox Penalty - Since the inclusion of a gearbox has significant effects on rotordynamics, substantially increasing the system's operating complexity, it was decided to apply a penalty to options that include a gearbox. It is estimated that 50% of the operational complexity concerns come from rotordynamics, so a penalty of 0.5 will be applied to the options that require a gearbox, using the following formula:

$$OC_{score} = OC_{initial} \cdot \lambda_{gb} \tag{5.53}$$

where $OC_{initial}$ represents the initial operation complexity score without including the rotordynamic concerns, and λ_{gb} the gearbox penalty, having the value of 0.5 in case a gearbox is required and a value of 1 otherwise.

It was decided not to include a safety criterion, as it was assumed that the safety standards must be met, regardless of how complex the process is. Therefore, the complexity of meeting these standards is still factored into the technical trade-off through the operation complexity criteria.

Required Base Infrastructure (RBI) - Quantifies the extent of the infrastructure necessary to operate each solution. It can take multiple forms, such as fluid tanks and feeding lines (which may serve as driving media/cooling, or lubrication), exhaust lines, or a power supply network.

Score translation:

1. Requires multi-MW power feed beyond typical industrial facilities' capability, extensive medium/high-voltage electrical lines (>10 kV), multiple high-pressure/high-temperature fluid lines, and permanent heavy civil works (large cooling towers, buried piping).
3. Multiple large fluid lines (≥2 high-pressure and/or high-temperature fluid feeding lines, and/or fluids with special handling complexity) and dedicated power infrastructure; cooling demands beyond simple closed-loop; likely need significant on-site works and permits.
5. Requires significant dedicated lines, which can take the form of extensive cooling/lubrication networks, exhaust systems, or up to one highly hazardous fluidic line (high-pressure and/or high-temperature). Power requirements exceed typical facility capabilities. Minor site works are likely needed to enable all the required inputs and outputs.
7. Needs reasonable industrial services, which can take the form of cooling loops and/or lubrication channels. Eventual power supply needs are within standard facility capabilities; conventional fluid lines (non-extreme pressure/temperature).
9. Self-contained or minimal infrastructure; fits within standard facility services; no special presence of high-pressure/temperature fluids or exceptional power supply demands.

Scalability (S) - Parameter that quantifies how flexible the upper limit of the operating parameters is. Quantifies the existing room for scalability in case, for example, power level or rotational speed increase, assessing the cost and effort required to perform such an upgrade.

Score translation:

1. The system is operating at its upper limits, and to increase its capabilities, it would need to be fully replaced by another model, which would entail a significant increase in cost and potential complexity (through operational complexity or a more extensive base infrastructure).
3. The system can be scaled without requiring a full replacement. However, this scaling is limited to a factor of 10% and requires significant financial and time effort to achieve, due to the mechanical changes required.
5. The system can be scaled to increase its operational upper limits by a factor of 10-50%. However, it brings substantial costs and time effort to implement the adaptations on the existing setup that allows for such an increase, as major component swaps or improvements to the base infrastructure may be required
7. The system is flexible enough to be scalable by a factor of 50-100% through the implementation of some adaptations. They can be achieved by either adding parallel modules or by modest upgrades, whose implementation is straightforward due to the system's modular nature.
9. The system can be easily scaled to increase its operational upper limits by more than 100% without significant cost or added complexity, thanks to its highly modular design. Adding parallel models or changing the operating point to achieve higher capacity can be realized without significant time and financial investment.

Reliability/Maintainability (RM) - quantifies how often each system is expected to fail, the extent of the failure modes, and the required maintenance to mitigate the risk for such failures.

Score translation:

1. Extensive maintenance is required after every use. Major subsystems must be replaced due to non-reusable components or catastrophic wear. Failure modes are catastrophic, leading to system or significant subsystem loss.
3. Reliability of key subsystems drops significantly within a few cycles. Frequent inspections and replacements are required to avoid unacceptable reliability loss.
5. System can run for 5–10 cycles before reliability degradation requires intervention. Inspections are periodic, with replacement limited to minor components, as failure modes are limited to minor subsystem degradation.
7. System operates reliably for many cycles or months before requiring inspection. Failures are rare and limited to minor, non-critical subsystems.
9. Very high intrinsic reliability. System lifetime and inspection intervals exceed the expected testing campaign by orders of magnitude. Little to no maintenance required as failure modes are negligible or outside the operational envelope

Having set the criteria, it is now possible to kick off the Analytic Hierarchy Process, starting with the trade-off between the criteria. This allows for defining the weights to be used in the final AHP, in which a trade-off between the candidates for power braking mechanisms will be performed.

For the initial AHP matrix, Saaty's scale [68], which assigns each value a relative importance, was chosen. The meaning of each value corresponds to the following:

- **1** – Equal importance
- **3** – Moderate importance
- **5** – Strong importance
- **7** – Very strong importance
- **9** – Extreme importance

Even numbers (2, 4, 6, 8) can be used as intermediate values to express judgments that fall between the main levels of importance.

Having set the scale, the populated matrix can be found below:

Table 5.5: Pairwise comparison matrix for the criteria

	OC	RBI	S	RM
OC	1	3	5	3
RBI	1/3	1	3	1/2
S	1/5	1/3	1	1/3
RM	1/3	2	3	1

The weights resulting from the Analytic Hierarchy Process using the scores from Table 5.7 are the following:

Table 5.6: Technical Criteria Weights resulting from trade-off

Criteria	Weight
Operation Complexity	51.17%
Required Base Infrastructure	17.52%
Scalability	7.80%
Reliability/Maintainability	23.78%

The rationale behind the decisions presented in the table follows:

- The operation complexity is the parameter that determines how fast and straightforward it is to test a turbine upon demand. Given the importance of flexible, rapid testing in an iterative development cycle, this is considered the most critical technical parameter.
- Reliability/Maintainability comes in second place. While considered significantly less critical than operational complexity, it is still highly relevant, as it defines the test facility's readiness to perform multiple consecutive test cycles without major maintenance requirements.
- The required base infrastructure comes in third, with a slightly lower weight than RM. It ultimately determines the ease of implementation of each power dissipation solution; however, its importance is limited, as it is seen as a one-time investment rather than a permanent concern, unlike the criteria ranked higher.
- Scalability comes as the least important parameter. While still relevant for future Research and Development projects, the sample showed that the combination of $3\ MW$ and $50000\ rpm$ represents a reasonable upper limit, with a considerable margin relative to the operating parameters of existing hardware. It is unlikely that these boundaries will be surpassed for (scaled) gas generator cycle turbines. Staged combustion turbines can operate at higher parameters, but, as shown in chapter 3, there is much more room to downscale the testing conditions further to meet these requirements.

To assess the consistency of the scores input into Table 5.7, the consistency ratio parameter is introduced. This parameter is a metric indicating whether there is any bias in the scores and shall remain within a defined threshold to ensure the scores are considered consistent.

Starting with the consistency index (CI), it is defined as:

$$CI = \frac{\lambda_{max} - n}{n - 1} \tag{5.54}$$

where λ_{max} corresponds to the largest eigenvalue of the criteria comparison matrix (Table 5.7), and n is the matrix size, i.e., number of criteria - in this case 4. By calculating the matrix's eigenvalues, a CI value of 0.347 is obtained.

The usual parameter of interest is the consistency ratio (CR). It is a normalization of the CI using Saaty's random index (RI), which depends solely on the number of criteria n. For $n = 4$ the RI has a value of 0.90, and the CR comes as:

$$CR = \frac{CI}{RI} = 0.386 \tag{5.55}$$

Saaty's rule of thumb [68] indicates that a CR value lower than 0.10 (10%) implies an acceptable consistency. When the value falls over 0.1, the judgments may be too inconsistent and should be revised. In this case, at 0.0386, the value is considerably below the threshold and therefore the judgments are considered consistent.

Having ensured consistency in the definition of the criteria weights, it is now time to rank each power dissipation mechanism candidate on each criterion to determine its technical score.

Table 5.7: Options ranking matrix

	OC	RBI	S	RM	Score (1-9)	Normalized Score (0-1)	Ranking
Water Brake	3.5	5	1	7	4.40	0.49	# 4
Water Pump	5	5	7	5	5.16	0.57	# 2
Generator + Resistor	2	9	5	7	4.49	0.50	# 3
Compressor	7	9	3	5	6.37	0.71	# 1

Note: the values for the Operation Complexity have already been corrected with the gearbox penalty, applied to the generator and the water brake.

With the technical scores, it is now time to perform the Pareto analysis, i.e., plot the technical parameters against the non-technical ones, specifically the cost. Recalling the cost figures:

Table 5.8: Cost Estimation Boundaries

Option	Cost Lower Boundary [k€]	Cost Upper Boundary [k€]
Water Brake	500	1000
Water Pump	1250	1510
Generator + Resistor	600	800
Compressor	2000	2560

And finally, plotting the technical scores against the cost, the following plot is obtained:

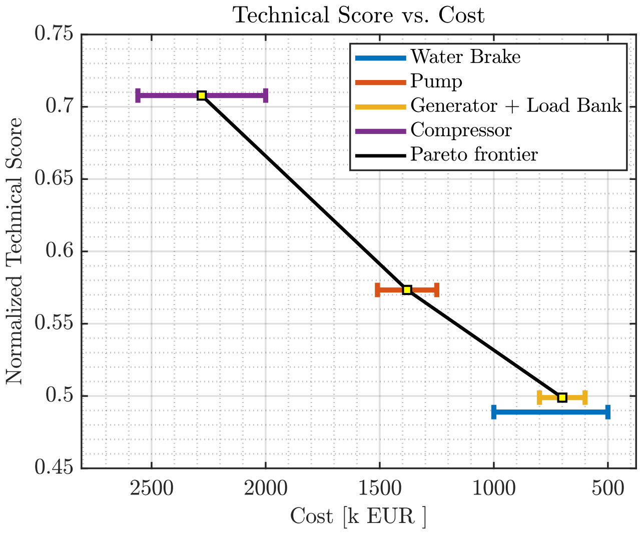

Figure 5.18: Technical Scores vs Cost plot

For an option to be considered Pareto-dominated by another, it must have both a lower technical score and a higher cost over the entire interval. In practical terms, it means the lower boundary of the cost needs to be higher than the upper boundary of the option dominating it. On the plot, a dominated option is located to the left of the black line — the Pareto frontier.

Having said this, and analyzing Figure 5.18, it is visible that there are no Pareto-dominated options in the case. This is primarily due to high uncertainty in cost estimation. For example, if the cost interval for the water brake were narrowed down to the top 200 k€, it would become dominated by the Generator + Load Bank.

However, given that it is not possible to reduce the mentioned uncertainty due to the project's limitations, a decision support will be written, also taking this uncertainty into account.

Regarding the sensitivity of the results, it should be noted that uncertainties of 11.1% $(1/9)$, for example, which correspond to the minimum difference on the 1-9 scale, can completely change the results. This is a limitation of conducting such research under a high level of uncertainty. However, for the scope of this research, the results are considered reliable, as extensive debate was encouraged within a specialized team of engineers. It is believed that the team's experience enabled the achievement of representative technical scores, which can be used for the trade-off. Nevertheless, it is recommended that further studies be conducted to mitigate uncertainties and support more robust decision-making.

5.5.2. Decision Support

Given all the analysis performed, the following statements can be derived and used as decision support.

- The compressor has the highest technical score (0.71) and the highest cost, starting at 2 M€ in the most optimistic scenario.
- The pump has a significantly lower technical score (0.57) at a cost that is also significantly reduced, ranging from 1.25 M€ to 1.51 M€.
- The Generator + Load Bank and the Water Brake have very close technical scores (0.50 and 0.49, respectively), and come at a reduced cost, under 1 M€ in the water brake case and 800 k€ on the generator case. The high uncertainty regarding the cost of the water brake raises the possibility that it will be dominated by the Generator + Load Bank if the cost is found to be at the upper end of the interval after more detailed studies.

5.5.3. Final Decision

Considering all the information obtained from the studies conducted, the characteristics of the options, and their respective pros and cons, it is now possible to select the preferred candidate for this application.

After careful consideration regarding the performance metrics, their correlation to cost, and the potential of each option, it was decided to select the water pump as the preferred solution. An overview of the reasoning behind this decision follows.

- While not being the highest in technical score, it presents a significant reduction in cost when compared to the winner in that criterion, the compressor
- Given that it is a solution to be developed in-house, it can benefit from some design choices and manufacturing techniques, and expertise that have the potential to reduce the cost. In fact, this cost figure could potentially be further reduced, reaching values even below the lower boundary of the confidence interval. This is because the pump is not specifically designed to achieve optimal efficiency and weight, for example, allowing the elimination of some design loops and the selection of lower-cost materials.
- The lower technical score for the compressor is primarily due to the high-pressure water stream at the outlet. However, a team with expertise in operating turbines on HydroLOx and/or MethaLOx combustion gases is assumed to be capable of handling high-pressure propellants, which, by nature, are significantly more hazardous and complex to operate than water. Therefore, while not overlooking the complexity introduced by this high-pressure media, its impact on the facility's overall operation may be limited.

- Compared to the lower-cost options - the water brake and the generator + load bank — it offers the significant advantage of not requiring a gearbox. This simplifies rotordynamics significantly by reducing the number of axial interfaces and, consequently, the residual unbalance.
- Performing an in-house development also benefits the design team regarding the earned expertise and ”lessons learned”. A team that has designed a water pump can more easily adapt it to meet potential changing requirements. It also benefits from the team members’ existing expertise in turbomachinery and/or pumps, in particular.

It is important to recall that this decision was made under several assumptions regarding both technical and non-technical parameters. Despite still considering this finding a useful insight, it shall be the subject of more detailed investigations to be followed subsequently to this research. A summary of the proposed follow-up research is presented in chapter 8.

6

Pillow Block Design and Rotordynamics

The shaft supporting subsystem must withstand the loads and vibrations encountered in all operating conditions included in the facility operating envelope. This design exercise is to develop a flexible mounting system that eliminates the need to switch between different pillow blocks during the testing of various turbines. For that, it must comply with the upper limits of all operating parameters, as defined in chapter 3. The pillow block is the nomenclature adopted for the bearing unit composed of the bearing itself and the respective housing. A schematic of such a unit can be observed in the following figure:

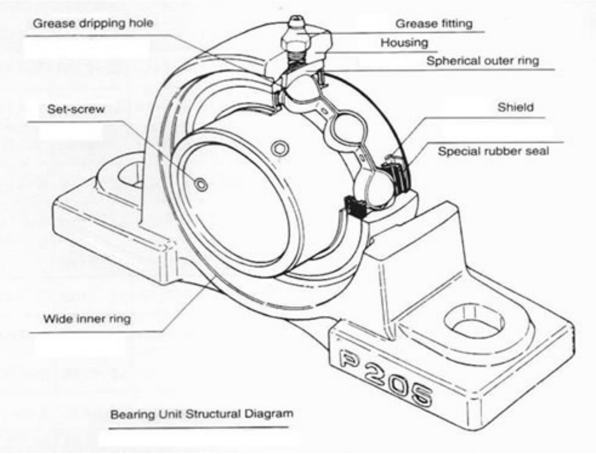

Figure 6.1: Schematic of a pillow block unit [69]

The depicted example is a grease-lubricated unit, but there are no significant changes for an oil-lubricated unit, apart from minor changes in the design of the lubrication channels.

In a turbine test facility, the shaft supporting subsystem consists of two pairs of bearings and their respective housings. Since the operating conditions for this application are extreme, adequate cooling and lubrication systems must be incorporated into the housing design. Due to the need to comply with all these parameters, it was decided that the housing shall be either designed in-house or outsourced as a custom-made component. Regarding the bearing, the option of using standard off-the-shelf components will be evaluated, as there is a wide range of available options.

Therefore, the design will start by calculating the bearing loads and assessing whether a suitable off-the-shelf model meets the requirements. Subsequently, a housing that complies with this bearing (and is flexible enough to allow for a change of bearings if a different application requires so), and is capable of thermally conditioning and providing lubrication for this specific bearing, will be designed.

6.1. Load Estimation

Given the intended flexibility for the test facility and the associated lack of a specific turbine model with well-defined loads, it is necessary to make a load estimation for the extreme case scenario in terms of loads. To do so, four sources of loads are considered:

- Axial thrust - coming as a product of the pressure difference acting on the two sides of the disk. Its direction is from inlet to outlet in the turbine, given the expansion process, and from outlet to inlet in the pump due to the pressure head rise in the axial direction.
- Gravity force - coming in the radial direction and proportional to the mass of the disk.
- Fluid dynamic loads - coming also in the radial direction due to uneven pressure distributions on the volute in semi-loaded points in terms of volumetric flow rate. These loads are much more significant in radial machines due to the geometry considerations and also on the pump side (hydrodynamic loads), due to the much higher density of the media (liquid water vs the turbine driving gas). The exact location of the force vector within the radial directions (i.e, the split between x and y components) depends on the internal pressure distribution.
- Unbalance loads - dynamic loads in the radial direction, which are brought by the uneven mass distribution on the disks resulting from machining.

A schematic of the resultant loads on a turbine stage can be observed in the following figure:

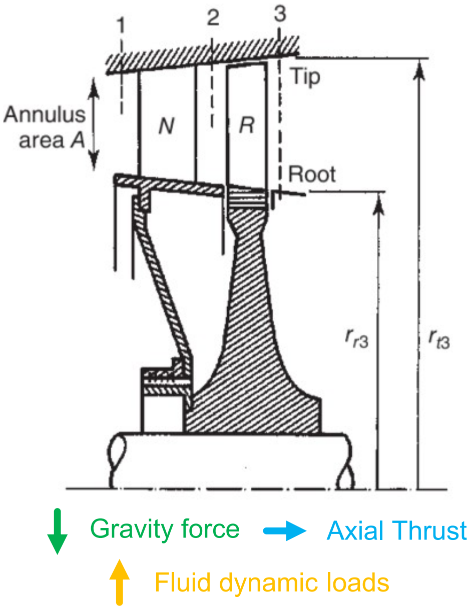

Figure 6.2: Resultant loads on a turbine stage (adapted from [70])

6.1.1. Axial Loads Model

The axial loads experienced by the bearings correspond to the axial thrust on the turbine rotors. The axial thrust over each side of each rotor has three separate contributions: the disk, the blade, and the labyrinth seal axial thrust.

$$F_{ax-rotor} = F_{ax-disk} + F_{ax-blade} + F_{ax-labyrinth} \tag{6.1}$$

Disk contribution

The disk is the main driver for the rotor's global axial force, as it has a significantly larger surface area than the other components.

The pressure difference across the rotors drives this axial thrust disk contribution due to the expansion process. Therefore, the force on each side of the disk, with surface area S, is given by:

$$F_{ax} = \int_S p(r,\theta)dA = \int_0^{2\pi} \int_{r_{hub}}^{r_{shroud}} p(r,\theta)r \; dr d\theta \tag{6.2}$$

This equation can be simplified under the assumption of a symmetric pressure distribution over the disk, i.e., no tangential direction influence on the pressure, so it is independent of θ. Therefore, the Equation 6.2 simplifies to:

$$F_{ax} = \int_{r_{hub}}^{r_{shroud}} p(r)r \; dr \tag{6.3}$$

From the equation, it is evident that to calculate the axial force, the radial pressure distribution along the rotor disk must be known. The only method to directly determine these values is to perform a Computational Fluid Dynamics (CFD) analysis. However, some models take the meanline pressure as input and return a pressure distribution along the disk. These models achieve a relatively high level of accuracy in estimating axial thrust. The model used in this analysis assumes a constant density along the hub, which has proven to be a good approximation in NASA studies [71]. Following the model, the radial pressure distribution is given by:

$$p(r) = p(r_{meanline}) - \frac{k^2\rho\Omega^2}{2}(r_{meanline}^2 - r^2) \tag{6.4}$$

where k is the slip factor, which represents the fraction of the tangential velocity of the disk - U - that is imparted to the velocity of the fluid - C_u. [71]

$$k = \frac{C_u}{U} \tag{6.5}$$

This value is not constant along the disk span. However, for the purpose of this investigation, a value of 0.1 is taken as a representative value for the span-average slip factor, following the test results observed in [71]. In a more detailed investigation, a CFD-based adjustment of the k factor across the disk's different regions can yield more accurate results. Given the approximation of a constant k factor, for simplicity, a constant K_a can now be defined:

$$K_a = \frac{k^2\rho\Omega^2}{2} \tag{6.6}$$

which allows to write Equation 6.7 simply as:

$$p(r) = p(r_{meanline}) - K_a(r_{meanline}^2 - r^2) \tag{6.7}$$

This expression can now be used in Equation 6.3, leading to the following axial thrust

$$F_{ax} = \int_0^{2\pi} \int_{r_{hub}}^{r_{rim}} \left(p(r_{rim}) - K_a(r_{rim}^2 - r^2)\right) r \; dr d\theta = 2\pi \int_{r_{hub}}^{r_{rim}} \left(p(r_{rim}) - K_a(r_{rim}^2 - r^2)\right) rdr \tag{6.8}$$

Blade contribution

For the blade, there are two contributions to consider: the pressure effect over the blade's annular area (similar to the disk) and the impulse force.

$$F_{ax,b} = F_{pressure} + F_{impulse} \tag{6.9}$$

The pressure term is driven by the different pressures acting on the two sides of the blade. As the blades are much smaller than the disk, it is a reasonable approximation to use the meanline pressure as the area-averaged pressure. This leads to the following equation for the resultant axial force due to the pressure contribution, where 1 corresponds to the inlet and 2 to the outlet:

$$F_{pressure-res} = A_{blade}(p_1 - p_2) \tag{6.10}$$

A_blade corresponds to the annular surface area of the blade, and p_{in} and p_{out} are a simplified notation for the meanline inlet and outlet pressures of the rotor, respectively.

Regarding the impulse term, it is defined, on each side of the blade, by:

$$F_{impulse} = \frac{1}{2}\rho V^2 \tag{6.11}$$

Where V is the absolute velocity on the blade. Given that the mass flow rate is usually more widely available than the absolute velocity, it can be written as a function of it:

$$\dot{m} = \rho A_{blade} V \Leftrightarrow V = \frac{\dot{m}}{\rho A_{blade}} \tag{6.12}$$

Therefore, the impulse contribution on each side of the rotor's blade can be written as:

$$F_{impulse} = \frac{1}{2A_{blade}} \frac{\dot{m}^2}{\rho} \tag{6.13}$$

And the resultant impulse force is then given by:

$$F_{impulse-res} = \frac{\dot{m}^2}{2A_{blade}} \left(\frac{1}{\rho_1} - \frac{1}{\rho_2} \right) \tag{6.14}$$

Finally, the resultant global axial force over each rotor blade section is given by:

$$F_{ax,b} = A_{blade}(p_1 - p_2) + \frac{\dot{m}^2}{2A_{blade}} \left(\frac{1}{\rho_1} - \frac{1}{\rho_2} \right) \tag{6.15}$$

Labyrinth contribution

The labyrinth region makes a small contribution to the axial thrust because of its smaller dimensions compared to the other contributing regions. As a result, it is a good approximation to assume that the area-averaged pressure is equal to the blade tip pressure. Therefore, the axial force on each side of the labyrinth is given by:

$$F_{ax,l} = p_{tip} L_h \tag{6.16}$$

where L_h represents the labyrinth height. The resultant force is then given by:

$$F_{ax,l-res} = L_h(p_{tip,1} - p_{tip,2}) \tag{6.17}$$

where 1 and 2 correspond to the rotor's inlet and outlet, respectively.

Given the reduced dimensions of the labyrinth when compared to the blade, and especially the disk, it was decided to neglect its contribution to the axial thrust. This decision was also driven by the fact that no geometric figures for the labyrinth in the literature are available to allow for an accurate estimate. This assumption will be taken into account when choosing the safety factor for the axial loads.

Global Results

Having set the model and the required approximations, data from a specific turbine must be used to compute its axial thrust, which can then be used to draw general conclusions.

As a result of the turbine dimensions, and in particular the fact that the disk's surface area is much larger than the blade and labyrinth annular areas combined, its contribution is, as mentioned, the main driver for the axial thrust. Furthermore, it is also noticeable that the axial force scales quadratically with the disk radius and linearly with the pressure:

$$F_{ax,d} \propto r_{disk}^2 \, p \tag{6.18}$$

This information helps determine which turbine — the fuel or oxidizer one — is driving the upper limit of the axial thrust requirements.

While oxidizer (or LOx) turbines feature lower mass flow rates and slightly lower operating pressures, they are generally larger. The effects of Equation 6.18 can be noticed when comparing Vulcain 2 oxidizer [72] and fuel [73] turbines, for which public datasets are available.

The meanline radius for the Vulcain 2 oxidizer turbine is $0.16\ m$, which is one third larger than the one for the fuel turbine at $0.12\ m$. This effect is particularly pronounced in the annular area, which is estimated to be close to twice that of the fuel turbine, assuming the same shaft diameter. This doubled area has a direct impact on the axial thrust, which is not compensated by the higher pressure on the fuel turbine side, as it is only about 30% higher. This would lead to the oxidizer turbine axial thrust being roughly 40% higher than that of the fuel turbine.

Due to the lack of public data on the fuel turbine's side, the same pressure ratios for each rotor as those published for the oxidizer turbine [74] were used. In reality, these values do not match perfectly, but for the scope of this study, the approximation is considered acceptable and aligned with the expected results. The results for the disk axial thrust on both turbines are represented in the following table:

Table 6.1: Full Scale Axial Thrust - Disks contribution

	OT	FT
R1 global [kN]	12.08	8.25
R2 global [kN]	-3.13	-2.13
Turbine Global - Disks [kN]	8.96	6.12

The absolute value of the axial thrust is 46% larger along Rotor 1 and 47% along Rotor 2 when comparing the oxygen and the fuel turbines of Vulcain 2. These values corroborate the findings of Equation 6.18 and are especially useful, as public data on the axial thrust of the oxidizer turbine is available in the literature [75].

In this document, there is a plot for the axial thrust as a function of the stage pressure ratio. For the first stage, it is also noted that the pressure ratio is 10.7, which, from the plot, corresponds to an axial thrust between $12\ kN$ and $13\ kN$, in line with the modeled values (Table 6.1). For stage 2, it is public that the global axial pressure ratio is 12, and given the 10.7 on the first rotor, 1.3 is left for the second stage. For this pressure ratio, the plot shows an axial thrust of roughly $-3\ kN$, which aligns with the modeled value.

As the radius has a bigger impact, the axial thrust is inherently higher for the oxidizer turbine. Given the magnitude of the difference, it is implausible that the blade effects compensate for it. However, the values were also computed to derive anchored conclusions:

Table 6.2: Full Scale Axial Thrust - Blades contribution

	OT	**FT**
Axial thrust - pressure (R1+R2) [kN]	2.50	2.42
Axial thrust - impulse (R1+R2) [kN]	0.03	0.22
Turbine Global - Blades [kN]	2.53	2.64

Note: a value of $20\ mm$ for the blade height was used for both turbines. In this case, the higher operating conditions on the fuel turbine side even out the effect of the larger oxidizer turbine radius, resulting in similar axial thrust values. This effect comes mainly from the squared contribution of the mass flow rate to the impulse. Nevertheless, the value is much smaller than the disk's forces, as expected.

Regarding the labyrinth, no public data on geometric parameters were found. However, standard rotor designs show that it has much smaller dimensions than the blade and therefore produces minimal axial force, so that it can be neglected.

Leading to the global values of axial thrust:

Table 6.3: Full Scale Axial Thrust - Global values

	OT	**FT**
Axial thrust - disks (R1+R2) [kN]	8.96	6.12
Axial thrust - blades (R1+R2) [kN]	2.53	2.64
Turbine Global [kN]	11.49	8.76

The previously calculated values refer to the nominal axial thrust during operation. However, given the scaled conditions where the pressure at all stations is reduced by a minimum factor of 5, the scaled axial thrust for the OT is given by:

$$F_{ax-scaled} = \frac{1}{5} F_{ax-OT} = 2.29\ kN \tag{6.19}$$

where in this case, for F_{ax-OT} the value of $30\ kN$, assuming the most extreme conditions for the disk, and that it drives the axial thrust value. The calculated value of $2.29\ kN$ will be used, together with the radial load requirements, which will be determined in the following section, to determine the bearing requirements.

However, these values are based on only two data points from two turbines. Therefore, and to extrapolate these results to a more general case, the most pessimistic values of axial thrust over the disk presented in [75] will be used as a guide to define the safety factor. This occurs for a first-stage pressure ratio of 14, resulting in $25\ kN$ of axial thrust and a second-stage pressure ratio of 2, resulting in an axial thrust of $5\ kN$. The turbine global axial thrust would be, in this case $30\ kN$. The value is overestimated due to the extremely high pressure ratio of 28, which is well above typical values for such turbines. However, it offers a generous safety factor against axial thrust and allows for generalization while leaving room to relax the bearing load requirements after further investigations. Comparing the values for the extreme case with the values in Table 6.3, it was derived that a safety factor in the order of 3 should be included to account for all the uncertainties.

This safety factor will be included after calculating the equivalent static load, as it provides a safety factor for both axial and radial loads, which will be derived under similar assumptions.

Pump Axial Loads

The pump's operation itself generates axial loads that must be considered. However, they occur in the opposite direction when compared to the turbine ones. The pressure head over the movable parts of the pump is much higher than in the turbine case, often requiring axial thrust balancing systems or dedicated thrust bearings to contain the resulting loads.

CFTurbo provides the values for the axial force, as they depend only on the geometry and the specified operating point. Axial forces of $-35.65\ kN$ for the impeller and $-20.99\ kN$ for the inducer are obtained, resulting in a total axial force acting on the pump of $-56.64\ kN$. Note that the negative sign shows once again that the resultant axial force on the pump has the opposite direction when compared to the turbine one. This value is much larger than the value observed in the turbine, despite the pump's smaller dimensions. This is a product of the high operating pressures, which are above the turbine's nominal operating point and, on top of that, are not scalable, as the pressure head rise itself dissipates the power.

This requires a dedicated mechanism to handle these loads on the turbine side, which may take the shape of an axial thrust balancing system or a thrust bearing rated for a load of $56.64\ kN$.

Given that the results indicate a specific balancing mechanism for the pump, its axial loads will not be considered in the bearing design chapter, assuming the balancing system is a mandatory section in the pump's detailed design.

6.1.2. Radial Loads Model

Radial loads on rotating machinery can come from three sources: rotor eccentricity (mass unbalance), hydrodynamic radial load (caused by the flow itself), and residual unbalance from the axial couplings.

For axial machines, such as the turbine used for this study and the inducer, the hydrodynamic radial load is negligible when compared to the rotor mass unbalance.

Therefore, for these machines, this study will focus on two significant contributions: providing an estimate with an acceptable level of accuracy.

In radial machines, such as impellers, the hydrodynamic radial loads are non-negligible. Therefore, the two contributions — mass unbalance and hydrodynamic loads — will be taken into account in the estimation of its radial loads.

Turbine

Without a specific turbine design and respective CFD simulations, it would not be possible to estimate the turbine's fluid dynamic loads with a sufficient level of accuracy. Therefore, given the much lower density of the driving media of the turbine when compared to the pump and its axial design (which also makes hydrodynamic loads less relevant), it was decided to neglect the hydrodynamic contribution to the turbine radial loads. The effect of this will then be taken into account when choosing a generous safety factor for the bearings.

Under this assumption, the relevant radial loads resulting from turbine operation are driven by the disks' mass unbalance. This unbalance is caused by the rotor's eccentricity. There are no perfectly machined parts in any of the components produced, and the rotors are no exception. To ensure that the eccentricity is within the acceptable levels for each application, the standardization in ISO 1940 shall be followed. In this norm, the maximum permissible eccentricity is specified for the application and value of each rotational speed. [76]

Rocket engine turbines fit the criteria of "Gas turbines and steam turbines" with the grade $G\ 2.5$, therefore having to comply with the following:

$$\varepsilon_{per}\Omega = 2.5mm/s \tag{6.20}$$

This means the highest permissible eccentricity at the rotational speed upper limit of $50000\ rpm$ is given by:

$$\varepsilon_{per} = \frac{2.5\ mm/s}{\Omega} = \frac{2.5\ mm/s}{50000\frac{2\pi}{60}\ rad/s} = 4.8 \times 10^{-4}\ mm = 0.48\mu m \tag{6.21}$$

The physical meaning of this value is that for this grade and rotational speed, the maximum distance between the center of mass of the rotor and the geometrical center is $4.77 \times 10^{-4}\ mm$.

Using this result, the maximum value for the mass unbalance can be computed, which naturally occurs for the maximum permissible eccentricity [77]:

$$U = m_{rotor}\varepsilon_{perm}\Omega^2 = m_{rotor}G\Omega \tag{6.22}$$

where G corresponds to the grade, in this case $2.5mm/s$. At a rotational speed of $50000\ rpm$, it leads to the following unbalance force:

$$U \approx 13.1\ m_{rotor}\ [N] \tag{6.23}$$

In the case of rocket engine turbine testing, the system is balanced to achieve a grade of $G\ 2.5$ as a whole, rather than balancing each rotor. In the case of a two-stage turbine, the total static force on the shaft comes then as:

$$U \approx 13.1(m_{r1} + m_{r2}) \tag{6.24}$$

where m_{r1} and m_{r2} correspond to the rotor 1 and rotor 2 mass, respectively.

To obtain a figure for the static force, it is left to estimate the rotor mass. This can be done following some approximations:

- The rotor is a single solid metal cylinder (metal removed during machining is neglected)
- The rotor is composed of a single material
- Both rotors have the same dimensions

Following these assumptions, the mass of each rotor is given by:

$$m_{rotor} = \rho_{alloy} V_{rotor} = \rho_{alloy} A_s t = \rho_{alloy} \pi r_{tip}^2 t \tag{6.25}$$

where A_s corresponds to the rotor's surface area and t the rotor thickness.

Considering that most turbines are produced using Inconel 718, which has a density of $8193\ kg/m^3$ [78], and using the meanline diameter data from [72], the assumptions for the blade height, the only missing parameter is the rotor thickness.

Observing the technical drawing (with redacted dimensions) in [79], it is possible to observe that the rotor has a variable thickness across the disks' span, following the standard design of such rotors. Knowing the meanline diameter, it is possible to make a proportion of the dimensions on the drawing to obtain an estimation of the rotor thickness. In the first half of the disk span, the thickness is approximately $30\ mm$, while in the remaining span it is roughly $10\ mm$. Therefore, an average thickness of $20\ mm$ will be used, leading to the following value.

$$m_{rotor} \approx 9.38\ kg \tag{6.26}$$

This value is obtained under the assumption that the combined height of the blade and labyrinth is $20\ mm$, which is generally higher than the values reported in the literature.

Following the approximation that both rotors have the same mass, Equation 6.24 allows us to compute the unbalance force as:

$$U = 13.1 \times 2\ m_{rotor} = 9.96\ g \cdot mm = 0.25\ kN \tag{6.27}$$

From a rotordynamics point of view, this force can be seen as a force of $0.125kN$ applied on each rotor center of mass, in the radial direction.

Pump

Both the impeller and the inducer also have rotordynamic radial unbalance, which will affect the deflections experienced during the system's operation.

Starting with the hydrodynamic unbalance, the following relation can be used to compute the radial force:

$$F_r = k_r \rho g_0 H d_2 b_2 \tag{6.28}$$

k_r is defined as a radial force coefficient, a pump-dependent parameter; g_0 is the gravitational acceleration in m/s^2, H is the pump's head, d_2 is the diameter at the outlet of the impeller, and b_2 is the impeller outlet width. Axial pumps (inducers) are characterized by low k_r values due to their geometry and internal flow characteristics. Therefore, this results in minimal hydrodynamic radial loads, especially when compared to the inducer's mass unbalance loads. Gülich provides relations for the k_r parameter, depending on the pump characteristics. [80]. The estimated values of k_r are dependent on the operating point in terms of volumetric flow rate. The conservative approach is to use the worst-case (highest) k_r scenario for a single volute to account for startup and shifts in the operating point. For the specific speed (n_q) of the impeller, which has a value 62.2, the maximum value for the radial thrust coefficient k_r is slightly lower than 0.4, so this value will be used. Therefore Equation 6.28 can be written as:

$$F_{r,hydro} = 0.4 \rho g_0 H D_2 b_2 \tag{6.29}$$

This result occurs at the point where the pump is closest to the being unloaded in terms of volumetric flow rate, as can be observed in the following figure:

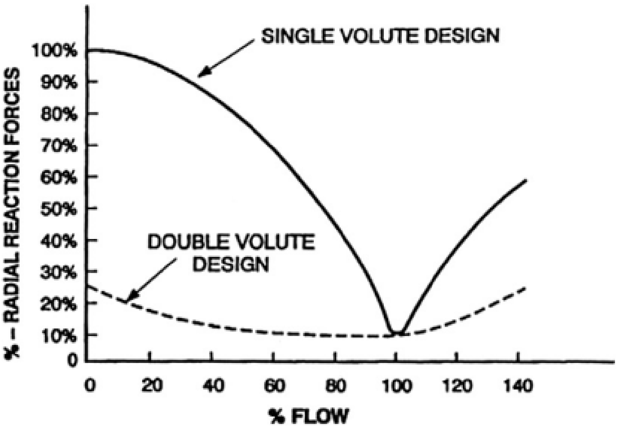

Figure 6.3: Pump radial loads as a function of the volumetric flow rate ratio to the best efficiency point (BEP) [81]

The numerical values can be computed from the impeller geometry and design point, yielding a hydrodynamic contribution to the static radial force of $6.06\ kN$. This is a significant value, largely driven by the impeller's high head, at $1608.6\ m$.

Regarding the dynamic loads, Gülich's most pessimistic value for $k_{R,dyn}$ will be used at 0.12. This results in a dynamic load of $1.82\ kN$.

For axial pumps (inducers) Gülich provides the following relation [80]:

$$F_R = k_{R,D} \rho g_0 H d_2^2 \tag{6.30}$$

With a $k_{R,D}$ value of 0.02 for steady (static) forces and 0.01 for unsteady (dynamic) forces. This results in a static force of $0.44\ kN$ and a dynamic force of $0.22\ kN$ for the geometry of our inducer.

Regarding the mass unbalance term, it is non-negligible for both the impeller and the inducer, especially given the high speed of this application. As per ISO 1940 [76], a balancing grade can be selected based on the application. Given that this pump is not considered flight hardware but rather test hardware, it may have a more relaxed grade than the turbine. With this in mind, it is assumed that the pump falls into the general "Pumps" category and requires a grade of $G\ 6.3$. Recalling the meaning of such a grade:

$$\Omega \varepsilon_{per} = 6.3 \frac{mm}{s} \tag{6.31}$$

And using the unbalance equation (Equation 6.22), which for $G\ 6.3$ translated into the following relation for the mass unbalance force:

$$U \approx 32.98 m_{rotor} \tag{6.32}$$

where the term m_{rotor} translates into the inducer and the impeller masses.

Table 6.4: Unbalance force on the pump

Stage	Unbalance Force - U $(g \cdot mm)$
Inducer	2.44
Impeller	1.28
Total	3.72

The values are relatively small compared to those of the turbine due to the pump's reduced dimensions, with its moving parts having much lower mass than the turbine rotors. However, they still account for roughly 40% of turbine unbalance, highlighting the importance of this value in the bearing design process.

Total Radial Loads

Taking into account all the previously calculated contributions, the overall values for the radial loads acting on the system are:

Table 6.5: Radial Loads summary

Section	Radial Load (kN)
Turbine (unbalance)	0.25
Inducer	0.507
Impeller	6.095
Total	6.853

And a total dynamic force of $2.04\ kN$, which it shall be noted to be an optimistic value given that the turbine contribution to this value has been neglected.

6.2. Methodology

Having defined the loads applied to the system, it is now necessary to determine the approach to be followed in the rotordynamics analysis.

In practical terms, the system consists of a flexible shaft on which two rotors are mounted, held by bearings, and coupled to the power-dissipating mechanism, in this case, the pump, on one side.

The system is treated as an undamped multi-degree-of-freedom (MDOF) rotor-bearing-damper assembly. The bearings used for this application were found to have negligible damping, requiring a separate damping system — the ”damper”.

Given the high-speed nature of the system, it is predicted that it shall be designed to operate in supercritical conditions, as the design rotational speed of $50000\ rpm$ is well above the values for the first and second forward natural frequencies of such a system. Therefore, the objectives of this analysis are to:

1. Quantify bearing loads
2. Identify critical speeds
3. Quantify resonance-crossing amplitudes during startup
4. Confirm stability margins at nominal operating speed

The choice of the bearing (i.e., its stiffness) directly affects the aforementioned parameters, requiring an iterative approach. Ultimately, the goal is to narrow down the stiffness window into a ”compliant region” which will be used as a requirement for the bearing supplier.

Given the significant uncertainties in the system design, which will only be reduced after a detailed design loop, the ultimate goal of this research is to perform worst-case scenario analysis for each of the mentioned objectives. With that, a ceiling for the subsystem requirements will be derived, followed by recommendations on how to reduce the value for such requirements, in case further studies indicate that to be advantageous.

To perform such an analysis, a Rotordynamics model capable of plotting Campbell diagrams and computing local shaft displacements is needed. The ROSS Python library [82] was selected for this purpose, which uses the Timoshenko beam theory [83] to model the system.

The workflow for such analysis is presented in the following figures, divided into analysis of the nominal operating point and resonance crossing (pseudo-transient) effects.

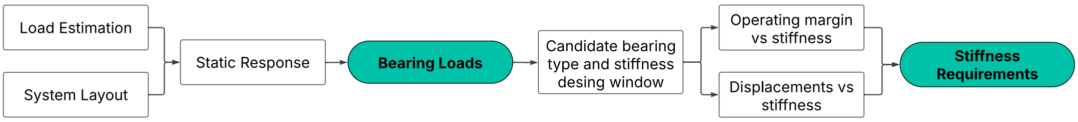

Figure 6.4: Rotordynamics Workflow - Nominal OP analysis

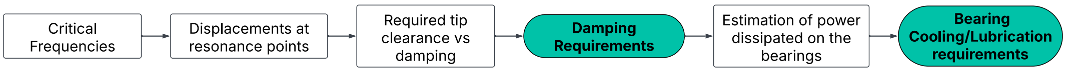

Figure 6.5: Rotordynamics Workflow - Pseudo-transient analysis

6.3. Rotordynamics

6.3.1. Model Definition

The first step for a rotordynamics analysis is to define the model's geometrical characteristics. This is particularly relevant because, in this case, the turbine and the pump have different shaft diameters, so the desired bearing location dictates the required bore diameter.

Defining the system requires the following parameters to be decided:

- Shaft dimensions, namely length and diameter
- Rotor positioning
- Bearing positioning
- Pump positioning and modelling

A technical visual representation of the derived system can be observed in the following figure:

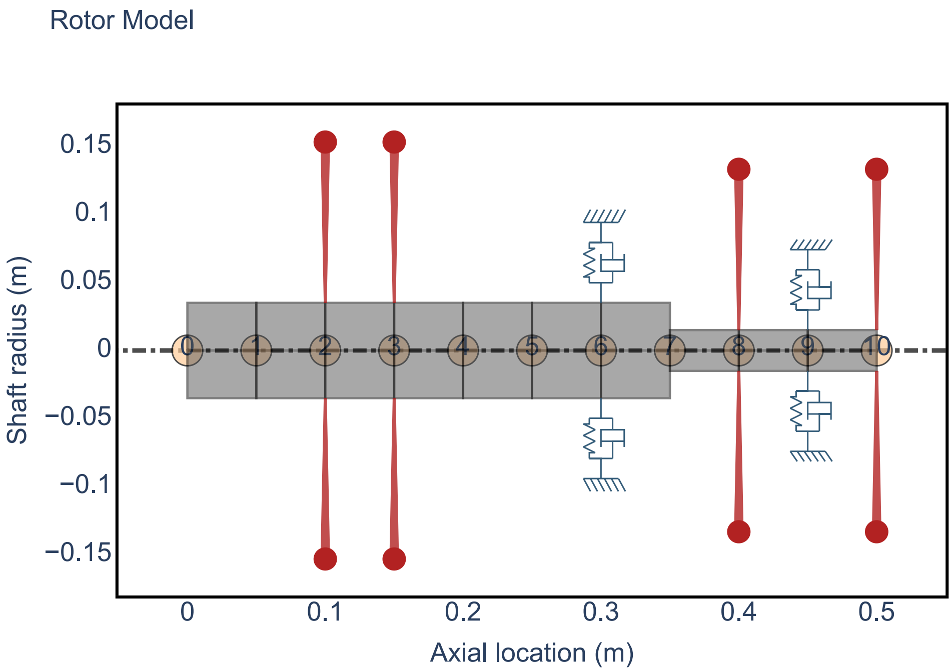

Figure 6.6: System Visual Representation

Starting with the shaft, the diameter is approximately $70\ mm$, coming from an estimation performed using the same technical drawing of Vulcain 2's OTP [79] as the one used to predict the disk dimensions in the load estimation section. Furthermore, it is considered a solid shaft. The length is slightly more complex, as it depends on multiple unknown factors, such as the space needed for instrumentation, cooling, and/or lubrication fluidic lines. On the other hand, a longer shaft indicates a larger cantilever distance between the bearings, which may raise concerns about local displacements.

For the purpose of this research, a shaft length of $0.5\ m$ is considered, leading to a length-to-diameter ratio (L/D) of 8.57. In ROSS, the shaft is initially modelled as 10 segments of $0.05\ m$ each, resulting in 11 nodes, numbered from left to right from 0 to 10. For some studies in which a higher discretization is desired, the number of nodes was increased by the required factor, reducing the element length and increasing the number of nodes by the same factor.

The first $0.3\ m$ of the shaft is occupied by the turbine, whose rotors are located at nodes 2 and 3, which are $5\ cm$ apart.

The bearings are placed to reduce the cantilever effect, which is proportional to the distance between the point of the shaft that is the furthest away from its closest bearing. Additionally, it is advantageous to locate the bearing as close as possible to the (radial) loads to reduce the bending moment at the bearing location.

Therefore, the first double bearing, which from now on will be named ”Bearing #1” or the ”Turbine Bearing”, will be located right after the turbine, on its right. This corresponds to node 6 (axial position (z)=$0.30\ m$). It is important to note that sets of double bearings arranged in a back-to-back configuration are assumed for this application, as recommended by the suppliers. This enhances the radial load capabilities while supporting axial loads in both directions, which may be important during transient operation.

Going further to the right in the shaft, the diameter reduction occurs. For the scope of this research, it is assumed that the shaft can be designed as a single part, with this diameter reduction from $70\ mm$ to $30\ mm$ at ($z = 0.35\ m$). If this assumption is found not to be valid in subsequent studies, a flexible coupling may be considered and modelled, as it will affect rotordynamics and load transmission.

Addressing the system from the pump side, it is possible to leverage the pump's modular design, namely that the inducer and impeller are separate parts with distinct casings. This allows for the second bearing, which from now on will be denominated ”Bearing #2” or the ”Pump Bearing”, to be located precisely between the inducer and the impeller. This not only reduces the cantilever effect on the right side of the shaft but also places the bearing equally distant from the centers of mass of the inducer and the impeller, where the loads are applied, minimizing bending moment.

The pump feasibility design indicated that the impeller has an axial length of about $24\ mm$, while the inducer has an axial length of $65\ mm$. Placing the impeller at the final node (node 10, $z = 0.50\ m$), the pump bearing at node 9 ($z = 0.45\ m$), and the inducer at node 8 ($z = 0.40\ m$), this leaves clearances of $17.5\ mm$ and $38\ mm$ between the double bearing center of mass and the inducer and the impeller centers of mass, respectively.

Looking at a few examples of angular contact ball bearings, the width of the bearing assembly is in the order of $25\ mm$ [84]. Despite a first look indicating compliance with the pump's clearances, additional systems, such as cooling lines and instrumentation, may require the bearing to be slightly shifted towards the impeller side, or the shaft diameter to be increased to accommodate all the necessary systems. This analysis will be performed under the assumption that the current clearance is sufficient, but it shall be reassessed in case the configuration is changed by updating the geometrical inputs.

Finally, a damper is added at node 7 ($z = 0.35$), which coincides with the place in which the diameter is reduced, allowing for the damper to be designed for a bore diameter of either $70\ mm$ or $30\ mm$, depending on the design effort in meeting each of the proposed geometries and/or the existence of compliant standard off-the-shelf parts. If the existing clearance (roughly $37.5\ mm$ on the left side and $17.5\ mm$ on the right side) is found to be insufficient, the shaft length may be increased to accommodate the component.

The numbers presented above are design assumptions and may change after a more detailed analysis is conducted. However, this work is performed under the assumption that these values are representative and, therefore, that the results from this work will provide representative guidelines. In case there are deviations in the dimensions due to further studies, this methodology can still be followed to update the results and obtain case-specific values.

Finally, the pump's impeller and inducer are modelled as disks, just as the turbine rotors, for simplicity. The dimensions again follow the pump feasibility study, while the inertia and mass values assume an inexpensive steel alloy is used to lower costs. The alloy selected for this application is the same as the shaft, with a density of $7810\ kg/m^3$. The inertia values are taken from the analysis performed with the CAD software in the mentioned section.

6.3.2. Bearing Design Considerations

Loads

Having performed the load estimation and established the system's geometrical configuration, the next logical step in this analysis is to assess the bearing loads.

The analysis is performed following the previously introduced assumption that the pump's axial loads are balanced by its specific balancing system, and under the hypothesis that there is no tuning also to balance out the turbine's axial thrust.

In this case, the axial loads from the turbine side must be considered, making the system a 6-degree-of-freedom (6DOF) system that allows translations and rotations along the three axes (x, y, and z).

Regarding the loads, the following assumptions are made, purposely non-consistent, to account for an extreme-case scenario that is never realized in reality and to avoid a transient analysis.

- The residual unbalance forces are the ones experienced at $50000\ rpm$, the maximum rotational speed for this system. Given that unbalanced forces scale quadratically with the rotational speed (Equation 6.22), the values at the maximum rotational speed will define the upper boundary of the loads due to mass unbalance.
- The radial loads on the pump side due to hydrodynamic effects are modelled using the highest value (worst-case), at which the pump is fully unloaded ($Q \to 0$), the point at which the radial load factor is maximum (Figure 6.3.

As previously introduced, in reality, these two operational points are contradictory, as the unbalance is maximum for the maximum rotational speed. However, at this operating point, the pump needs to be operating at the nominal point to dissipate the power generated by the turbine, and therefore close to the region where the radial load factor is minimum.

Nevertheless, given the uncertainty regarding the turbine's transient behaviour and starting times, these values provide an upper bound for the loads experienced in the system. More detailed analysis shall follow in the next design loop, which will ultimately identify the most critical load point, most likely to occur during transient behaviour. At such a load, neither of the loads (unbalance and hydrodynamic) is at its maximum value. Still, the resultant load is maximum and will, in any case, be lower than the one estimated in this study.

A summary of the loads applied for this analysis and their numerical values follows:

As this is only a force-and-momentum-balancing static problem (speed=0), this study is independent of the chosen bearing type and its properties, and depends solely on the bearing location. Nevertheless, it is necessary to obtain tangible results that can be directly applied to the bearing design.

For that, a parameter of interest is the equivalent static load, P_0, that combines the axial and radial static loads into a single design parameter. This parameter is given by:

$$P_0 = X_0 F_r + Y_0 F_a \tag{6.33}$$

where X_0 and Y_0 are the radial and axial load factors, respectively. For angular contact ball bearings, the most likely bearing type for this application, these parameters depend on the contact angle (α) and are specified in ISO 76 [85]. The contact angle acts as a tuning parameter to split the load rating between axial and radial loads. The value of $20°$ is used as an illustrative example, as it is one of the most common values observed in bearing catalogues. However, a different value may be considered if further studies indicate it is better suited to the application.

For $\alpha = 20°$, and an arrangement in a double row, X_0 has the value of 1 and Y_0 has the value of 0.84. [85]

For this configuration, the equivalent static load experienced is given by:

$$P_0 = F_r + 0.84 F_a \tag{6.34}$$

The required static load capability of the bearing - C_0 is given by the chosen safety factor S_0, as:

$$S_0 = \frac{C_0}{P_0} \tag{6.35}$$

The linear system is composed of the force vectors on each disk as shown in Figure 6.2 and the reaction forces on the bearings on the x, y, and z. By solving the system to achieve an equilibrium of forces and bending momentum at the bearing locations, it is possible to determine the bearing reaction forces. The following results were obtained for the loads acting on the bearings in each direction and the equivalent static loads they experience:

Table 6.6: Static Bearing Reactions (axial + radial + disk gravity)

Bearing #	**Axial pos. [m]**	F_x **[kN]**	F_y **[kN]**	F_z **[kN]**	P_0 **[kN]**
1	0.30	2.38	-0.37	-1.19	3.22
2	0.45	-8.53	0.16	-1.11	8.28

z corresponds to the axial direction and x and y the two axes perpendicular to it, both in the radial direction.

As mentioned before, the parameter of interest from the point of view of the bearing design is the equivalent static load P_0. To compute this parameter, the magnitude of the vector corresponding to the sum of F_x and F_y is taken as the radial force - F_{rad}. The values obtained can be used to determine the ceiling of the design requirement in terms of load capabilities for such a bearing. In the following section, this parameter and the remaining bearing design parameters will be addressed to allow conclusions on the feasibility of designing such bearings.

Load Rating and Attainable Speeds

This application has two particular characteristics: the high rotational speed and the presence of both axial and radial loads. This makes angular contact ball bearings, namely the subcategories of such bearings suited for high speed, the best bearing type for this application.

Given the physical limitations in bearing design and the bearings in suppliers' catalogues, it can be concluded that the problem splits into two.

First, for Bearing #1, with a bore diameter of $70\ mm$, the load ratings largely exceed the equivalent static load experienced of $3.22\ kN$, so this is not a design concern. However, in this case, what is a point of concern is the rated speed, which is no more than a direct result of the maximum peripheral speed at which the bearing can operate.

To assess requirements for rated speed, the widely used d_mN parameter is introduced. Numerically, this parameter is the mean diameter (between the bore and the outer diameter) in mm multiplied by the rotational speed in rpm. Physically, it is no more than a product of the peripheral speed as introduced above, as it is the rotational speed, this time in rad/s multiplied by the radius, in m ($\Omega\ r$). This value indicates whether a standard solution is capable of meeting the requirements. In this case, and assuming a bearing radius (between the bore and the outer circumference, or approximately the ball diameter) of $15\ mm$ [84] and a shaft diameter (thus bore diameter) of $70\ mm$ [79]:

$$d_mN = 85\ [mm] \times 50000\ [rpm] = 4.25 \times 10^6\ \frac{mm}{min} \tag{6.36}$$

Note: the definition of these parameter values varies among suppliers. The dN parameter is also commonly reported in literature and suppliers' catalogues. In this case, the bore diameter is used instead of the mean diameter. This research uses the SKF catalog as a baseline due to its wide availability and detailed information. SKF uses d_mN; therefore, it is the relevant parameter to compute for this application.

A d_mN value of 4.25 million is considered a very-high-speed application. While it is an attainable value, reported in various applications that even exceed it, it is not part of the standard parts catalog from suppliers. In fact, and using the SKF example, the series of standard bearings for whose dN rating is the closest to the target value is the SKF UltraFast Series, for which upper limits of d_mN values of $3.3 \times 10^6 \frac{mm}{min}$ for oil lubrication and $2.2 \times 10^6 \frac{mm}{s}$ for grease lubrication are reported for standard parts. [86]

Returning to the loads, the SKF 71910 ABA/HCP4ADG model [87] can be used as an illustration. This is the standard bearing from SKF with the largest bore diameter that supports still rotational speeds up to $50000\ rpm$. However, its bore diameter is $50\ mm$, being significantly lower than the required $70\ mm$.

Nevertheless, it is still relevant to observe its static load rating, C_0, which has a value of $15\ kN$, far larger than the estimated equivalent static load for this application (Equation 6.34), offering a generous safety factor, S_0, of 4.65.

It is also evident that the load rating generally increases with bearing size; therefore, a bearing of $70\ mm$ is expected to meet the load requirements, and the safety factor will increase further. The dynamic load rating is $18.2\ kN$, which, given the estimated figures in the load estimation section, does not bring relevant concerns and is expected to meet the requirements for such a design.

For Bearing #2, the problem is the exact opposite. With a d_mN value of $2 \times 10^6 \frac{mm}{min}$ ($40\ [mm] \times 50000\ [rpm]$), it is well within the speed rating capabilities of standard parts. The concerns are primarily about load ratings and attainable safety factors, as load capacities are lower for smaller bearings.

Given that the d_mN requirements are generally lower for smaller bearings, the SKF UltraFast Series only starts at a bore diameter of $40\ mm$. Therefore, the following bearing example belongs to the SKF Super Precision Angular Contact Ball Bearings, as it is the series that follows in terms of speed ratings.

Taking SKF 7006 CE/P4ADBA [88] as an example, the rotational speed is compliant with the requirements, while the static load rating is $10.4\ kN$, which, when compared to the equivalent load rating experienced by this bearing of $8.53\ kN$, offers a safety factor of 1.22 or 22%, which may be insufficient, depending on the requirements.

Given that the load is overestimated in this extreme-case analysis and that the axial load can be balanced by the pump loads, the actual safety factor of the bearing is underestimated. For a less conservative load estimation, this or another standard model is likely to be suitable for this application, making only Bearing #1 the custom-made design.

For the scope of this research, the work will be performed under the assumption that solutions for both bearings (with custom designs and potentially a standard bearing for the turbine side) are achievable, as there is no indication that the design requirements are unfeasible. However, if further studies indicate that a load rating that offers the required safety factor for Bearing #2 or the required d_mN value for Bearing #1 is unattainable, the system design needs to be reassessed. Tuning parameters could be, among other options, the diameter of the shaft on the pump side (changing the other pump geometrical parameters as a consequence), the bearings' axial positions on the shaft, or even slightly reducing the rotational speed capabilities of the system, as the current margin is considered generous given the existing turbine designs.

Therefore, this research will proceed with deriving the remaining requirements of the bearing and the pillow block, namely the bearing stiffness, lubrication, and cooling requirements. To do so, a parameteric rotordynamics analysis will be performed, following the workflow presented in Figure 6.5. These requirements will then serve as a baseline for future work, in which suppliers must be contacted to determine whether they are capable of designing a bearing meeting these requirements.

Stiffness Ranges

The bearing stiffness is an important driver of the system's behaviour, including critical frequencies and displacements. Therefore, it is essential to understand, for the current system configuration, which stiffness band provides acceptable results and ensures stable operating conditions.

To define the acceptable band, the operating margins must be assessed across the common design range of bearing stiffness. Unfortunately, SKF does not provide stiffness data for its UltraFast Series bearings, which have the highest rotational speed capabilities. Therefore, data for the super precision angular contact ball bearing series will be used to define the stiffness range. This bearing series has slightly lower rotational speed capabilities but is still close to our requirements and is assumed to provide an estimate of the stiffness range.

In fact, even the UltraFast Series bearings come in partial compliance with the requirements, being able to support the loads and having the required bore diameter of $70\ mm$, but not being compliant with the rotational speed of $50000\ rpm$. The selected series was the super precision angular contact ball bearings, as it has considerable data on stiffness while being relatively close to the requirements.

The axial stiffness (K_{zz} or K_{ax}) is not a fixed parameter and depends on the preload of the bearing mounting and usually varies in the $50 - 500\ \frac{N}{\mu m}$, or $5 \times 10^7 - 5 \times 10^8 \frac{N}{m}$ range for this type of bearing [84]. To generalize the values and leave room for eventual deviations, a wider range of $10^7 - 10^9 \frac{N}{m}$ will be used for the parametric study.

The axial load sources have opposite directions in the whole arrangement, as the turbine axial thrust is generated from the inlet to the outlet. The pump, with a meridional pressure increase, generates an axial force from the outlet to the inlet. This necessitates a double bearing in the Back-to-Back arrangement to support axial loads in both directions. This is done to address any concerns during transient modes, during which the resultant axial force may change direction.

For such an arrangement, Guay provides a relationship for the radial stiffness of a bearing as a function of its axial stiffness and contact angle - α [89]:

$$\frac{K_{ax}}{K_{rad}} = 2\tan^2\alpha \Leftrightarrow K_{rad} = \frac{1}{2\tan^2\alpha} K_{ax} \tag{6.37}$$

The table below presents the value for the correction factor in Equation 6.37 for the most common values of contact angle specified in ISO 76 [85], including the value for which $K_{ax} = K_{rad}$:

Table 6.7: Correction factor $f(\alpha)$ to convert axial to radial stiffness.

Contact angle α	$f(\alpha) = 1/(2\tan^2\alpha)$
$15°$	6.96
$20°$	3.77
$25°$	2.30
$30°$	1.50
$35°$	1.02
$35.26°$	1.00
$40°$	0.71

Applying this correction to the axial stiffness interval and with some rounding, the radial stiffness interval to be used will be from $7 \times 10^6 \frac{N}{m}$ to $7 \times 10^9 \frac{N}{m}$.

6.3.3. System General Behaviour

Looking at the system from a Rotordynamics point of view, the general ODE rules the system's behaviour [77]:

$$M\ddot{x} + C\dot{x} + Kx = F(t) \tag{6.38}$$

where M is the mass distribution of the system, C the damping matrix (in all directions) and K the stiffness matrix. $F(t)$ represents the external forces applied on the system in the time (t) domain. In this case, this factor represents the rotordynamic unbalance forces from the rotors.

The response vector x dimensions are a function of the number of degrees of freedom of the system. Suppose the system is totally unconstrained. Then, it is considered to have 6 degrees of freedom (6DOF), allowing translation over the three axes x, y, and z. This assumption was followed when computing the bearing loads in subsection 6.3.2. However, it can be noted that, even for the most conservative case in which the stiffness value is the minimum of the interval, the equilibrium axial displacements for the bearing that experiences the highest loads are given by:

$$\delta_{ax} = \frac{F_{ax}}{K_{ax}} = \frac{1190\ N}{10^7\ \frac{N}{m}} = 119\ \mu m = 0.119\ mm \tag{6.39}$$

Which is considered negligible given the total length of the shaft of $500\ mm$.

Additionally, this work is performed under the assumption that the axial thrust does not vary in nominal operation and is always equal to its maximum value, neglecting any eventual fluctuations.

Under the aforementioned assumptions, the axial behaviour of the system remains constant, allowing the radial analysis to treat the system as having 4 degrees of freedom (4DOF). Therefore, for this point onward, the analyses of the behaviour described by Equation 6.38 are made assuming that the vector x has four dimensions, allowing translations and rotations along the x and y axes, which correspond to the radial directions.

Having defined the system's constraints and degrees of freedom, it is now important to assess the system's natural frequencies. The value of such frequencies is significant, as they represent the shaft's bending modes and the points at which resonance can occur when the system is operated at these rotational speeds. On a simplified view, these frequencies scale with the mass and the stiffness (for a specified direction) through the following rule [77]:

$$f_n \propto \sqrt{\frac{k}{m}} \tag{6.40}$$

This highlights the importance of choosing an adequate bearing stiffness. The mass is not varying significantly, as it is an inherent characteristic of the system since the turbine, shaft, and pump dimensions are not subject to change in this analysis. For the scope of this research and given the target rotational speeds, the critical speeds of concern are the first, second, and third forward bending modes. Therefore, the system's natural frequencies scale almost exclusively with the stiffness. This can lead to three different scenarios:

1. Supercritical System - All the natural frequencies are situated below the operational frequency. There are no concerns regarding the nominal operating point. Still, during startup, when the system's rotational speed matches each natural frequency, the critical frequencies will require special attention regarding the deflection amplitudes.
2. Subcritical System - The exact opposite of the supercritical system and the most widely used operating regime. All the natural frequencies are well above the operational speed, and the critical frequencies are never met, avoiding resonance completely. While desired, achieving such an operating regime is often not possible in high-speed applications, as the one that is the object of this research.
3. Other systems - these systems are not supercritical nor subcritical. Some of the natural frequencies are below the nominal rotational speed, while others are above. For such a system, a defined margin between the nominal rotational speed needs to be ensured so that fluctuations in the operating point don't lead to resonance at the nominal operating point. Similar to the supercritical system, the startup also needs to be analyzed to ensure that the critical frequencies are passed through quickly enough so that no deflections with dangerously large amplitudes occur.

Given the large range of stiffness defined for this parametric study, it is likely that, for different radial stiffness combinations in each bearing, the system changes operating regime. Therefore, it is helpful to start by defining the system and plotting Campbell diagrams for some points of interest in (K_{rad1}, K_{rad2}). Note that K_{rad1} corresponds to the radial stiffness of the turbine bearing, while K_{rad2} refers to the pump bearing. For this analysis, the bearings are assumed to be isotropic, i.e., their stiffness properties are equal in all radial directions. Starting with the limits of the stiffness window (lowest and highest values of K_{rad1} and K_{rad2}), the Campbell diagrams are the following:

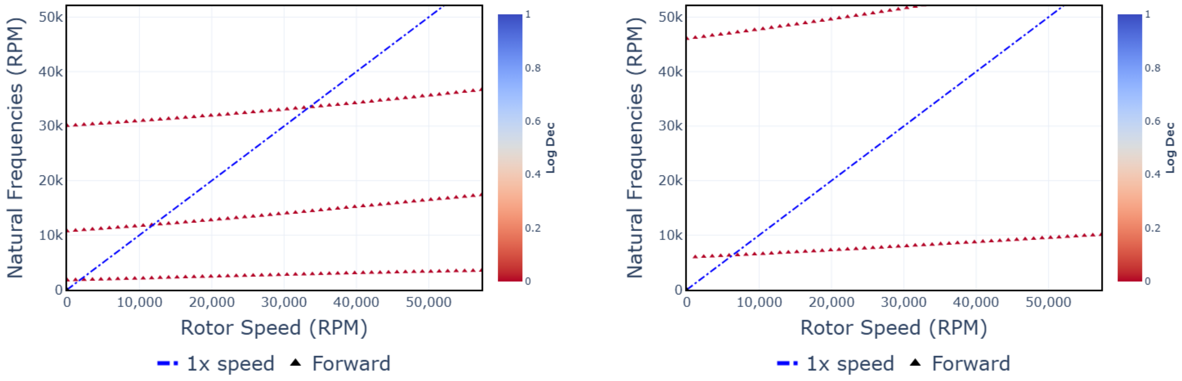

(a) Lowest stiffness combination $k_{rad_1} = k_{rad_2} = 7 \times 10^6 \ \frac{N}{m}$

(b) Highest stiffness combination $k_{rad_1} = k_{rad_2} = 7 \times 10^9 \ \frac{N}{m}$

Figure 6.7: Campbell diagrams for the lower and upper limits of the radial stiffness interval

These plots allow us to draw conclusions about the operating regime and how the ”nominal operation problem” can be addressed. The first conclusion is that, looking at the plot on the right, where the stiffness values are the maximum within the design window, the system will never be subcritical. This follows from Equation 6.40: given that the system mass is constant, for the highest values of stiffness, the natural frequencies will be the highest. However, even in the upper boundary of the interval, there are some natural frequencies below the nominal operating point ($50000\ rpm$). Any other combination of (K_{rad1}, K_{rad2}) will produce natural frequencies which occur at lower rpm, and therefore the system will never be operating below all the natural frequencies.

The plot on the left tells the rest of the story. If the stiffness decreased from a particular combination of Bearings 1 and 2 radial stiffness, the system will become supercritical, operating above all its natural frequencies.

These findings, together with the previously defined objectives for this rotordynamics analysis, allow us to divide the problem into two. First, the steady-state problem (i.e., nominal operating point, whose maximum sits at $50000\ rpm$), in which the critical frequencies will be identified and compared to the nominal operating point in terms of rotational speed. This process will allow us to confirm the stability margins during nominal operations. Furthermore, the displacements will be assessed using a worst-case load scenario. This will enable us to evaluate if the stiffness interval needs to be further constrained to prevent dangerously high displacement amplitudes.

Secondly, comes the pseudo-transient (startup) problem, which, using the previously identified critical speeds, involves analyzing the deflections at these points. The system will be analyzed from the extreme point of view, in which the system is operating nominally at the critical frequencies. A damping sweep will be performed at these points to determine the ceiling of the damping requirements.

6.3.4. Nominal Operation

To initiate the steady-state problem and return to the critical frequencies and the operating regime of the system, it is necessary to generalize the result observed in Figure 6.7 to the global radial stiffness interval.

To do so, first, a value for the required margin will be assumed, followed by a sweeping of the stiffness window in which the natural frequencies will be computed. Subsequently, the acceptable region of stiffness will be defined as the radial stiffness values for each bearing for which the margin is ensured, and the system can operate safely at its nominal state.

Given that the value of $50000\ rpm$ is assumed to be the upper limit of the rotational speed capabilities of the facility, this is the upper boundary of the interval for which it needs to be ensured that no critical frequencies are contained in. Looking at the turbine sample (Table 3.1a), a value of $40000\ rpm$ was selected to represent the middle of the range for the high-power (fuel) turbines. This value was combined with a 25% margin to allow for safe testing at rotational speeds ranging from $30000\ rpm$ to $50000\ rpm$.

For the lower-duty turbines, for which the rotational speeds are considerably lower, a separate study is recommended, as the possibility of operating in subcritical conditions is present and highly advantageous, completely mitigating the startup problem since critical frequency crossing does not occur.

The results of such analysis can be observed over the stiffness (K_{rad_1},K_{rad_2}) logarithmic grid:

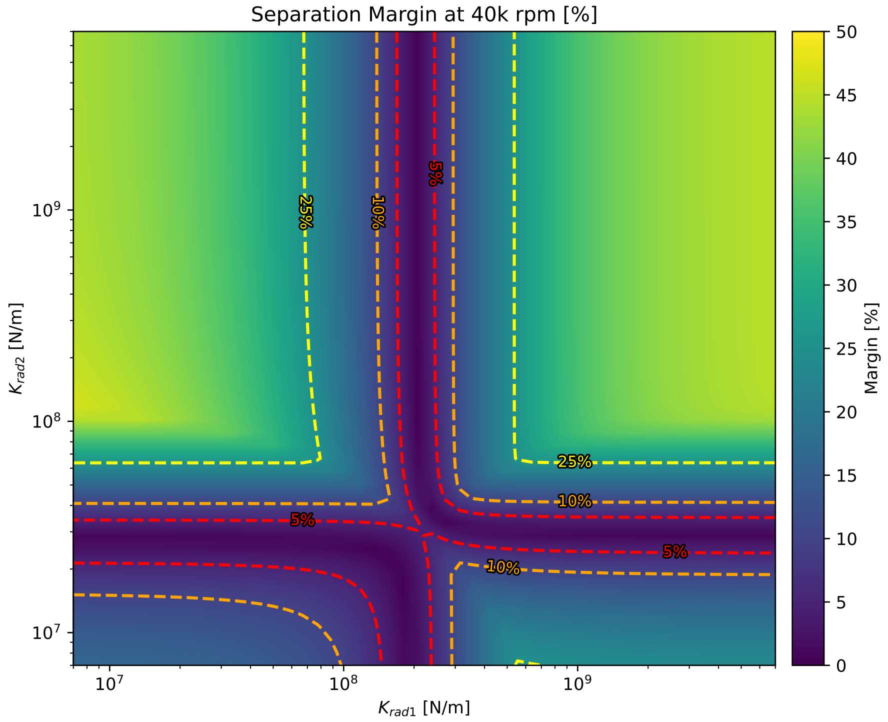

Figure 6.8: Margin to closest critical frequency (shaft bending mode) over the radial stiffness design window

From the plot, the forbidden bands of stiffness for the two bearings can be identified. Inside these regions, the system is considered to be nominally operating dangerously close to one or more critical frequencies and with the associated risk of resonance. The combinations of stiffness that verify this condition shall not be used. These bands are not equal for both bearings due to the asymmetric nature of the system, leading to a design with a larger stiffness for Bearing #2 (pump Bearings), corresponding to the top-right area of the plot, which is optimal in terms of rotordynamics.

Solely from a separation margin to the bending modes point of view, any design in the yellow regions of the space would be suitable. That would lead to a design on the top right side of the area (high stiffness for both bearings), which would be possible from a resonance avoidance point of view. However, in such a region, the required stiffness values for Bearing #1 are considerably high, sitting very close to the order of magnitude of 10^9. Although within the study's range, these stiffness values are outside the typical ranges for standard bearings. This is particularly relevant if damping properties are included in the bearings, as later studies will show that this has a negative impact on the bearings' stiffness.

Having this information in mind, the design process will proceed with special focus on the top-left side of the chart, for which bearing stiffness values within reasonable ranges observed in standard parts can be used.

Having defined the compliant stiffness window, it remains to assess the displacements at nominal speed to complete the steady-state problem. The displacements can be divided by the individual contributions of static and unbalanced responses:

$$\delta(z) = \delta_{static}(z) + \delta_{unbalance}(z) \tag{6.41}$$

The work in this section follows a similar assumption to that in the bearing loads calculations, using the worst-case load scenario. However, in this case, the unbalance is handled separately as a separate dynamic study.

Therefore, the static contribution comes from the worst-case scenario of the pump radial loads ($Q \rightarrow 0$, as per Figure 6.3) and the gravity force acting on the system. As an illustrative example, the static deflection values obtained for $k_{rad,1} = 2 \times 10^7 \ \frac{N}{m}$ and $k_{rad,2} = 10^8 \ \frac{N}{m}$ over the shaft's length are represented in the following plot:

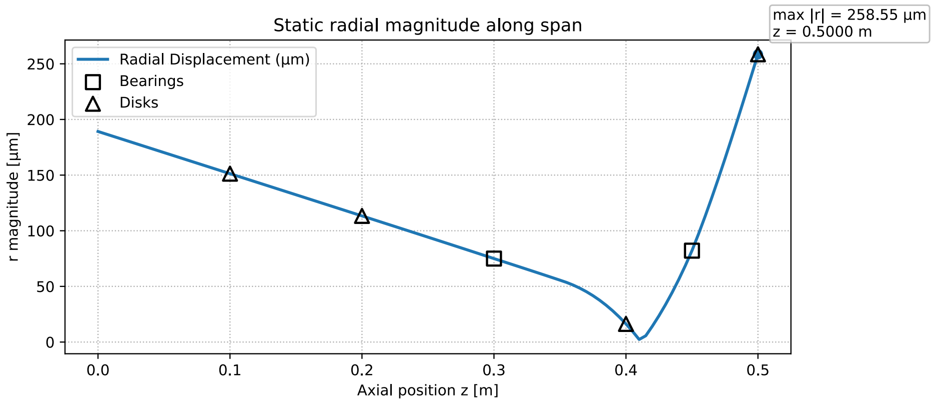

Figure 6.9: Radial magnitude of static deflections for $k_{rad,1} = 2 \times 10^7 \ \frac{N}{m}$ and $k_{rad,2} = 10^8 \ \frac{N}{m}$ over the shaft's length (z-axis)

The parameter of interest in this case is the peak radial displacement, as it drives the bearing requirements. For this reason, for the plot in Figure 6.9, the magnitude value of the displacement was taken rather than the signed displacement on one of the radial directions. Therefore, the inflection point around $z = 0.4$ is a consequence of the shaft bending in the opposite direction from the left side of the shaft.

An interesting visualization is that, despite the radial stiffness of the pump bearing being, in this example, 5 times higher than the turbine bearing, the equilibrium radial displacements are similar. This shows, once more, the uneven load distribution in the system, as the pump side is more heavily loaded when considering static loads. This is driven by the significant contribution of the hydrodynamic loads on the impeller, which amounts to $6.095 \ kN$. This is a consequence of the high head rise in the impeller and the overestimation provided by the extreme-case analysis.

Regarding the dynamic contribution, which consists of the response of the system to the unbalances calculated in subsection 6.1.2. The results, for the same example values of stiffness and when operating at the maximum rotational speed ($50000 \ rpm$), are the following:

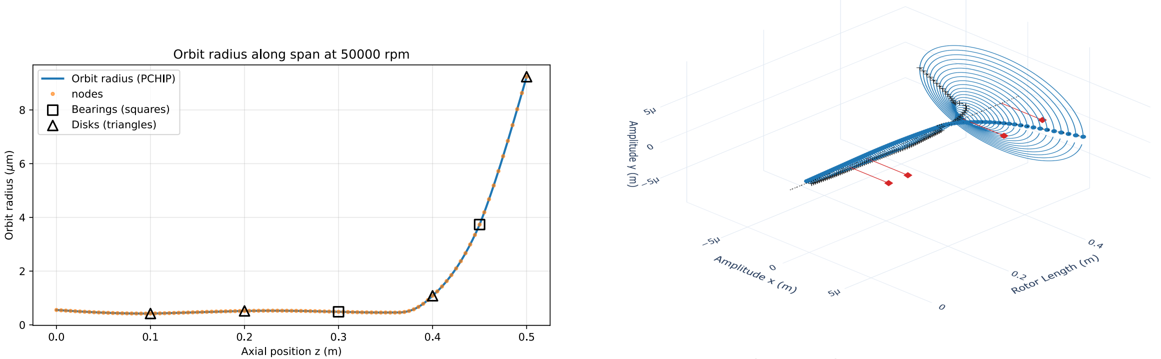

(a) Radial magnitude of the displacements [μm]

(b) 3D view of the deflected shape. The red labels are located on the disks in which the unbalance is applied.

Figure 6.10: Unbalance response for $k_{rad,1} = 2 \times 10^7 \ \frac{N}{m}$ and $k_{rad,2} = 10^8 \ \frac{N}{m}$ over the shaft's length (z-axis) at $50000 \ rpm$

On first glance, the results may appear counterintuitive, as one would expect to see a cantilever effect on the left side of the turbine bearing, similar to that observed on the right side of the pump bearing.

The discrepancy between the expected and actual results is attributed to the large asymmetries in the system. From the disks' point of view, the turbine has a mass of roughly $18 \ kg$ hanging on the left side of the bearing. The pump otherwise only has an inducer of little more than $0.5 \ kg$ hanging on the free end of the shaft.

The shaft diameter reduction amplifies this effect, making the "free-hanging" end of the shaft more than 40 times as massive as the pump end, with the associated inertia.

To verify the assumption and confirm that the unbalance response is being modeled correctly, the same methodology was applied to assess the unbalance response of a system with a more conventional layout. For that, a constant shaft diameter of $30 \ mm$ was used, with cantilever lengths of $0.3 \ m$ on the left and right sides, on which the turbine and the pump are mounted, respectively. The shaft length was also increased to $1 \ m$, to provide a spacing between the bearings of $0.4 \ m$. Finally, for symmetry purposes, the pump and the turbine were modelled with the same mass. The results are the following:

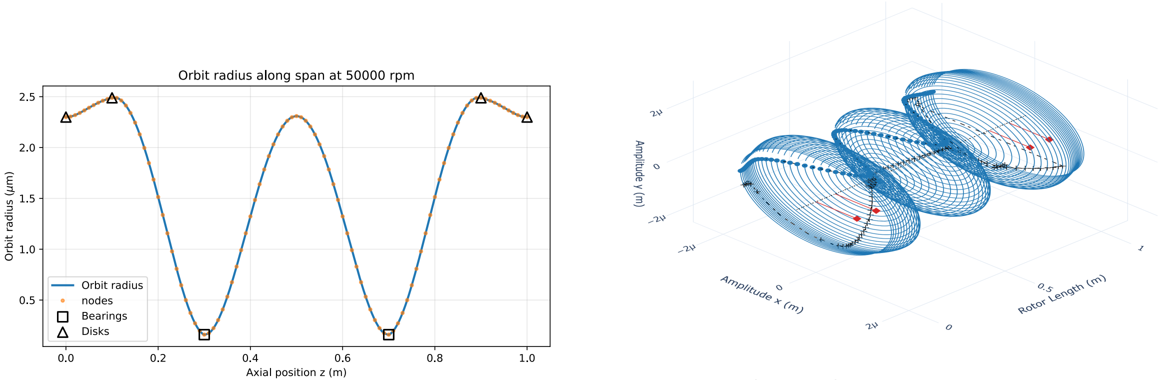

(a) Radial magnitude of the displacements [μm]

(b) 3D view of the deflected shape. The red labels are located on the disks in which the unbalance is applied.

Figure 6.11: Example of the unbalance response of a symmetric system (Non-representative displacement values)

This illustration shows the expected results, with the cantilever effect evident on both sides, more pronounced at the shaft's free ends, where inertia is lower. This validates the unbalanced model and corroborates the assumption that the non-intuitive shape of the shaft's deflections is attributed to the geometrical asymmetry of the system.

Further studies are recommended to determine whether the current configurations provide an advantage in terms of global system vibrations, or whether a configuration closer to a conventional turbopump assembly is more favourable.

The work will proceed under the assumption that the current configuration is acceptable, given the promising results for both static and dynamic contributions. The impact of the unbalance response is minimal with the current configuration at the nominal operating point, where the static contribution is the primary driver of the peak shaft deflections.

This effect can be easily noted when the results for the total displacements are plotted:

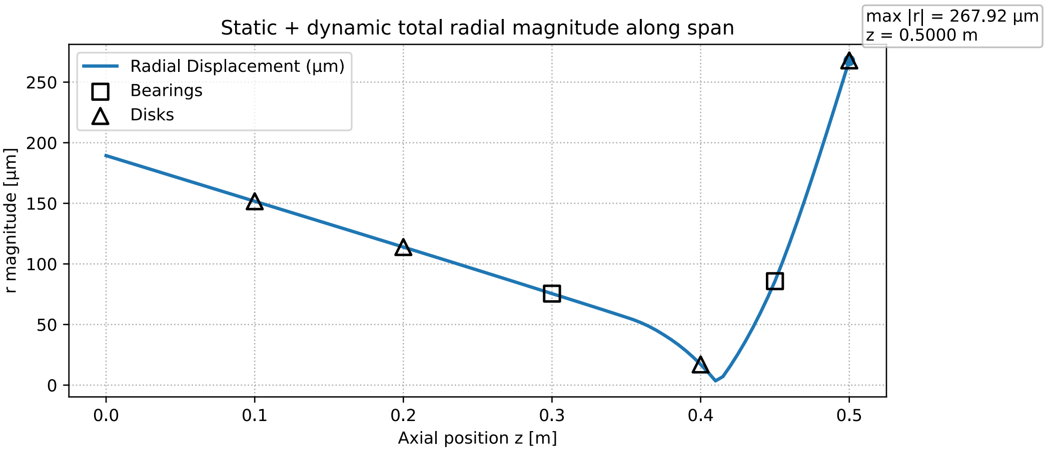

Figure 6.12: Global magnitude of the radial deflections for $k_{rad,1} = 2 \times 10^7 \ \frac{N}{m}$ and $k_{rad,2} = 10^8 \ \frac{N}{m}$ over the shaft's length, considering both static loads and the unbalance response

In which the shape of the static deflections curve is generally preserved, showing once again that it drives the deflections in nominal operation, given that it is ensured that it has sufficient margin from the system's critical frequencies through the performed stiffness tuning.

The present results demonstrate a valid bearing radial stiffness combination that complies with the critical frequency margin criteria. However, the displacement values across the entire valid range need to be assessed, and acceptance criteria need to be derived to determine whether the values are acceptable.

Acceptance Criteria

The acceptable window of bearing stiffness needs to be further constrained to take the deflections into account. This is done to ensure that the bearing parameters are chosen so the system operates safely without mechanical concerns.

In the context of turbomachines, the labyrinth seal's tip clearance is set to account for the expected deflections in the system, providing a margin between the rotor disks and the casing. The higher the clearance value, the higher the leakage flow is, as some of the gas passes through this gap, decreasing efficiency because the entire mass flow rate of gas is not used to extract mechanical energy on the shaft. Due to this decrease in efficiency, the labyrinth seal clearance values, particularly the ones used in the aerospace industry, are minimized as much as possible.

Labyrinth tip clearances are stated to be in the range of $0.25 - 0.5 \ mm$ in literature [90]. Furthermore, for the specific case of the Vulcain 2 oxidizer turbine, for which the use of abradable materials to maintain tight clearances and thus optimize efficiency is mentioned in [79]. Combining these two pieces of information, the lower end of the scale reported in [90] was taken as a reference, based on the resonance-crossing points of the use of abradable materials. This sets the static allowable deflection to $250 \ \mu m$, using the abradable material to account for transient effects.

Some preliminary studies on the displacement of resonance crossing frequencies suggested that a $250\ \mu m$ contribution from static-load displacements would yield feasible stiffness values. These initial studies also highlighted that keeping the displacements at the critical frequencies below $50\ \mu m$ would be too demanding in terms of bearing stiffness for some configurations. Therefore, the work will follow under the assumption that the maximum displacements at nominal operation are $250\ \mu m$ and $300 \mu m$ during startup when crossing the resonance points.

This follows the assumption that the abradable design of the casing can handle deflections of up to $50 \mu m$, which is corroborated by literature that mentions abradable coatings with thickness in the range of $1.016 - 1.524\ mm$, applied to aero-engine turbines with similar gas temperature requirements as this application. [91] As these values largely exceed the limit set for this application, further studies can be performed to reduce the damping requirements, if proven to be advantageous.

On the other hand, it is also essential to keep in mind that when estimating the damping requirements, the displacements on the resonance crossing frequencies are severely overestimated due to the assumption of nominal operation at these points. In reality, these points are passed through rapidly enough so they never reach the maximum amplitude.

Additional studies conducted indicated that tightening the requirement by lowering the threshold to $200 \mu m$ (and therefore bringing the upper limit of the startup displacements down to $250\ \mu m$) would not imply significant added complexity for the bearing design, as it would place the minimum stiffness requirements at 3×10^7 for the turbine bearing and 2×10^8, which are well within common values observed in literature and suppliers' catalogs. These findings leave room for fine-tuning the stiffness, in case further research provides findings regarding optimized clearance values, or specific values of abradable coating thickness, for example.

Updated Stiffness Ranges

Having set the acceptance criteria, it is now possible to further constrain the stiffness design window to account for a maximum displacement of $250\ \mu m$ due to static loads. The following figure presents the displacements as a function of the radial stiffness of the two bearings:

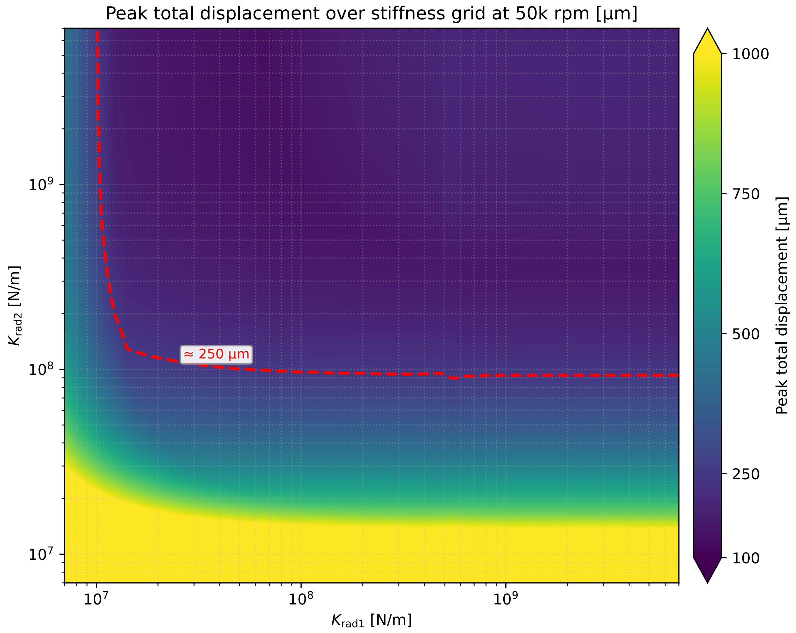

Figure 6.13: Peak displacements over the stiffness design window

Merging this result for $250 \mu m$ with the 25% margin to the closest critical frequency, the results can be translated into a stiffness acceptable range.

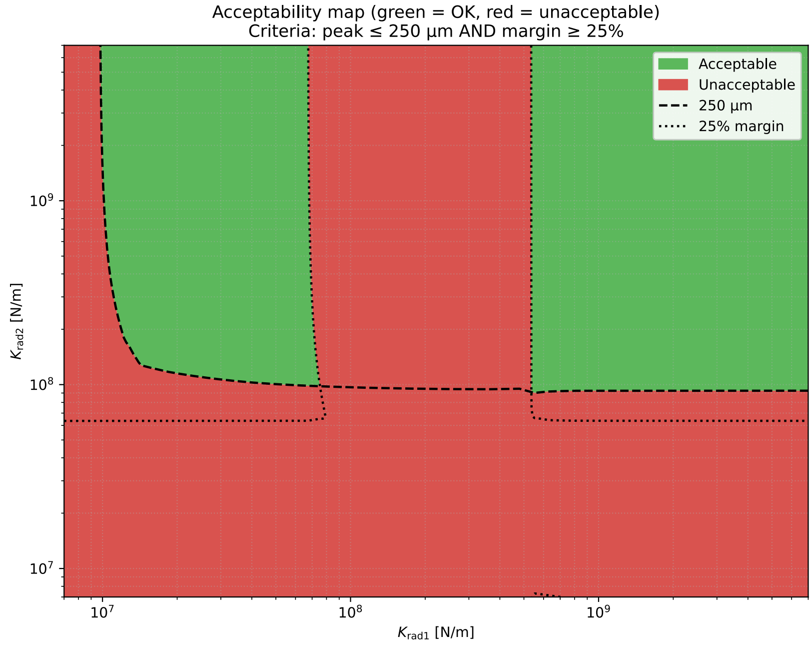

Figure 6.14: Acceptable stiffness range after applying a margin of 25% to the closest critical frequency and a maximum static displacement of $250\ \mu m$

It is visible that the current configuration of the system favors designs with a stiffer pump bearing and a less stiff turbine bearing. This comes from the high loads on the pump side, which, combined with the lower mass when compared to the turbine, lead to high displacements. The turbine benefits from having a significantly higher mass and inertia, enabling it to keep the displacements under acceptable figures with stiffness values that can be lower by roughly one order of magnitude.

The considerations following from the results of Figure 6.8 prevail, so that the design will focus on the top left green area, rather than the top right region, as the feasibility of achieving stiffness values of $10^9\ \frac{N}{m}$ is questionable, especially if bearing damping mechanisms are included.

6.3.5. Critical Frequencies and Bending Modes

Having dealt with the steady-state problem and defined the design window in terms of bearing stiffness, it is now time to handle the quasi-transient (startup) problem. In this problem, the response of the system to the residual unbalance will be assessed. The focus will be on the critical frequencies, when the shaft speed coincides with the natural frequencies of the system - the resonance-crossing amplitudes.

Up to this point, the system was considered to be undamped, apart from the damping offered by the structure. This approach was followed, given that in nominal operation, the unbalance has little impact on the system behaviour, and damping does not significantly change the displacement values. In resonance, the behaviour is completely different when the system is operating at a critical frequency (bending mode). In an undamped system, the amplitudes can reach dangerously high values, even when only considering the unbalance (forced) response component. Under these conditions, damping has a critical impact on the system, and choosing an adequate value of damping prevents the displacements from surpassing the defined threshold.

The damping method chosen for this application was the squeeze-film-damper (SFD). This essentially consists of an oil film, outside the outer ring of the bearing, against which the bearing is pushed. The viscosity properties of the oil provide a reaction force, pushing the bearing back to its original position, and therefore limiting the displacements experienced by the system.

However, using an SFD comes with a cost associated with it. Given that the bearing needs to push against the oil film, significantly more radial movement needs to be allowed when compared to the initial case in which undamped rigid bearings were used. To allow for such movement, the centering stiffness provided by the rigid coupling between the bearing and the housing of the undamped design is changed to a squirrel cage. Such components act as an elastic spring, allowing for the required radial movement so that the SFD can be used effectively, while providing some of the stiffness that was lost due to the breaking of the coupling between the bearing outer ring and the casing. A schematic of such a system is presented in the following figure, adapted from the work of Heidari et al. [92]

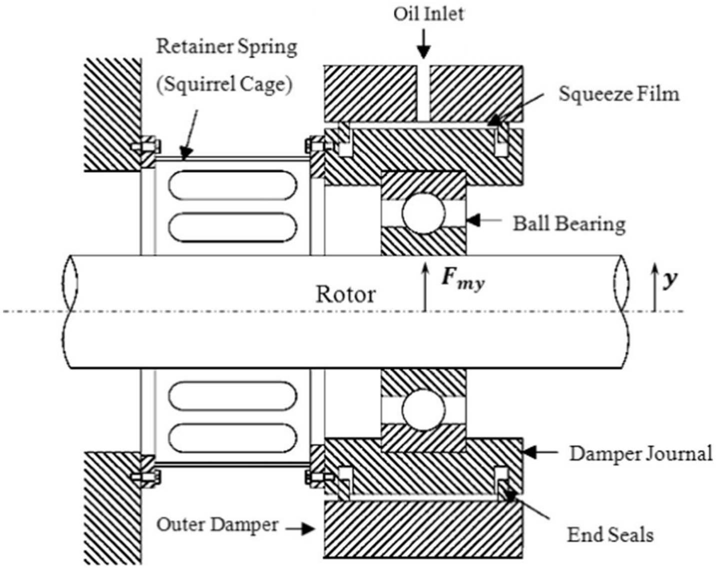

Figure 6.15: Schematic of a bearing design with squeeze film damping and squirrel cage (Adapted from the work of Heidari et al. [92])

However, and in line with the required permissible radial movement, the stiffness provided by the squirrel cage is generally lower than that for bearings with no squeeze film damper and with original bonding to the housing. The attainable stiffness values for this configuration are reported to be in the order of magnitude of $10^7\ \frac{N}{m}$, with reported values ranging from $1-4\times10^7\ \frac{N}{m}$, for aircraft engine applications. [93]

These values can be compared with the commonly reported figures for bearing stiffness in suppliers' catalogues [84] at an order of magnitude of $10^8\ \frac{N}{m}$. This results in a stiffness penalty of roughly one order of magnitude when using a squirrel cage, compared to the initial bearing stiffness.

Therefore, given the current distribution of stiffness requirements among the two bearings for this application, it is possible that the SFD and associated squirrel cage can only be applied to the turbine bearing. This comes since the pump bearing stiffness requirements are in the order of magnitude of $10^8\ \frac{N}{m}$, which may be unattainable with a squirrel cage design.

To address this potential problem, two separate studies will be conducted. In the first case, both bearings will be assumed to have the same damping properties, provided an SFD design is feasible and meets the stiffness requirements of both bearings. For the second case, a more conservative approach will be followed, for which only the turbine bearing will be assumed to have an SFD, having a traditional undamped bearing for the pump bearing. The damping requirements coming from these analyses will allow us to determine the feasibility of both configurations.

To perform such an analysis, the same methodology as the nominal operation case was followed. The residual unbalance forces on each turbine rotor disk, the inducer, and the impeller have been modelled in ROSS as an excitation, and the unbalance response function was called to return the deflections.

Given the high uncertainty regarding system startup, the extreme case in which the system operates nominally at its critical frequencies is analyzed. In reality, these are precisely the points that need to be avoided and passed through quickly enough during startup to prevent dangerous deflection amplitudes from occurring. However, to define the ceiling of the damping requirements, simulating steady-state operation at the critical frequencies enables this.

To perform an assessment of the system's behaviour, some representative values for damping and stiffness have been chosen, and some other assumptions have been made:

- $k_{rad,1} = 1.5 \times 10^7 \frac{N}{m}$ and $k_{rad,2} = 1.4 \times 10^8 \frac{N}{m}$- using the lower end of the acceptable stiffness interval, which is on top of the maximum allowed static deflection of $250\ \mu m$
- $k_{xx} = k_{yy} = k_{rad}$ - assuming that the bearing is isotropic
- Both bearing arrangements have the same stiffness properties and damping properties offered by the squeeze film damper - first configuration.
- The damping properties of the squeeze film dampers of both bearings are identical and isotropic.
- The residual unbalance forces are in phase

For such parameters, the natural frequencies of the system corresponding to the first, second, and third forward bending modes occur at the speeds of $2833\ rpm$, $22788\ rpm$, and $62659\ rpm$, respectively. The system is supercritical with respect to the first two bending modes, and subcritical with respect to the third. In practical terms, the third critical frequency, being well above the maximum rpm of the system, would never be reached. However, to keep the results general and prepare for system designs for which the bearing stiffness may be lower, the displacements at this critical frequency will still be assessed.

The corresponding peak total displacements are presented, as a function of the radial damping, in the following figures:

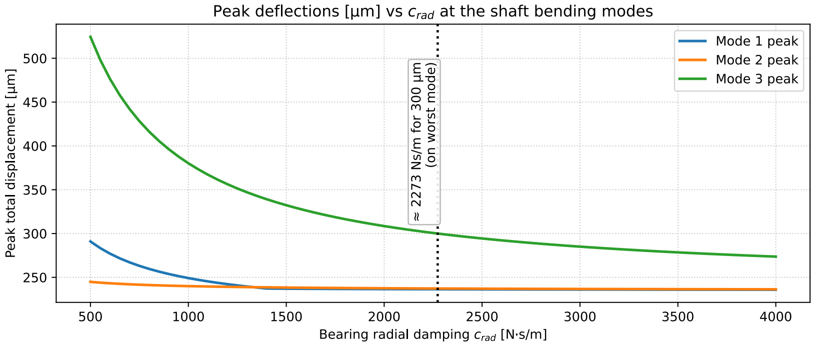

Figure 6.16: Damping requirement to keep the system's maximum displacement at critical frequencies under $300\ \mu m$ with a squeeze film damper applied on both bearings

If all modes are considered, and both bearings have the same damping properties, the required damping to keep the total displacements at all critical frequencies under $300\ \mu m$ is $2273\ \frac{Ns}{m}$. While this value is feasible, it is still of interest to assess the behaviour in case the third bending mode, which is well above the system's maximum rotational speed, is not considered. The requirements are expected to become much lower. As shown in Figure 6.17, the first and second bending modes lead to significantly lower displacements. The updated requirements, as well as the behaviour for the first and second bending modes, can be observed in the following figure:

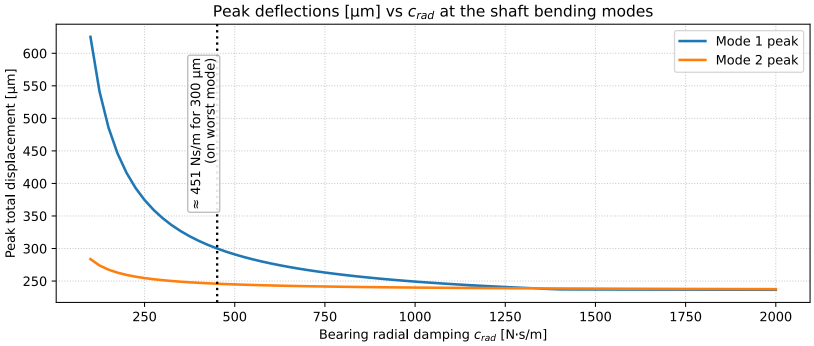

Figure 6.17: Damping requirement to keep the system's maximum displacement at the critical frequencies corresponding to the first two forward bending modes under $300\ \mu m$ with a squeeze film damper applied on both bearings

This results in a significant reduction in damping requirements, with the minimum damping value at just $451\ \frac{Ns}{m}$. It is also noticeable that, as expected, as damping rises, the displacements converge to the value of the static displacement for the used stiffness combination. Given that for this analysis, the value used was the lowest stiffness combination that complies with the displacement requirements, the system converges to a peak displacement value of $250\ \mu m$ for higher values of damping.

As previously introduced, the use of a squirrel cage effectively imposes a "penalty" on stiffness. The reported values in the literature for bearings with squirrel-cage design integrated for squeeze film dampers are more aligned with the order of magnitude of the turbine bearing's stiffness than with that of the pump bearing. Therefore, the results from the same study, but with damping applied only to the turbine bearing, can also be useful as input for future designs. An initial analysis indicated that such a design would be unfeasible if the third bending mode is considered. Therefore, the following results present the damping requirements for the case in which only the turbine bearing has an SFD, and only for bending modes under $50000\ rpm$, corresponding to the first and second bending modes.

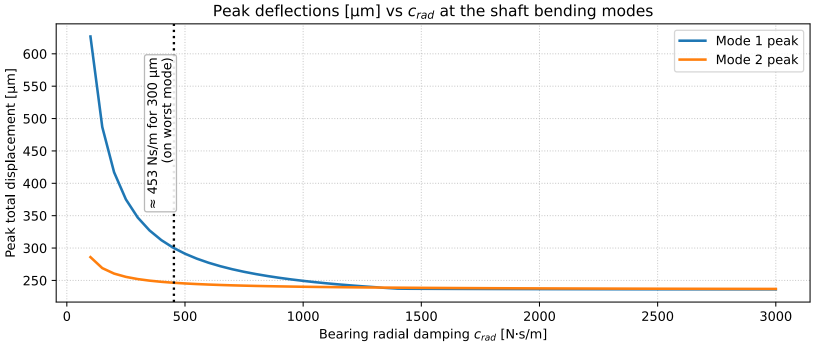

Figure 6.18: Damping requirement to keep the system's maximum displacement at critical frequencies under $300\ \mu m$ with a squeeze film damper only applied on the turbine bearing

The difference in damping requirements when only the turbine bearing is damped is almost negligible. These results may sound surprising, but are explained by the shape of the bending modes at $2833\ rpm$ and $22788\ rpm$. The values were plotted for a damping of $100\ \frac{Ns}{m}$ per bearing, so that the resonance effects remain noticeable.

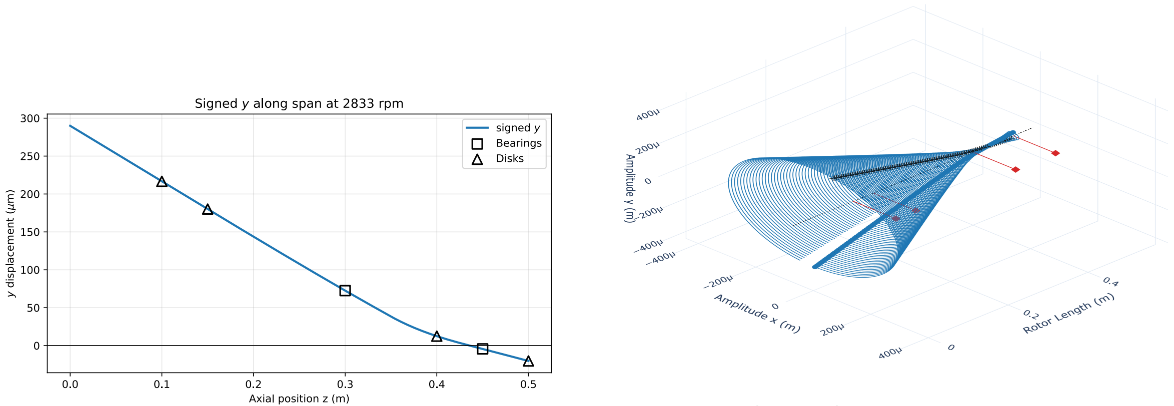

(a) Displacements magnitude $[\mu m]$

(b) 3D view of the deflected shape. The red labels are located on the disks in which the unbalance is applied.

Figure 6.19: Radial displacements over the axial length of the shaft on the first critical frequency

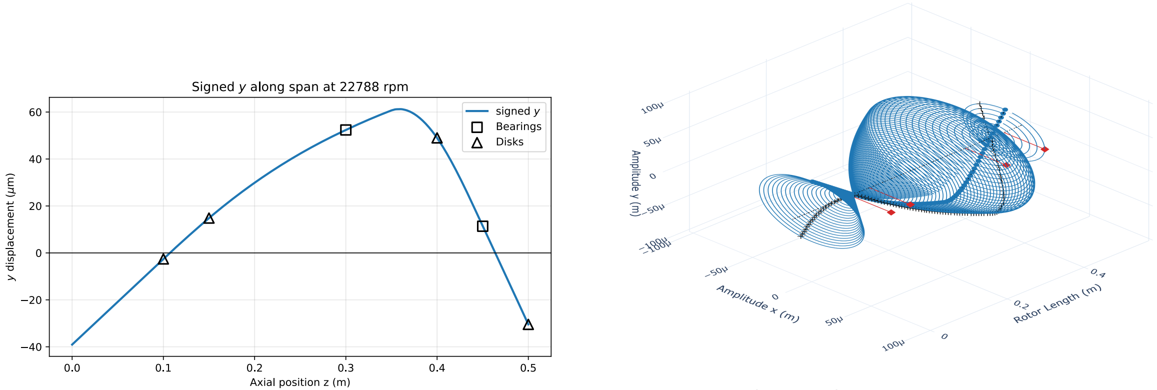

(a) Displacements magnitude $[\mu m]$

(b) 3D view of the deflected shape. The red labels are located on the disks in which the unbalance is applied.

Figure 6.20: Radial displacements over the axial length of the shaft on the second critical frequency

As can be noted, the location of the second bearing is a node on both these frequencies, and its displacement is close to zero. Therefore, its properties have little impact on the system's behaviour, and its damping value is not critical for the system's displacements.

This proves the feasibility of operating with an SFD on the turbine bearing, provided the third bending mode is never excited, which is the case within the current acceptable stiffness window. Regarding the required damping, the values are within the state of the art, as values of $3.9\ \frac{kNs}{m}$ have been reported in the literature and are well above the requirements of this application. [94]

6.3.6. Unbalance Phase Impact

All the studies performed up to now have followed an assumption that, in reality, is hardly verified. The assumption was that all rotor unbalance forces were in phase. In a real application, there is a phase gap between the rotor's unbalance, which is unknown during operation.

Therefore, the case with the largest displacements needs to be considered to define the damping requirements.

Due to the system configuration, it is clear that, on the turbine side, both unbalances being in phase represent the worst-case scenario. For the pump, otherwise, this is less clear, as the bearing is placed between the inducer and the impeller. Therefore, the study is made around these two disks, by fixing the unbalance phase of the inducer at 0, while varying the inducer unbalance in the $[0, 2\pi]$ range and observing the evolution of the displacements. The results are presented in the following figure:

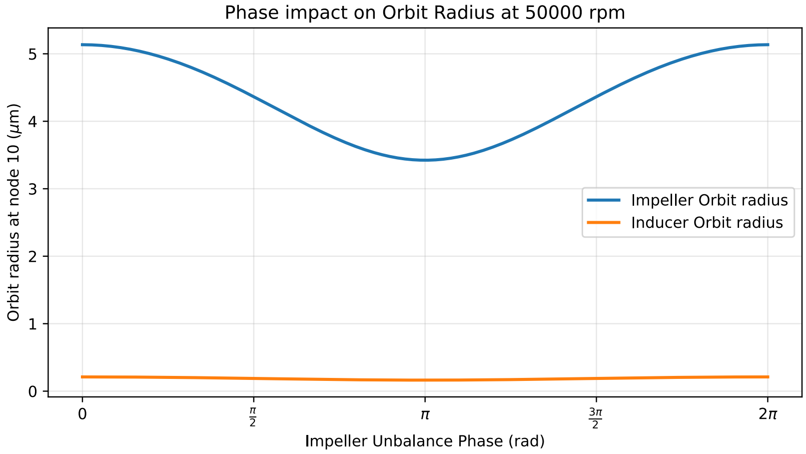

Figure 6.21: Radial displacements on the inducer and impeller as a function of the impeller's unbalance phase

From the results, it is possible to conclude that the case with the largest displacements at both locations occurs when the two unbalance contributions on the pump side are in phase. As expected, across the entire envelope, the displacements at the impeller location are much higher than those at the inducer, as its location near the two bearings strongly constrains its movement. Nevertheless, and despite being hard to notice from the plot, it follows the same trend as the impeller displacement, being minimum when the unbalances are in opposite directions, with a phase offset of π or 180 degrees.

These findings confirm that the previously computed results are the most conservative ones, and therefore suppress the need to update the damping and stiffness requirements to account for the unbalance phase impact.

6.3.7. Bearing Lubrication Requirements

The only missing requirement of the facility regarding rotordynamics within the scope of this study is the bearing lubrication requirements.

To perform such a study, a dedicated bearing design tool provided by ArianeGroup was used to estimate the power dissipation on each bearing. The inputs used were the ones for the closest match with the $d_m N$ and load rating requirements found on the SKF website. The following models were used:

- Turbine Bearing - SKF 7014 CEGA/HCP4A [95]- coming as partially compliant with the requirements due to a lower speed rating than the required for this application. However, it is assumed that the bearing parameters are still representative for a rough estimation of the power dissipation, which is the purpose of this study.
- Pump Bearing - SKF 7006 CE/P4A [88] - which is fully compliant with the requirements, with the note that, as previously mentioned, the load ratings offer a safety factor that may be too small, depending on the outcome of further studies.

Both supports are considered double bearings with a back-to-back arrangement to provide axial load ratings in both directions. The software was found to be increasingly complex when dealing with lubricated bearings and to require input parameters for which there are high uncertainties at this stage. Therefore, for the scope of this research, the bearings were modelled as unlubricated, yielding a result that represents the upper limit of friction values and, consequently, the upper limit of dissipated power.

Given that the purpose of this research is to determine the upper limit of lubrication requirements, this figure remains useful despite its limitations.

The results can be observed in the following table:

Table 6.8: Bearing Power Dissipation for the turbine and pump bearings at peak operating conditions ($50000\ rpm$)

Bearing Designation	P_{diss} $[kW]$
#1 (Turbine Bearing)	3.45
#2 (Pump Bearing)	1.17

Considering a lubrication system using an oil-air heat exchanger, the API 610 Standard [96] from the American Petroleum Institute limits the oil temperature rise on the bearings to $28\ K$ for pressurized systems. By performing a simple energy balance, the required mass flow rate of oil $\dot{m}_{oil}$ can be directly related to the dissipated power as:

$$P_{diss} = \dot{m}_{oil} c_{p,oil} \Delta T \tag{6.42}$$

Which for the maximum ΔT of $28\ K$ becomes:

$$\dot{m}_{oil} = \frac{P_{diss}}{28\ c_{p,oil}} \tag{6.43}$$

The same standard also states that bearing metal temperatures shall not exceed $93°C$ for such systems. [96]. Therefore, assuming the temperature rise occurs from $65°C$ to $93°C$, the average c_p for motor oil at such temperatures is roughly $2.1\frac{kJ}{kg \cdot K}$, and the average density is $825\ \frac{kg}{m^3}$, interpolating the values provided by Atlantic Heat Transfer Oils for low viscosity oils.[97]. Having figures for these values, the required mass flow rate of oil in g/s and the volumetric flow rate in l/min (liters per minute).

per bearing is presented in the following table:

Table 6.9: Oil mass flow rate requirements for the system bearings at peak operating conditions (50,000 rpm)

Bearing Designation	$\dot{m}_{\mathrm{oil}}\,[\mathrm{g\,s^{-1}}]$	$Q_{\mathrm{oil}}\,[\mathrm{L\,min^{-1}}]$
#1 (Turbine Bearing)	58.7	4.27
#2 (Pump Bearing)	19.9	1.45
Total	**78.6**	**5.72**

A figure of $5.72\ l/min$ does not represent extreme requirements for the base infrastructure, as it is well within the per-line capabilities of SKF oil distribution systems [98]. These results confirm the feasibility of using such bearings with respect to their lubrication system.

6.3.8. Bearing Lifetime

The analysis performed with RMS5 also yielded some interesting figures on bearing lifetime. The values are expressed as fatigue limits L_{10h}, defined as the time, in operating hours, after which 10% of such bearings are expected to fail. The values are presented in the following table:

Table 6.10: Oil mass flow rate requirements for the system bearings at peak operating conditions (50,000 rpm)

Bearing Designation	**Bearing Expected Lifetime** L_{10h} $[\mathrm{h}]$
#1 (Turbine Bearing)	186.0
#2 (Pump Bearing)	4.59

It can be noted that neither value raises relevant concerns, given that their lifetimes are several orders of magnitude longer than the test duration of such machines. Nevertheless, it is still advisable that, especially for the pump side, the bearings are replaced after each test campaign.

The significant differences are attributed to the turbine bearing being subject to significantly lower loads than the pump. Furthermore, it benefits from a larger number and diameter of balls (25 vs. 17 in the pump bearing) due to the larger design, further splitting the loads. It is expected that the results will improve with lubrication, as this analysis was conducted under the assumption of unlubricated bearings for simplicity.

Although the values are not concerning, it is recommended that special attention be paid to the pump bearing in future work. It is anticipated that a model better suited to this application, specifically to the loads experienced, can deliver significant improvements regarding its expected lifetime, given that the current safety factors are relatively low.

7

Conclusion

This work assessed the feasibility of the design of a flexible test facility to test turbines under representative conditions. The work was performed with very limited input, given the scarcity of public data and prior studies on this subject. In the context of this facility, flexibility means accommodating different turbine stages and operating points within the $30000–50000\ rpm$ envelope without significant hardware changes, enabled by a modular power dissipation path and bearing/damping supports that provide high margins (in the order of 25%) to the nominal operating point.

Given the uncertainty inherent to this preliminary design stage, the studies were performed parametrically and included repeated extreme-case analyses. As a consequence, most derived requirements are expressed as upper bounds, reflecting a conservative approach. The intention behind adopting these upper bounds is to provide clarity for future, more detailed studies that can complete the design by further constraining the operational requirements.

Despite the limitations, the work supports the feasibility of such a design, using a theory-anchored scaling methodology as the backbone of the subsystem design and of the derivation of operational requirements. Relative to the initial objectives of assessing feasibility, down-selecting a power-dissipation concept, and deriving rotor–bearing requirements, the results meet the intended outcomes at this stage. The main findings of the work provide a direct answer to the research questions and are summarized as follows:

- It is possible to achieve representative tests at TRL6 while operating at a reduced power output. This is achieved by testing at reduced pressures and fixing the following non-dimensional parameters: specific speed (N_s), specific diameter (D_s), and spouting velocity Mach number (M_{c_0}).
- Dissipating $3\ MW$ of power is feasible with a modular water pump design with an inducer and an impeller. Both components operate at a mass flow rate of $100\ kg/s$, achieving a total pressure rise (Δp_t) of $210\ bar$. Water must be supplied at no less than $13.9\ bar$ to avoid cavitation.
- It is feasible to support the turbine's shaft while allowing it to operate in the $3000\ rpm$ to $50000\ rpm$ range without the risk of running into resonance. This is attained using a turbine bearing whose stiffness is within the $10^7\ \frac{N}{m}$ to $8\times10^7\ \frac{N}{m}$ range, and a pump bearing whose stiffness exceeds $10^8\ \frac{N}{m}$. Avoiding the displacements at the resonance crossing points from exceeding the $300\ \mu m$ threshold is possible, even if only the turbine bearing is damped, with a minimum required damping of $453\ \frac{Ns}{m}$.

From a system-level perspective, these results allow us to answer the main research question RQ1: “What is the general configuration of a multi-MW turbine test facility?” The facility layout that emerges from this work follows the baseline configuration formulated in the Hypothesis section (subsection 2.3.4): a propellant storage and enthalpy-generation system feeding a turbine mounted on a direct-drive shaft line with a modular shaft-support subsystem and a multi-megawatt water-pump power dissipation mechanism, complemented by exhaust handling, cooling, lubrication, and data-acquisition and control systems sized for the $3\ \mathrm{MW}$ and $30000–50000\ \mathrm{rpm}$ operating envelope.

The scope focused on the two largest drivers of complexity, which are also the main levers for modularity and flexibility: power dissipation and shaft-supporting mechanisms.

For the required power dissipation, different options were surveyed, and their advantages and disadvantages outlined. An engineering trade-off, informed by a Pareto-based Analytic Hierarchy Process, was used to structure the decision in the context of this facility. Although no single optimal solution emerged, the analysis provided decision support that informed discussion within the engineering team. With the available information, a self-designed water pump is favoured for this test facility. This option offers significant technical advantages, sits mid-range in cost among the studied alternatives, and can benefit from design choices that further reduce cost while building in-house knowledge. A further advantage is that it does not require a gearbox, which significantly simplifies rotordynamics.

Rotordynamics followed logically in this project's workflow. The objective was to derive requirements for the shaft support system. The focus was on bearings, dampers, and geometric considerations, given their critical impact on flexibility across wide operating domains. A preliminary design capable of operating in the range of 30000 to $50000\ rpm$ was achieved. This design specifies a proposed geometry, the components used and their locations along the shaft, and the corresponding load ratings, stiffness, and damping requirements for the bearings. These values were obtained under extreme conditions and should be treated as upper bounds that can be reduced as uncertainties are mitigated.

To finalize the assessment of this subsystem, potential bearing candidates were identified from supplier catalogues. Using a bearing design tool, the power dissipated in the bearings was estimated, which, in turn, set upper bounds for the cooling and lubrication mass flow rates. The same tool provided indicative bearing lifetime considerations, leading to the conclusion that further investigation of the pump-side bearing is necessary to ensure compliance with the facility's operating conditions.

Globally, this research presents a baseline for the development of a test facility that combines flexibility with an unprecedented level of representativeness at turbine-level testing, meeting the requirements for TRL6 test conditions. The facility concept accommodates direct-drive operation without the need for a gearbox or other startup auxiliary mechanisms, and it supports an operating range consistent with current hydrogen–oxygen turbine technology, with cooling and lubrication flows sized based on bearing losses.

Although this work does not present a complete, detailed design, which is something unfeasible within the project timeline, it consolidates the key design aspects of the critical subsystems and components. The research should be followed by studies that increase the level of detail, reduce uncertainty, mature the water pump concept and cost, verify bearing lifetime on the pump side, and validate the integrated rotor–bearing system, ultimately leading to a higher design maturity and culminating in the construction of the facility. These steps will convert ceiling requirements into verified design values and provide the evidence base that closes the loop from feasibility to construction.

8

Recommendations for Future Work

As extensively mentioned throughout this report, the most useful product of this research is the clarity it may provide for future work. Therefore, a summary of the proposed actions to be addressed in future research, taking the findings of this work as inputs, follows.

The action points are divided into four sections, following the logic of this report: scaling, the general layout and feed system, power dissipation, and rotordynamics.

8.1. Scaling

The proposed work aims to better understand the effects of the proposed scaling methodology on the phenomena observed during operation. The following action points are proposed:

- Performing parametric CFD simulations to understand the impact of the reduced operating parameters on the flow phenomena. With that, define further constraints on the scaling, namely the boundaries for staged combustion scaling.
- Collecting a larger database of turbines so that the operating requirements can be derived with a higher level of accuracy. This determined whether the system requirements needed to be increased to more ambitious figures, and whether the project's feasibility required to be reassessed, or whether they could be relaxed, demonstrating cost savings and reduced operational complexity.

8.2. General Layout and Feed System

Regarding these subsystems, the work shall focus on further detailing the components needed for the feeding lines and enthalpy generation systems, identifying critical design points.

- Identifying the valves and feeding lines needed for the system's operation and their operating conditions. With this information, the feasibility of using standard components shall be assessed, and candidate models shall be identified.
- Performing a test campaign and an eventual injector redesign to characterize a HydroLOx gas generator at pressures in the order of $20\ bar$, to suppress the lack of existing equipment rated to operate at this range.

8.3. Power Dissipation

The proposed work on the power dissipation mechanism falls into two categories: the characterization of the options and the feasibility of their design.

- Contacting suppliers to obtain more precise base infrastructure requirements and cost figures, which allow for a more anchored trade-off process.

- Performing a more detailed design of the water pump, to have a full understanding of its capabilities and required base infrastructure.
- Performing a detailed cost estimation for the water pump, making an impact study on the different drivers for the cost, and optimizing to achieve an inexpensive solution. As the pump is not designed for flight, there is significant potential to reduce the cost and make it a more attractive solution.
- Promoting further discussion regarding the criteria weights and option scores in the Analytic Hierarchy Process. Preferably, this should be done through a detailed analysis by the turbine manufacturer to achieve more precise figures for the projected evolution of operating requirements.
- If, after the uncertainties in the trade-off are mitigated, the pump is still seen as the most advantageous solution for this application, perform a test campaign to characterize its loads and power curve. These parameters are crucial for determining bearing requirements and for providing accurate power and torque measurements during turbine testing.

8.4. Pillow Block Design and Rotordynamics

For this section, the recommendations are based on further determining the feasibility of the current subsystem requirements, reducing the uncertainty of the load estimations, and assessing other options for components and system configuration. The following action points are left as suggestions:

- With a larger and more complete turbine database, reassess the upper limits for the loads experienced during operation. Suppose transient behaviour is well-characterized on both the turbine and pump sides. In that case, it is possible to determine the time at which the resultant loads acting on the system take their maximum value. With this information, it is possible to reduce the bearing requirements and reassess whether standard components can fully meet them.
- Surveying the feasibility of slightly reducing the rotational speed requirements and the shaft diameter. A slight adjustment of those parameters may yield significant cost savings, as the $d_m N$ values of such bearings fall within the standard part capabilities if these requirements are reduced by roughly 10%.
- Contacting suppliers regarding the findings of this work in terms of bearing requirements. With that, assess the feasibility of standard parts or custom-made designs, and iterate upon the system's geometry accordingly.
- Using more detailed bearing specifications provided by the suppliers, it is valuable to reassess rotordynamics to determine whether changes to the system are needed to ensure the bearing is suited to the application.
- Performing an impact study on different system configurations (bearings and dampers location) to understand the available trade-offs and to better understand which is the most advantageous solution for this application.
- Analyzing other damping options, such as journal damping, to provide support for an informed decision on whether the usage of a squeeze film damper and a squirrel cage is the optimal solution for this application.

References

[1] D. Coulon. "Vulcain-2 Cryogenic Engine Passes First Test with New Nozzle Extension". In: *ESA Bulletin* 102 (May 2000), pp. 123–124. URL: `https://www.esa.int/esapub/bulletin/bullet102/Coulon102.pdf`.

[2] M Héder. "From NASA to EU: the evolution of the TRL scale in Public Sector Innovation". In: *The Innovation Journal* 22.2 (2017), pp. 1–23.

[3] European Space Agency. *Technology Readiness Levels (TRL)*. Enabling & Support → Space Engineering & Technology → Shaping the Future. n.d. URL: `https://www.esa.int/Enabling_Support/Space_Engineering_Technology/Shaping_the_Future/Technology_Readiness_Levels_TRL` (visited on 02/04/2025).

[4] J.C. Mankins et al. *Technology readiness levels*. 1995.

[5] Wayne J Bordelon Jr, William J Kauffman Jr, and John P Heaman. "The Marshall Space Flight Center Turbine Test Equipment: Description and Performance". In: *Turbo Expo: Power for Land, Sea, and Air*. Vol. 78927. American Society of Mechanical Engineers. 1993, V03CT17A041.

[6] A.J. Head et al. "Preliminary design of the ORCHID: a facility for studying non-ideal compressible fluid dynamics and testing ORC expanders". In: *Turbo Expo: Power for Land, Sea, and Air*. Vol. 49743. American Society of Mechanical Engineers. 2016, V003T25A001.

[7] T Traudt et al. "An overview on the turbopump roadmap for the LUMEN demonstrator engine and on the new turbine test facility". In: *Proc. Int. Astronaut. Congr. IAC* 13 (2017), pp. 8513–8517.

[8] T Traudt et al. "LUMEN: Test Platform for Rocket Engine Technologies. Project Overview and Upcoming Steps in the Development". In: *34th International Symposium on Space Technology and Science ISTS*. 2023.

[9] D Ehrlich and J Schwille. "A water test facility for liquid rocket engine turbopump cavitation testing". In: (2009).

[10] E Rapposelli et al. "A new cavitation test facility at centrospazio". In: *4th International Conference on Launcher Technology*. 2002, pp. 3–6.

[11] C Schiewe, Nicolas Neuburger, and Stephan Staudacher. "How future propulsion systems influence future component testing: Latest results from Stuttgart University's altitude test facility". In: *Proceedings of the Global Power and Propulsion Society Technical Conference, Zurich, Switzerland*. 2019, pp. 15–16.

[12] K-J Schmidt et al. "Adaptation of the stuttgart university altitude test facility for BR700 core demonstrator engine tests". In: *Turbo Expo: Power for Land, Sea, and Air*. Vol. 78637. American Society of Mechanical Engineers. 1998, V002T02A016.

[13] F Kost and P-A Giess. "Experimental turbine research at DLR Goettingen". In: *Journal of the Gas Turbine Society of Japan* 32.6 (2004), pp. 47–56.

[14] AH Epstein, GR Guenette, and RJG Norton. *The MIT blowdown turbine facility*. Vol. 79498. American Society of Mechanical Engineers, 1984.

[15] A.H. Epstein, Gerald Roger Guenette, and Robert JG Norton. *Design of the MIT Breakdown Turbine Facility*. Tech. rep. Cambridge, Mass.: Gas Turbine Laboratory, Massachusetts Institute of …, 1985.

[16] H. Lee et al. "Turbine performance experiments for the turbopump of a liquid rocket engine". In: *International Journal of Aerospace System Engineering* 3.1 (2016), pp. 25–29.

[17] L Byeung-Jun and Hong Chang-Uk. "Air Similarity Performance Test of Turbopump Turbine". In: *Journal of the Korean Society of Propulsion Engineers* 10.2 (2006), pp. 39–45.

[18] EREA — European Research Establishments in Aeronautics. *High-Speed Rotating Turbine Rig CT-3*. EREA Catalogue — Technology Infrastructures. n.d. URL: `https://erea.org/catalogue/listing/high-speed-rotating-turbine-rig-ct-3/` (visited on 11/02/2025).

[19] D Visconti. “Efficiency of a high-speed low pressure turbine measured in an intermittent short-duration facility”. In: (2022).

[20] H Ellerbrock and Stefan Ziegenhagen. “Liquid rocket engine test facility engineering challenges”. In: *Acta Astronautica* 59.12 (2006), pp. 1123–1134.

[21] K Kamijo, E Sogame, and A Okayasu. “Development of liquid oxygen and hydrogen turbopumps for the le-5 rocket engine”. In: *Journal of Spacecraft and Rockets* 19.3 (1982), pp. 226–231.

[22] O.S Vaidya and Sushil Kumar. “Analytic hierarchy process: An overview of applications”. In: *European Journal of operational research* 169.1 (2006), pp. 1–29.

[23] OE Balje. “A study on design criteria and matching of turbomachines: Part a—similarity relations and design criteria of turbines”. In: (1962).

[24] L Souverein et al. “On the effect of axial turbine rotor blade design on efficiency: a parametric study of the Baljé-diagram”. In: *7th European conference for aeronautics and space sciences(EUCASS). doi: http://doi. org/10.13009/EUCASS2017-241*. 2017.

[25] QuasarMaster. *Gas generator rocket engine cycle*. `https://commons.wikimedia.org/wiki/File:Gas_generator_rocket_engine_cycle.svg`. Diagram of a gas generator cycle (rocket engine). Licensed under CC BY-SA 4.0. Accessed: 2025-12-01. 2025.

[26] S Trollheden et al. “Development of the turbines for the Vulcain 2 turbopumps”. In: *35th Joint Propulsion Conference and Exhibit*. 1999, p. 2342.

[27] Duk. *Staged combustion rocket thermodynamic cycle*. `https://commons.wikimedia.org/wiki/File:Staged_combustion_rocket_cycle.svg`. Diagram of a staged combustion rocket engine cycle. Licensed under the GNU Free Documentation License 1.2 and Creative Commons BY-SA 3.0. Accessed: 2025-12-01. 2005.

[28] T. Mizuno and colleagues. “Development of Turbopump for LE-9 Engine”. In: *IHI Engineering Review* 51.2 (2018), pp. 41–47. URL: `https://www.ihi.co.jp/en/technology/techinfo/contents_no/__icsFiles/afieldfile/2023/06/17/e149819e77e8ce8aa1b497fbbb05a107.pdf`.

[29] S. Eury, J. Gastal, and J. Borromée. “Development Status of the Vulcain Engine”. In: *26th AIAA/ASME/SAE/ASEE Joint Propulsion Conference*. AIAA 1990-2251. 1990. DOI: `10.2514/6.1990-2251`.

[30] A. Iffly and M. Brixhe. “Performance Model of the Vulcain Ariane 5 Main Engine”. In: *35th AIAA/ASME/SAE/ASEE Joint Propulsion Conference*. AIAA 1999-2472. 1999. DOI: `10.2514/6.1999-2472`.

[31] U. Wåhlen. “The Aerodynamic Design of the Turbines for the Vulcain Rocket Engines”. In: *31st AIAA/ASME/SAE/ASEE Joint Propulsion Conference*. AIAA 1995-2536. 1995. DOI: `10.2514/6.1995-2536`.

[32] J. Barton, C. Goulpeau, and P. Jorant. “The Vulcain Mk2 Engine for Ariane 5 Evolution”. In: *31st AIAA/ASME/SAE/ASEE Joint Propulsion Conference*. AIAA 1995-2535. 1995. DOI: `10.2514/6.1995-2535`.

[33] R. Bosson, P. Sabin, and G. Turin. “Improvements of the Hydrogen Turbopump for the Vulcain 2 Engine”. In: *35th AIAA/ASME/SAE/ASEE Joint Propulsion Conference*. AIAA 1999-2344. 1999. DOI: `10.2514/6.1999-2344`.

[34] S. Andersson, M. Lindeblad, and U. Wåhlen. “Performance Test Results for the Vulcain 2 Supersonic/Transonic Hydrogen Turbine”. In: *34th AIAA/ASME/SAE/ASEE Joint Propulsion Conference*. AIAA 1998-3999. 1998. DOI: `10.2514/6.1998-3999`.

[35] S. Trollheden et al. “Development of the Turbines for the Vulcain 2 Turbopumps”. In: *35th AIAA/ASME/SAE/ASEE Joint Propulsion Conference*. AIAA 1999-2342. 1999. DOI: `10.2514/6.1999-2342`.

[36] K Kamijo et al. “Developmental History of Liquid Oxygen Turbopumps for the LE-7 Engine”. In: *Transactions of the Japan Society for Aeronautical and Space Sciences* 44.145 (2001), pp. 155–163. URL: `https://www.jstage.jst.go.jp/article/tjsass/44/145/44_145_155/_pdf`.

[37] D. Watanabe and colleagues. “Combustion Stability Improvement of the LE-9 Engine for the H-III Launch Vehicle”. In: *Mitsubishi Heavy Industries Technical Review* 53.4 (2016), pp. 28–33. URL: `https://www.mhi.com/technology/review/sites/g/files/jwhtju2326/files/tr/pdf/e534/e534028.pdf`.

[38] Bonnie J. McBride and Sanford Gordon. *Computer Program for Calculation of Complex Chemical Equilibrium Compositions and Applications. Part II: Users Manual and Program Description*. NASA Reference Publication NASA RP-1311, Part II. Chemical Equilibrium with Applications (CEA). Cleveland, OH: NASA Lewis Research Center, June 1996. URL: `https://ntrs.nasa.gov/citations/19960044559`.

[39] S Soller et al. “Characterisation of a lox-lch4 gas generator”. In: *Space Propulsion Conference*. Vol. 2014. 2014.

[40] NN Narayan Rao. “The basic theory of hydraulic dynamometers and retarders”. In: *SAE Transactions* (1968), pp. 650–667.

[41] *H3606 Engine Dynamometer*. H3606. Power Test - Taylor Dynamometer. Aug. 2025.

[42] B Knight. “Understanding inertia ratio and its effect on machine performance”. In: *Mitsubishi Electric, White Paper.[Online]. Available* (2015).

[43] *Dokumentacija za nadmetanje: CAPAX — Smart Marine Engineering (KK.03.2.1.05.0035-N02), Izmjena 1*. Capax d.o.o. Nov. 2, 2017. URL: `https://arhiva.strukturnifondovi.hr/wp-content/uploads/2017/12/04_DZN___CAPAX_SME_N02___izmjena_1_02.11.2017.pdf` (visited on 10/03/2025).

[44] *Dynamometer — Contract Award N6660424P0039*. U.S. Navy, Naval Undersea Warfare Center Division Newport. Dec. 19, 2023. URL: `https://sam.gov/opp/2dcfda1f6bf34f79b7443f450ad82b68/view` (visited on 10/03/2025).

[45] *2MW 30krpm Dynamometer Test Stand*. University of Nottingham. Dec. 4, 2020. URL: `https://www.contractsfinder.service.gov.uk/Notice/274a9dc1-959c-4f21-9953-11490d5443e3` (visited on 10/03/2025).

[46] *Supply, Installation and Commissioning of Two 1MW Dynamometers and Associated Equipment. Contract award notice 2022/S 000-006282*. University of Strathclyde. Mar. 8, 2022. URL: `https://www.find-tender.service.gov.uk/Notice/006282-2022/PDF` (visited on 10/03/2025).

[47] *Capax successfully implemented a EUR 2.1 million investment*. Capax d.o.o. Oct. 2018. URL: `https://www.capax.hr/news/capax-successfully-implemented-a-eur-2-1-million-investment/` (visited on 10/03/2025).

[48] Barber-Nichols. *NSDS Pump Chart*. Access via Tools & Resources page: https://barber-nichols.com/media/tools-resources/. Online image. URL: `https://www.barber-nichols.com/wp-content/uploads/2019/07/pump-chart.png` (visited on 07/10/2025).

[49] Igor J Karassik. *Pump handbook*. 2001.

[50] C Pfleiderer. *Die Kreiselpumpen für Flüssigkeiten und Gase: Wasserpumpen, Ventilatoren, Turbogebläse Turbokompressoren*. Springer-Verlag, 2013.

[51] CFturbo GmbH. *CFturbo [Computer software]*. `https://cfturbo.com/`. Version 2025 R2.3; accessed 2025-11-01. Dresden, Germany, 2025.

[52] L Souverein et al. “Design and tool anchoring for a 120-kilonewton expander cycle rocket engine liquid oxygen turbopump”. In: *Progress in Propulsion Physics–Volume 11* 11 (2019), pp. 591–612.

[53] J.K. Jakobsen and RB Keller Jr. *Liquid rocket engine turbopump inducers*. Tech. rep. NASA, 1971.

[54] Dassault Systèmes SolidWorks Corporation. *SOLIDWORKS [Computer software]*. `https://www.solidworks.com/`. Version 2025; accessed 2025-11-01. Waltham, MA, USA, 2025.

[55] M Shamoushaki et al. “Development of cost correlations for the economic assessment of power plant equipment”. In: *Energies* 14.9 (2021), p. 2665.

[56] U.S. Bureau of Labor Statistics. *Producer Price Index by Industry: Pump and Compressor Manufacturing*. Series ID: PCU3339133391; Index base: Dec 2003 = 100; Not seasonally adjusted; Monthly. U.S. Bureau of Labor Statistics, 2025. URL: `https://data.bls.gov/timeseries/PCU3339133391` (visited on 09/09/2025).

[57] R Knuts. “Improvement Suggestions for a Load Bank Control System”. In: (2023).

[58] Cummins Generator Technologies Ltd. *P734H Technical Data Sheet*. Tech. rep. TD_P734H_Rev.B_17.03.16. Mechanical data lists Moment of Inertia: 55.6 kg·m2 (1-bearing) and 54.5 kg·m2 (2-bearing). STAMFORD | AvK, 2016. URL: `https://www.kentepower.com/uploads/4d26205a.pdf` (visited on 11/01/2025).

[59] Cummins Generator Technologies GmbH. *Technical Data Sheet: DIG142D 6.6 kV Alternator*. Tech. rep. Lists moment of inertia $J = 165$ kg·m2. AvK, 2013. URL: `https://www.stamford-avk-stg.cummins.com/sites/stamfordavk/files/dig142d_4_60_6600.pdf` (visited on 11/01/2025).

[60] IEC. *CENELEC standard voltages*. Standard 60038. Dec. 2011. URL: `https://www.nen.nl/en/nen-en-iec-60038-2011-en-164344`.

[61] Marathon ®Generators. *Generators: Selection and Pricing Catalogue*. 2018. URL: `https://www.marathongenerators.com/generators/images/SB0163E-50Hz.pdf`.

[62] U.S. Bureau of Labor Statistics. *Producer Price Index by Commodity: Machinery and Equipment: Motors, Generators, Motor Generator Sets (WPU1173)*. Index 1982=100, monthly, not seasonally adjusted. Retrieved via FRED, Federal Reserve Bank of St. Louis. Aug 2025 = 314.249. Accessed 3 Oct 2025 (Europe/Amsterdam). 2025. URL: `https://fred.stlouisfed.org/series/WPU1173`.

[63] European Central Bank. *Euro foreign exchange reference rates: US dollar (USD)*. ECB euro reference exchange rate. EUR 1 = USD 1.1754 on 2 Oct 2025. Accessed 3 Oct 2025 (Europe/Amsterdam). Oct. 2, 2025. URL: `https://www.ecb.europa.eu/stats/policy_and_exchange_rates/euro_reference_exchange_rates/html/eurofxref-graph-usd.en.html`.

[64] Avtron Power Solutions. *True Direct-Connect Medium Voltage Load Banks: Eliminating the Step-Down Transformer Yields Capacity and Cost Benefits*. White paper. Revision: September 2019. Sept. 2019. URL: `https://avtronpower.com/wp-content/uploads/2022/10/True-Direct-Connect-MV-LB-2022-nre.pdf` (visited on 10/03/2025).

[65] R Tassenoy et al. “Assessing the influence of compressor inertia on the dynamic performance of large-scale vapor compression heat pumps for Carnot batteries”. In: *Journal of Energy Storage* 101 (2024), p. 113948.

[66] M Ehrgott. *Multicriteria optimization*. Springer, 2005.

[67] S Duleba and Sarbast Moslem. “Examining Pareto optimality in analytic hierarchy process on real Data: An application in public transport service development”. In: *Expert Systems with Applications* 116 (2019), pp. 21–30.

[68] T.L. Saaty. “A scaling method for priorities in hierarchical structures”. In: *Journal of mathematical psychology* 15.3 (1977), pp. 234–281.

[69] China Ningbo SUP Bearing Co., Ltd. *Bearing Units*. `http://www.supbearing.com/bearing_units.htm`. Accessed: 2025-12-01.

[70] A. S. Alghamdi, Yousef SH Najjar, and Mohammad H Al-Beirutty. “Aerothermal design of a multistage axial flow gas turbine with air cooling”. In: *International Journal of Mechanical Engineering Education* 38.1 (2010), pp. 9–27.

[71] D Dorney et al. “Calculation of turbine axial thrust by coupled CFD simulations of the main flow path and secondary cavity flow in an SLI LOX turbine”. In: *39th AIAA/ASME/SAE/ASEE Joint Propulsion Conference and Exhibit*. 2003, p. 4919.

[72] *LOx Turbine - Vulcain and Vulcain 2 Engines*. Volvo Aero Corporation. 2005.

[73] *LH2 Turbine - Vulcain and Vulcain 2 Engines*. Volvo Aero Corporation. 2005.

[74] S Andersson and S Trollheden. “Aerodynamic Design and Development of a two-stage supersonic Turbine for Rocket Engines”. In: *35th AIAA/ASME/SAE/ASEE Joint Propulsion Conference Exhibit* (1999).

[75] S Andersson, M Lindeblad, and U Wahlen. “Performance test results for the Vulcain 2 supersonic/transonic turbine”. In: *34th AIAA/ASME/SAE/ASEE Joint Propulsion Conference and Exhibit*. 1998, p. 3999.

[76] D ISO. “Mechanical vibration—Balance quality requirements for rotors in a constant (rigid) state—Part 1: Specification and verification of balance tolerances”. In: *ISO 1940-1: 2003* (2003).

[77] O Matsushita et al. *Vibrations of rotating machinery*. Springer, 2017, p. 105.

[78] *INCONEL alloy 718*. Special Metals Corporation. July 2007.

[79] K Holmedahl. “Analysis and testing of the Vulcain 2 LOX turbine blades for prediction of high cycle fatigue life”. In: *36th AIAA/ASME/SAE/ASEE Joint Propulsion Conference and Exhibit*. 2000, p. 3680.

[80] J.F. Gülich. *Centrifugal pumps*. Springer, 2010, pp. 665–714.

[81] W.E. Forsthoffer. *Forsthoffer’s best practice handbook for rotating machinery*. Elsevier, 2011.

[82] ROSS devs. *ROSS User Guide*. English. ROSS. 2024.

[83] A Öchsner. “Timoshenko beam theory”. In: *Classical Beam theories of structural mechanics*. Springer, 2021, pp. 67–104.

[84] SKF. *Super-precision bearings*. Catalogue PUB BU/P1 13383/2 EN. This publication supersedes 6002. Gothenburg, Sweden: SKF Group, Mar. 2016. URL: `https://www.skf.com/binaries/pub12/Images/0901d19680495562-Super-precision-bearings-catalogue---13383_2-EN_tcm_12-129877.pdf` (visited on 10/09/2025).

[85] ISO - International Organization for Standardization. *Rolling bearings — Static load ratings*. Geneva, May 2006. URL: `https://www.iso.org/standard/38101.html`.

[86] SKF. *The UltraFast Series — Super-precision angular contact ball bearings*. URL: `https://www.skf.com/us/products/super-precision-bearings/angular-contact-ball-bearings/the-ultrafast-series` (visited on 10/08/2025).

[87] SKF. *71910 ABA/HCP4ADG — Matched set of two super-precision, UltraFast A design, single row angular contact ball bearings*. URL: `https://www.skf.com/us/products/super-precision-bearings/angular-contact-ball-bearings/productid-71910%20ABA%2FHCP4ADG` (visited on 10/08/2025).

[88] *7006 CE/P4ADBA — Super-precision angular contact ball bearings*. Product page for matched set of two super-precision, high-speed E design, single row ACBBs (DB arrangement). SKF Group. URL: `https://www.skf.com/us/products/super-precision-bearings/angular-contact-ball-bearings/productid-7006%20CE%2FP4ADBA` (visited on 10/23/2025).

[89] Patrick G. “Ball bearing stiffness: a new approach offering analytical expressions”. In: *Proceedings of the European Space Mechanisms and Tribology Symposium (ESMATS)*. Accessed 2025-10-09. 2015, pp. 1–7. URL: `https://esmats.eu/esmatspapers/pastpapers/pdfs/2015/guay.pdf`.

[90] Farhad E. Aslan-zada, Vugar A. Mammadov, and Fadi Dohnal. “Brush seals and labyrinth seals in gas turbine applications”. In: *Proceedings of the Institution of Mechanical Engineers, Part A: Journal of Power and Energy* 227.2 (2013), pp. 216–230. DOI: `10.1177/0957650912464922`. URL: `https://doi.org/10.1177/0957650912464922`.

[91] R.C. Hendricks et al. *Interfaces—Weak Links, Yet Great Opportunities*. NASA Technical Memorandum NASA/TM-2011-214041. Cleveland, OH: NASA Glenn Research Center, May 2011. URL: `https://ntrs.nasa.gov/citations/20110012458`.

[92] HR Heidari and Pedram Safarpour. “Design and modeling of a novel active squeeze film damper”. In: *Mechanism and Machine Theory* 105 (2016), pp. 235–243.

[93] A Manjunath, Shriharsha Patil, et al. “Stiffness Optimization of Squirrel Cage in Aircraft Engines”. In: *International Journal of Engineering and Advanced Technology* 14.1 (2024), pp. 10–35940.

[94] L San Andrés et al. “Squeeze film dampers: an experimental appraisal of their dynamic performance”. In: *First Asia Turbomachinery and Pump Symposium*. 2016, pp. 22–25.

[95] *7014 CEGA/HCP4A — Super-precision angular contact ball bearing*. Single-row, high-speed E design; super-precision. SKF. URL: `https://www.skf.com/id/products/super-precision-bearings/angular-contact-ball-bearings/productid-7014%20CEGA%2FHCP4A` (visited on 10/30/2025).

[96] *API Standard 610: Centrifugal Pumps for Petroleum, Petrochemical, and Natural Gas Industries*. Authoritative industry standard; 12th edition (January 2021). Washington, DC: American Petroleum Institute, Jan. 2021.

[97] *Atlantic Heat Transfer Oils — Product Data Sheet*. Includes specific heat capacity vs. temperature table for ISO 30 and ISO 100 grades. Atlantic Lubricants Pty Ltd, Nov. 2024. URL: `https://www.atlanticoil.com/storage/Atlantic-Heat-Transfer-Oils-PDS.pdf` (visited on 10/30/2025).

[98] *Automatic oil circulation lubrication systems. Product catalogue 2024*. SKF Group, 2024.